UNIVERSITA' DEGLI STUDI DI PARMA

Dottorato di Ricerca in Fisiopatologia Sistemica

Ciclo XXVIII

Electro-mechanical coupling in the aging heart: Role of the Late Na^+ current

Meccanismo di Eccito-Contrazione nel cuore anziano: Ruolo della corrente protratta del Na^+

Coordinatore:

Chiar.mo Prof. Enrico Maria Silini

Tutor:

Chiar.mo Prof. Federico Quaini

Dottorando:

Dott. Andrea Sorrentino

Contents

Abstract

The aging myopathy manifests itself with diastolic dysfunction and preserved ejection fraction. However, the difficulty in defining myocardial aging and the mechanisms involved complicates the recognition of the cellular processes underlying impaired diastolic relaxation. We raised the possibility that, in a mouse model of physiological aging, defects in the electromechanical properties of cardiomyocytes are important determinants of the diastolic properties of the myocardium, independently from changes in the structural composition of the muscle and collagen framework. Here we show that an increase in the late Na^+ current (I_{NaL}) in aging cardiomyocytes prolongs the action potential (AP) and influences the temporal kinetics of Ca^{2+} cycling and cell shortening. These alterations increase force development and passive tension. Inhibition of I_{NaL} shortens the AP and corrects the dynamics of Ca^{2+} transient, cell contraction and relaxation. Similarly, repolarization and diastolic tension of the senescent myocardium are partly restored. I_{NaL} offers inotropic support, but negatively interferes with cellular and ventricular compliance, providing a new perspective of the biology of myocardial aging and the etiology of the defective cardiac performance in the elderly.

Keywords: Aging, Diastolic Dysfunction, Sodium Currents, Contractility

List of Abbreviations

4-AP, 4-aminopyridine

ATX-II, anemonia toxin-II

AP, action potential

$\mathbf{I_{CaL}}$, L-type Ca^{2+} current

$\mathbf{I_{NaL}}$, late Na^{+} current

LV, left ventricle

MAP, monophasic action potential

Mex, mexiletine

NCX, Na^{+}/Ca^{2+} exchanger

Ran, ranolazine

RMP, resting membrane potential

RyR, ryanodine receptor

SERCA, sarco-endoplasmic Ca^{2+} pump

SR, sarcoplasmic reticulum

TTX, tetrodotoxin

Introduction

Aging is a major risk factor for cardiovascular disease and the leading cause of deaths in individual more than 65 years of age (Schwartz & Zipes, 2011; Mozaffarian *et al.*, 2015). The aging myopathy typically manifests itself with diastolic dysfunction and preserved ejection fraction (EF) (Schwartz & Zipes, 2011). More than 50% of patients with heart failure have normal or near normal EF and the incidence and prevalence of this condition increases with age.

Although the claim is commonly made that age-associated physiological changes predispose older adults to develop heart failure with normal EF, the etiology of diastolic heart failure is unknown. The difficulty in defining myocardial aging and the mechanisms involved further complicates the recognition of the cellular processes underlying impaired diastolic relaxation. An important aspect of the aged heart is represented by the attenuated contractile reserve, which manifest in the elderly with exercise intolerance (Correia *et al.*, 2002; Lakatta, 2003; Lakatta & Levy, 2003; Hees *et al.*, 2006; Schwartz & Zipes, 2011). Whether impaired autonomic balance and/or defective mechanisms of inotropic support in aging myocytes are responsible for the blunted response of the aged heart to increase workload demand remain to be clarified (White *et al.*, 1994; Xiao *et al.*, 1994).

In the current study we raised the possibility that, in a mouse model of physiological aging, defects in the electromechanical properties of cardiomyocytes are critical determinants of the altered cardiac performance, independently from changes in the structural composition of the myocardium and collagen framework. Cardiomyocytes constitute nearly 90% of the myocardium and alterations in the mechanisms of cell excitation, force generation and kinetics of contraction may be critical in conditioning the abnormalities of the old heart. Aging alters the pattern of electrical activation, resulting in prolonged myocardial repolarization (Reardon & Malik, 1996; Schwartz & Zipes, 2011), which enhances the risk of ventricular arrhythmias and sudden death (Roden & Viswanathan, 2005). Moreover, prolongation of the time of repolarization and perturbations of intracellular ionic balance may influence the contractile and relaxation dynamics of the aging heart, impacting on diastolic and systolic function (Maeder & Kaye, 2009).

Impaired diastolic function includes abnormalities in muscle relaxation, distensibility and ventricular filling pattern (Zile *et al.*, 2001). The increase in myocardial stiffness has been

ascribed to changes in the composition of the extracellular matrix and/or to intrinsic characteristics of cardiomyocytes (Borlaug & Paulus, 2011). Switches in titin-isoforms and post-translational modifications of this cytoskeletal protein may affect the passive mechanical properties of myocytes, but whether defective electrical activation contributes to the process remains to be defined.

The mechanical activity of the myocardium is initiated by the electrical excitation of the tissue, which acts as a functional syncytium in propagating membrane depolarization in cardiomyocytes (Joyner *et al.*, 1983). The upstroke of the action potential triggers Ca^{2+} entry via L-type Ca^{2+} channels, which activate ryanodine receptors (RyRs), another class of Ca^{2+} channels located on the sarcoplasmic reticulum (SR), resulting in the translocation of Ca^{2+} from this site of storage to the cytoplasm. This process is termed Ca^{2+}-induced Ca^{2+} release (Fabiato, 1983; Bers, 2002) (**Figure 1**). The raise in cytosolic Ca^{2+} activates the contractile apparatus by promoting cross-bridge formation between myofilaments, thus initiating cell contraction. Subsequently, cytosolic Ca^{2+} levels are restored by the re-uptake of Ca^{2+} into the SR via the sarco-endoplasmic reticulum Ca^{2+} ATPase (SERCA) and Ca^{2+} extrusion via the Na^{+}/Ca^{2+} exchanger (NCX) (Bers, 2002).

The repolarization phase of the action potential is a relevant variable of the kinetics of Ca^{2+} entry; it controls the pattern of Ca^{2+} influx via L-type channels and NCX in a time and voltage dependent manner (Sah *et al.*, 2001; Bers, 2002; Janczewski *et al.*, 2002; Sah *et al.*, 2003; Rota *et al.*, 2007; Signore *et al.*, 2013). Thus, transmembrane Ca^{2+} fluxes and Ca^{2+}-induced Ca^{2+} release modulate the temporal dynamic of $[Ca^{2+}]_i$ (Sah *et al.*, 2001; Janczewski *et al.*, 2002; Sah *et al.*, 2003; Rota *et al.*, 2007; Signore *et al.*, 2013), providing an important link between electrical activity, on the one hand, and myocyte and myocardial contractility and relaxation, on the other.

An important component of the repolarization phase of the AP is represented by the late Na^{+} current (I_{NaL}) (Maltsev *et al.*, 1998; Maltsev & Undrovinas, 2008; Zaza & Rocchetti, 2013). Increase in I_{NaL} has been associated with altered electrophysiological and mechanical function of human myocytes and cells obtained from animal model of human disease (Maltsev *et al.*, 1998; Maltsev *et al.*, 2007; Maltsev & Undrovinas, 2008; Sossalla *et al.*, 2008; Zaza *et al.*, 2008; Coppini *et al.*, 2013), raising the possibility that alterations in the slowly inactivation Na^{+} current play a role in the remodeled electrical activity of senescent myocytes.

Here, we have tested the hypothesis that defects in the tightly controlled system that governs intracellular ionic homeostasis become apparent in the senescent heart contributing to the manifestations of the aging myopathy and impaired diastolic function. This analysis has been combined with measurements of the size and shape of the organ, structural composition of the myocardium and myocyte volume. This extensive examination has been performed in the attempt to recognize determinants of the aging myopathy and their potential implications in the development of life-threatening arrhythmia and ventricular dysfunction.

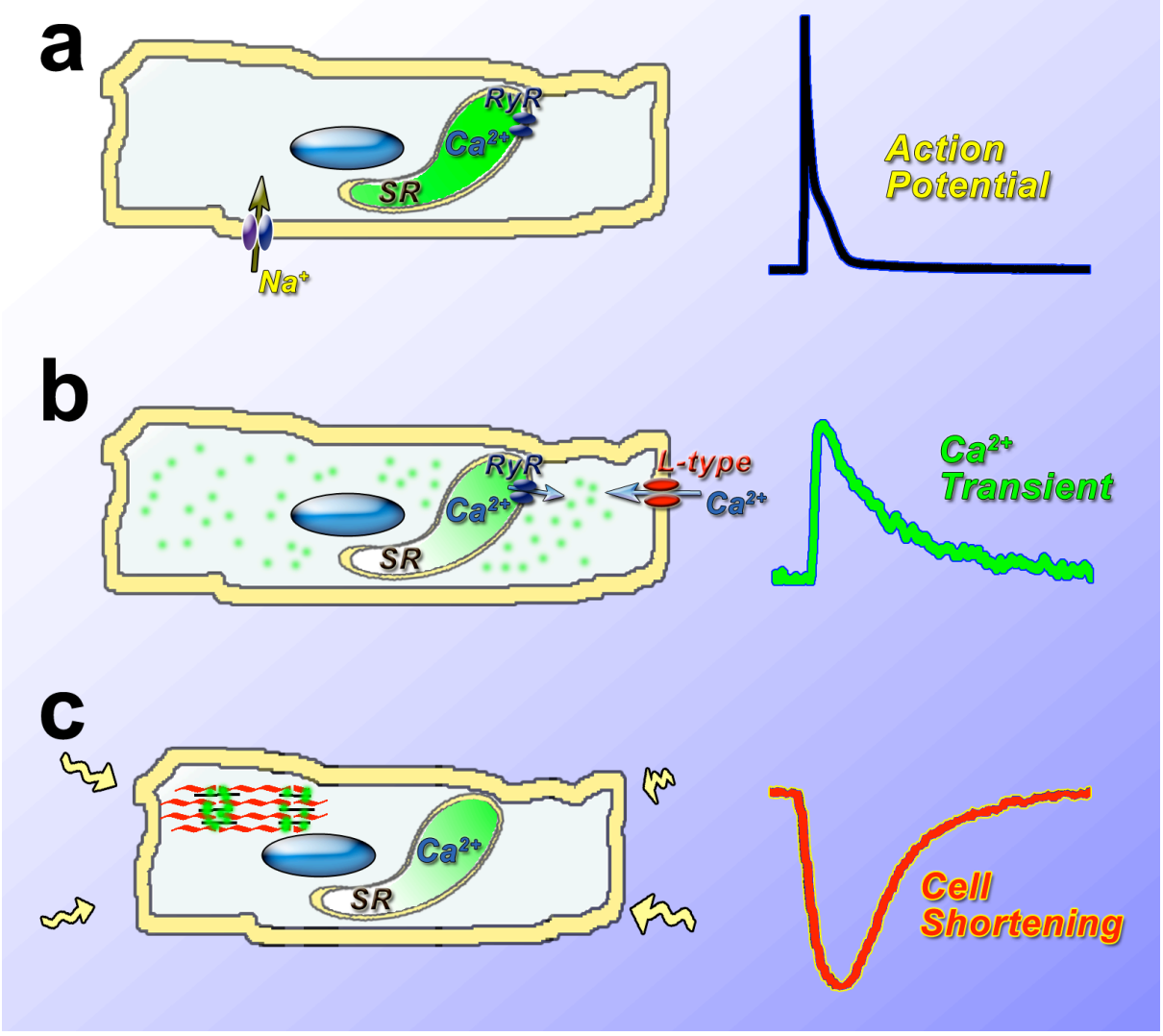

Figure 1. Excitation contraction coupling. Cartoon illustrating Ca^{2+} handling protein in cardiomyocytes. On right side, action potential, Ca^{2+} transient and cell shortening obtained from mouse left ventricular myocytes are reported (courtesy of Dr. Rota).

Materials and Methods

In vivo studies. C57Bl/6 mice from 3 to 35 months of age were used in this study. Animals were maintained in accordance with the Guide for Care and Use of Laboratory Animals; animal experiments were approved by the local animal care committee (IACUC). When needed, isoflurane (1-1.5%, inhalation) was employed as methodology of anesthesia.

In the attempt to define the effects of aging on LV function, anatomy and structure in mice, several assays were employed. The broad experimental approach was designed to obtain detailed information in vivo and to overcome limitations intrinsic to various experimental protocols applied and acquisition systems used.

Blood pressure in conscious mice was analyzed with a computerized, non-invasive tail-cuff plethysmography system (BP 2000 Blood Pressure Analysis System, Visitech Systems) (Krege *et al.*, 1995). For each mouse, ten inflation-deflation cycles were used initially to set amplifier and instrument controls. Subsequently, systolic blood pressure was calculated by averaging readings from forty cycles.

Echocardiography was performed in conscious mice using a Visualsonics Vevo 2100 System equipped with a MS550D high frequency (22-55 MHz) linear transducer. By this approach, long and short axis views of the LV were analyzed (Rota *et al.*, 2005; Bauer *et al.*, 2011). Diastolic function was assessed using pulsed-wave Doppler imaging of the transmitral filling pattern in the apical four-chamber view of the heart. Early transmitral filling wave (E-wave) and late filling wave due to atrial contraction (A-wave) were obtained. Isovolumic relaxation time was calculated as the time from closure of the aortic valve to the initiation of the E-wave, and isovolumic contraction time was calculated as the time from closure of the mitral valve to opening of the aortic valve. The deceleration time of the E-wave was determined by measuring the time needed for the down-slope of the peak of the E-wave to reach baseline (Ram *et al.*, 2011).

For high frequency speckle tracking imaging (Ram *et al.*, 2011), mice were anesthetized and B-mode loops were recorded in the parasternal long- and short-axis views, while continuous ECG monitoring was obtained via limb electrodes. Three consecutive cardiac cycles were selected and analyzed with Vevostrain software (Visualsonics). Strain measures were averaged over the cardiac cycles resulting in curvilinear strain and strain rates. In both the long- and short-axis views, the LV myocardium was divided into 6 standard anatomic

segments, which were averaged for global speckle-tracking based strain analysis throughout the cardiac cycle. Images collected with suboptimal physiological parameters or inadequate visualization of the endocardial border were excluded.

Magnetic resonance imaging (MRI) was performed with a 7 Tesla Pharmascan (Bruker) system equipped with a mouse cardiac coil in birdcage design (Rapid Biomedical) to obtain cine volumetric short axis (Nahrendorf *et al.*, 2006). To reduce motion artifacts and heart rate, animals were anesthetized with isoflurane by nose cone and placed into the coil in prone position. Electrodes were attached to the front left paw and right leg for electrocardiographic gating and monitoring of vital signs using a gradient echo sequence (echo time 2.6 ms, 16 frames per RR interval; flip angle 30 degrees; in-plane resolution 200x200 µm; slice thickness 1 mm). Animals were kept warm by blowing hot air into the magnet. The heat flow and the anesthesia level were manually adjusted to maintain heart rate. Anatomical and functional parameters were quantitated from 6-8 cine short axis imaging slices covering the LV.

Electrocardiograms (ECGs) were recorded under isoflurane anesthesia by inserting needle electrodes subcutaneously into the mouse limbs (lead II). Electrical signals were amplified (Animal Bio Amp, ADInstruments), digitized using a 4 kHz A/D converter (MPVS-400, Millar Instruments) and recorded using LabChart software (ADInstruments), with low and high-pass filtering at 100 Hz and 3 Hz, respectively. Surface ECG intervals were measured using LabChart7 or LabChart8. Spontaneous cycle length was determined by averaging 10 consecutive R-R intervals. PR and QT intervals were measured by determining the earliest onset and latest offset of atrial and ventricular deflections from the averaged cycles (**Figure 2**) (Hagendorff *et al.*, 1999; Korte *et al.*, 2002; Roell *et al.*, 2007).

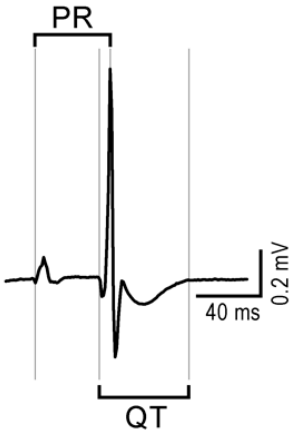

Figure 2. **ECG parameters.** PR and QT intervals are defined on the electrocardiogram obtained from a young mouse. Scale bars: 40 ms, 0.2 mV.

To record ECGs in freely roaming, anesthetized animals, telemetric biopotential transmitters (ETA-F10, Data Science International) were implanted surgically in anesthetized mice (Knollmann *et al.*, 2003). Surgery was performed in anesthetized mice. The peritoneum was exposed with a midline incision, the implant was secured within the peritoneal cavity, and leads were implanted subcutaneously corresponding to position II. Subsequently, signals were transmitted from implants to RPC-1 receivers and Data Exchange Matrix (Data Science International), and stored in a computer. The telemetric ECG was analyzed during normal activity and following pharmacological treatments. All recordings were digitized at 2 kHz and analyzed off-line with Ponemah 5.10 software.

Left ventricular (LV) hemodynamics and pressure-volume (PV) loops were obtained in anesthetized mice (isoflurane, 1.5%) in the closed chest preparation with a MPVS-400 system for small animals (Millar Instruments) equipped with a PVR-1045 catheter (Torella *et al.*, 2004; Rota *et al.*, 2005; Pacher *et al.*, 2008; Ferreira-Martins *et al.*, 2009; Cingolani & Kass, 2011). The mouse was intubated and ventilated (MiniVent Type 845, Hugo Sachs Elektronik-Harvard Apparatus) with isoflurane anesthesia and a warmed with a heat lamp; the right carotid artery was then exposed and the pressure transducer was inserted and advanced in the LV cavity. Data were acquired with Chart 5 or LabChart8 (ADInstruments) software. Baseline PV loops and loops following inferior vena cava or aortic arch occlusions were collected to compute the slope of end-diastolic PV relations (EDPVR), which is an indicator of LV stiffness (Cingolani & Kass, 2011). During data collection, ventilation was interrupted to acquire signals without motion artifacts. Inferior vena cava occlusion was achieved in the closed chest preparation by compression of the inferior vena cava accessed immediately below the diaphragm via a small abdominal incision, with a cotton tip applicator (Pacher *et al.*, 2008). For aortic arch occlusion, a thoracotomy through the sternoclavicular articulations provided exposure of the aortic arch allowing its transient constriction with a bulldog clamp (Pfeffer *et al.*, 1979). For calibration of PVR-1045 catheter and evaluation of LV blood volume, manufacturer's instructions were followed. Cuvette calibration with fresh heparinized, warm blood and in vivo bolus infusion of hypertonic saline solution were performed to compute slope and intercept and to assess parallel conductance. Analysis was performed using LabChart and PVAN (Millar) software. Systolic duration was computed by LabChart as the elapsed time between the start of the cycle at LV end-diastolic pressure, and the time of maximal -dP/dt.

For combined autonomic blockade atropine (0.5 mg kg^{-1} body weight, i.p., Hospira) plus propranolol (1 mg kg^{-1} body weight, i.p., Fluka) were administered to animals (Gehrmann *et al.*, 2000; Saba *et al.*, 2003; D'Souza *et al.*, 2014). In vivo blockade of the late Na^+ current (I_{NaL}) was achieved with administration of ranolazine (30 mg kg^{-1} body weight, i.p. or 2.5-5 mg kg^{-1} body weight, i.v., Sigma) (Lovelock *et al.*, 2012) or mexiletine (5 mg kg^{-1} body weight, i.p., Sigma) (De Luca *et al.*, 2004). Compounds were dissolved in USP saline solution. Ranolazine bolus was delivered via left jugular vein using a syringe pump (PHD Ultra, Harvard Apparatus).

Ex-vivo properties of the mouse heart. To assess ex-vivo electrical properties and isovolumic LV pressure, hearts were perfused through the aorta in a Langendorff apparatus (Radnoti) at a constant pressure of 80 mm Hg with Krebs–Henseleit buffer (KHB; Sigma), containing in mM: 118 NaCl, 4.7 KCl, 11 glucose, 1.2 $MgSO_4$, 1.2 KH_2PO_4, 1.8 $CaCl_2$ and 25 $NaHCO_3$, gassed with 95% O_2 and 5% CO_2 (pH 7.4) at 37°C (Goichberg *et al.*, 2011; Signore *et al.*, 2013). The temperature was maintained by immersing the heart in a water-heated glassware reservoir (Radnoti), containing preheated KHB. Hearts were stimulated with a 2 ms square pulse at 1.5-fold its threshold level (4 channels stimulator, BMS 414, Crescent Electronics), using a mini-coaxial electrode (Harvard Apparatus). A two-lead mini ECG system (Harvard Apparatus), in which electrodes were placed on the right atrium and apex of the heart, was used to obtain pseudo-ECG. Monophasic action potentials (MAPs) were recorded using a micro MAP-Tip electrode (Harvard Apparatus) positioned on the LV free wall (Goichberg *et al.*, 2011; Signore *et al.*, 2013). ECG and MAP signals were amplified (Animal Bio Amp, ADInstruments), digitized by a 4 kHz A/D converter (Power Lab 8/30, ADInstruments) and recorded with LabChart software, with low and high-pass filtering at 1 kHz and 0.3 Hz, respectively. A protocol of programmed electrical stimulation (PES) was introduced to assess the propensity of the mouse heart to develop ventricular arrhythmia. PES consisted of a train of pacing stimuli (S1) applied at 125 ms cycle length, with an extra stimulus (S2) inserted every 8 beats. The S1-S2 interval was progressively reduced until the S2 stimulus either failed to generate an action potential, or induced arrhythmic events. The appearance of ventricular tachycardia (3 or more consecutive ectopic beats characterized by atria-ventricular dissociation) and/or ventricular fibrillation was established (Goichberg *et al.*, 2011; Signore *et al.*, 2013). Data were analyzed with LabChart software.

Myocyte isolation. Hearts were excised and LV myocytes were enzymatically dissociated as reported previously (Torella *et al.*, 2004; Rota *et al.*, 2005; Rota *et al.*, 2007; Ferreira-Martins *et al.*, 2009; Signore *et al.*, 2013). Briefly, the heart was connected to a plastic cannula for retrograde perfusion through the aorta in a Langendorff system (Radnoti) at 37°C. Perfusate consisted of a Ca^{2+}-free solution gassed with 85% O_2 and 15% N_2. After 5 minutes, 0.1 mM $CaCl_2$, 274 units/ml collagenase (type 2, Worthington Biochemical Corp) and 0.57 units/ml protease (Type XIV, Sigma) were added to the solution which contained in mM: NaCl 126, KCl 4.4, $MgCl_2$ 5, HEPES 5, Glucose 22, Taurine 20, Creatine 5, Na Pyruvate 5 and NaH_2PO_4 5 (pH 7.4). At completion of digestion, atria and right ventricle were dissected and LV myocardium was cut in small pieces and these fragments were shaken in re-suspension solution and filtered using a 200 μm nylon mesh (Spectrum Labs). Aliquots of cell suspensions were centrifuged for 5 minutes at 100*g* (Eppendorf 5702 R) at 4°C and frozen for biochemical assays and fixed in paraformaldehyde (4%, Electron Microscopy Sciences). For electrophysiological and mechanical studies only rod-shaped myocytes exhibiting cross striations, and showing no spontaneous contractions or contractures were selected; cells were used within 8 hours following enzymatic digestion.

Myocyte volume. LV myocytes fixed in paraformaldehyde were stained with the nuclear dye Hoechst (10 μM, Sigma). Images were collected with a fluorescent inverted microscope (Olympus IX71) equipped with a CCD camera (Hamamatsu ORCA-R2). Cell length and area were evaluated using ImageJ software. Myocyte volume was then computed assuming an elliptical cross-section, in which the major axis corresponds to the average cell width, and the minor axis was computed after establishing the ratio between the major and minor axis, using three dimensional optical section reconstruction by two-photon microscopy (BX51WI Olympus microscope coupled with a Bio-Rad Radiance 2100MP system) and image analysis (ImageJ). Three dimensional reconstructions were obtained using second-harmonic generation signal of sarcomeric structures (Plotnikov *et al.*, 2006).

Histological analysis. Mouse hearts were fixed in phosphate buffered formalin (10%, Sigma) and embedded in paraffin. Sections 4 μm thick of the LV were trichrome-stained for detection of connective tissue (Gomori`s One Step Trichrome Method, Poly Scientific R&D Corp.) following manufacturer's instructions. Images were acquired using an upright

microscope (Olympus BX60) with 20x objective equipped with a color camera (Olympus DP73). Interstitial fibrosis was quantified with respect to total tissue area using ImageJ software.

Cell shortening and Ca^{2+} transients. Isolated LV myocytes were placed in a bath on the stage of an Axiovert (Zeiss), IX71, and BH-2 (Olympus) microscopes for contractility and Ca^{2+} transients (Torella *et al.*, 2004; Rota *et al.*, 2005; Rota *et al.*, 2007; Ferreira-Martins *et al.*, 2009; Signore *et al.*, 2013). Experiments were conducted at room temperature. Cells were bathed continuously with a Tyrode solution containing (in mM) NaCl 140, KCl 5.4, $MgCl_2$ 1, HEPES 5, Glucose 5.5 and $CaCl_2$ 1.0 (pH 7.4, adjusted with NaOH). Measurements were collected in field-stimulated (S88 and SD9 Grass stimulators) cells by IonOptix fluorescence and contractility systems (IonOptix), or by video edge detection (VED-205, Crescent Electronics; PowerLab 8/35, Adinstruments). Contractions were elicited by rectangular depolarizing pulses, 2 ms in duration, and 1.5 times threshold in intensity, with platinum electrodes. Ca^{2+} transients were measured by epifluorescence after loading the myocytes with 10 μM Fluo-3 AM or 2 μM Fluo-4 AM (Invitrogen). Excitation length was 480 nm with emission collected at 535 nm using a 40x objective. Fluo signals were expressed as normalized fluorescence (F/F_0), where F_0 is the diastolic fluorescent level subtracted by the background signal measured in the region adjacent to the cell (Signore *et al.*, 2013).
Unless otherwise specified, the late Na^+ current (I_{NaL}) was blocked with low dose of ranolazine (10 μM, Sigma) or mexiletine (10 μM, Sigma), or enhanced with anemonia toxin II (1 nM, Sigma) (Sicouri *et al.*, 1997; Rota & Vassalle, 2003; Sossalla *et al.*, 2008; Sossalla *et al.*, 2011; Wagner *et al.*, 2011; Wu *et al.*, 2011; Gao *et al.*, 2013; Fischer *et al.*, 2015). Rapidly activating Kv outward currents were blocked with 0.5 mM 4-aminopyridine (4-AP, Sigma) (Brouillette *et al.*, 2004; Rota *et al.*, 2007; Liu *et al.*, 2011).

Caffeine-induced Ca^{2+} transients. To evaluate SR Ca^{2+} load in field stimulated myocytes, a 2 sec caffeine (20 mM, Sigma) spritz was delivered using glass pipettes and a microinjector (FemtoJet, Eppendorf AG, or Pico-liter Injector, Warner Instruments), and Ca^{2+} transients recorded by epifluorescence microscope and IonOptix system, or two-photon microscope (Rota *et al.*, 2005; Rota *et al.*, 2007; Ferreira-Martins *et al.*, 2009; Signore *et al.*, 2013). For two-photon imaging, myocytes were loaded with 5 μM Fluo-4 AM and placed on the stage of

an upright microscope (BX51WI Olympus microscope coupled with a Bio-Rad Radiance 2100MP system). Cells were bathed with Tyrode solution and field stimulated using platinum electrodes. Fluo-4 was excited at 920 nm wavelength with mode-locked Ti:sapphire femtosecond laser (Tsunami, Spectra-Physics), and the emission signal was collected at 535 nm. Images were acquired in line scan mode with the myocyte oriented in the long axis, at 6 ms sampling rate (Ferreira-Martins *et al.*, 2009; Signore *et al.*, 2013). Fluo signals were expressed as normalized fluorescence (F/F_0), where F_0 is the diastolic fluorescent level subtracted by the background signal measured in the region adjacent to the cell (Signore *et al.*, 2013). Due to potential leak of caffeine from the glass pipette and undesired facilitation of Ca^{2+} release, cells displaying paced-induced Ca^{2+} transients larger than 5 F/F_0 (corresponding to values above average+2·SD) were excluded from the analysis.

Na^+/Ca^{2+} exchange (NCX) activity was evaluated by the decay of the caffeine-induced Ca^{2+} transient, which was fitted with a mono-exponential function (Tang *et al.*, 2010; Voigt *et al.*, 2012). Cells presenting prolonged Ca^{2+} transient decay (>4.8 sec, corresponding to values >average+2·SD) and/or poor fitting (R^2<0.96) were excluded from the study, without affecting statistical results.

Whole-cell patch-clamp studies. Isolated LV myocytes were placed in a bath on the stage of an IX51, IX53, and IX71 (Olympus) microscopes for patch-clamp measurements (Rota & Vassalle, 2003; Torella *et al.*, 2004; Rota *et al.*, 2005; Rota *et al.*, 2007; Ferreira-Martins *et al.*, 2009; Signore *et al.*, 2013). Experiments were conducted at room temperature. Data were acquired by means of the whole-cell patch-clamp technique in voltage- and current-clamp modes using Multiclamp 700A and 700B, and Axoclamp 900A amplifiers (Molecular Devices). Electrical signals were digitized using 250 kHz 16-bit resolution A/D converters (Digidata 1322, 1440A, and 1550, Molecular Devices) and recorded using pCLAMP 9.0 and 10 software (Molecular Devices) with low-pass filtering at 2 kHz. Membrane capacitance (C_m) was measured in voltage-clamp mode using a 5 mV voltage step and pCLAMP software algorithm; this parameter was employed to normalize transmembrane currents (Torella *et al.*, 2004; Rota *et al.*, 2005; Rota *et al.*, 2007; Ferreira-Martins *et al.*, 2009; Signore *et al.*, 2013). Pipettes were pulled by means of a vertical (PB-7, Narishige), or horizontal (P-1000, Sutter Instrument) glass microelectrode pullers; when filled with intracellular solution pipettes had a resistance of 1-2 MΩ.

Action potential measurements. For action potential (AP) measurements, current-clamp mode was employed (Rota & Vassalle, 2003; Rota *et al.*, 2007; Signore *et al.*, 2013). Cells were stimulated with current pulses 1.5 times threshold. Myocytes were bathed with Tyrode solution. The composition of the pipette solution was (in mM): NaCl 10, KCl 113, $MgCl_2$ 0.5, K_2-ATP 5, glucose 5.5, HEPES 10, EGTA 10, $CaCl_2$ 1 (pH 7.2 with KOH). To test the effects of ion channels modulators on the electrical properties of myocytes, APs were continuously recorded for the same cell before and after exposure to agonist or inhibitors. The following compound were used in current clamp experiments: ranolazine (10 μM), mexiletine (10 μM), anemonia toxin II (1 nM) (Sicouri *et al.*, 1997; Rota & Vassalle, 2003; Sossalla *et al.*, 2008; Sossalla *et al.*, 2011; Wagner *et al.*, 2011; Wu *et al.*, 2011; Gao *et al.*, 2013; Fischer *et al.*, 2015), 4-aminopyridine (4-AP, 0.5 mM) (Brouillette *et al.*, 2004; Rota *et al.*, 2007; Liu *et al.*, 2011).

Measurements of voltage-gated K^+ currents. Voltage-gated outward K^+ Kv currents were assessed in voltage-clamp mode with a previously reported protocol (Liu *et al.*, 2011), to dissect K^+ currents with rapid activation and fast (I_{to}), intermediate ($I_{K,slow1}$) and slow ($I_{K,slow2}$) kinetics of inactivation, together with a sustained (non-inactivating) component (I_{ss}) (Nerbonne & Kass, 2005; Liu *et al.*, 2011). Cells were bathed with a modified Tyrode solution containing (in mM) NaCl 140, KCl 4, $MgCl_2$ 1, HEPES 10, Glucose 10, $CaCl_2$ 1.2 and 0.3 mM $CdCl_2$ to block L-type Ca^{2+} current (pH 7.4, adjusted with NaOH) (Rota *et al.*, 2007; Liu *et al.*, 2011). The composition of the pipette solution was (in mM): NaCl 5, KCl 20, K-aspartate 120, $MgCl_2$ 1, Mg-ATP 5, EGTA 10, HEPES 10 (pH 7.2 with KOH) (Liu *et al.*, 2011). Following membrane capacitance and series resistance compensation, Kv currents were activated using depolarizing voltage steps from -80 mV to +60 mV, 25 sec in duration. Interpulse interval was 60 sec. I_{to}, $I_{K,slow1}$, $I_{K,slow2}$ and I_{ss} amplitude and time constant were obtained by fitting the current decay during the depolarizing step with a tri-exponential function using Clampfit 10 software (Liu *et al.*, 2011). Currents were normalized by C_m.

Measurements of voltage-gated Na^+ currents. The late Na^+ current (I_{NaL}) was measured in voltage-clamp mode (Sossalla *et al.*, 2011; Wagner *et al.*, 2011; Wu *et al.*, 2011). Myocytes were bathed with a modified Tyrode solution in which KCl was replaced with CsCl and 4 μM nicardipine was added to block L-type Ca^{2+} current. Composition of the pipette solution was

(in mM): NaCl 10, CsCl 113, $MgCl_2$ 0.5, Tris-ATP 5, glucose 5.5, HEPES 10, EGTA 5, and tetraethylammonium chloride 20 (pH 7.2 with CsOH). Myocytes were held at V_h of -120 mV and I_{NaL} was elicited using 500 ms depolarizing pulses to -30 mV. The pulse was preceded by a 5 ms pre-pulse to +50 mV in order to optimize voltage control (Sossalla *et al.*, 2011). Interpulse interval was 5 sec. I_{NaL} was measured as inward current decaying during the 500 ms depolarizing step to -30 mV, excluding the initial 20 ms of the depolarizing step. I_{NaL} was normalized by C_m. I-V relations were determined applying depolarizing steps 500 ms in duration from V_h -120 mV in 5 mV increments. The family of depolarizing steps was preceded by a 20 ms-preconditioning step to -50 mV to activate the fast Na^+ current. Interpulse interval was 5 sec. I_{NaL} amplitude was measured as inward current decaying during the 500 ms depolarizing at various test potentials, excluding the initial 20 ms. I_{NaL} was normalized by C_m.

Equilibrium potential for Na^+ at 25°C was calculated by the Nernst equation:

$E_{Na} = 25.69 \cdot \ln ([Na^+]_o / [Na^+]_i)$.

At each potential tested (V_m), Na^+ conductance (g) was calculated as:

$g = I_{NaL} / (V_m - E_{Na})$,

where I_{NaL} is the amplitude of the late Na^+ current at V_m.

Conductance-voltage relations were plotted and fitted with Boltzmann function:

$g = g_{max} / 1 + \exp [(V_{1/2G} - V_m) / k_G)]$,

where g_{max} corresponds to maximal conductance, $V_{1/2G}$ the potential at which conductance is halfway between 0 and g_{max}, and k_G the slope of the conductance curve.

Values of normalized Na^+ conductance ($G = g / g_{max}$) were plotted to obtain activation curves; half maximal activation potential ($V_{1/2G}$) and slope of the activation curve (k_G) were derived by fitting the data with Boltzmann equation:

$G = \{1 + \exp[(V_{1/2G} - V_m) / k_G]\}^{-1}$,

A two-pulse protocol was utilized to assess the voltage dependence of steady state inactivation of I_{NaL}. Prepulses were introduced to depolarize the cell to different membrane voltages ranging from −120 to +50 mV for 500 ms, in 10 mV increments. Each prepulse was followed by a single 500 ms test pulse, which depolarized the cell to -30 mV. Different prepulses were applied at 5 sec intervals. Values of normalized Na^+ conductance ($G = g / g_{max}$) were plotted with V_m relative to the preconditioning steps to determine steady state inactivation curves, fitted with a Boltzmann equation, as indicated above.

Additionally, I_{NaL} was assessed as tetrodotoxin (TTX)-sensitive current using depolarizing steps to -40 mV, 520 ms in duration from holding potential of -80 mV. The protocol was recorded for the same cell in Tyrode solution and following perfusion with 10 µM TTX (Sigma, Enzo Life Sciences). Scout depolarizations 10 mV in increments from V_h -80 mV and 5 sec interpulse interval were applied every 1-2 minutes to evaluate the effects of TTX and experimental conditions. Difference current was obtained by subtracting traces recorded in TTX from those measured in Tyrode. The slowly decaying TTX-sensitive current was evaluated by quantifying the inward current decaying over the 520 ms depolarization, excluding the initial 20 ms of the depolarizing step. Currents were normalized by C_m. For these measurements, pipette solution was comparable to the one employed for AP measurements.

The fast Na^+ current (I_{Na}) was measure in voltage-clamp mode (Vaidyanathan *et al.*, 2013). Myocytes were bathed with a modified Tyrode solution of the following composition (in mM): NaCl 5, $MgCl_2$ 1, $CaCl_2$ 1, $CdCl_2$ 0.1, HEPES 20, glucose 11, and CsCl 132.5 (pH 7.4 with CsOH). The composition of the pipette solution was (in mM): NaCl 5, CsF 135, EGTA 10, MgATP 5, and HEPES 5 (pH 7.2 with CsOH) (Vaidyanathan *et al.*, 2013). I-V relations were determined applying depolarizing steps 200 ms in duration from V_h -120 mV in 5 mV increments. Interpulse interval was 3 sec. I_{Na} amplitude was measured as the current difference between the inward peak current and the current at the end of the 200 ms step. I_{Na} was normalized by C_m.

A two-pulse protocol was utilized to assess the voltage dependence of steady state inactivation of I_{Na}. Prepulses were introduced to depolarize the cell to different membrane voltages starting from −140 mV for 300 ms, in 5 mV increments. Each pre-pulse was followed by a single 30 ms test pulse, which depolarized the cell to -40 mV. Values of normalized Na^+ conductance ($G = g / g_{max}$) were plotted with V_m relative to the preconditioning steps to compute the steady state inactivation curves, which were fitted with a Boltzmann equation, as indicated above.

In voltage-clamp experiments in which Na^+ currents were modulated pharmacologically with mexiletine (10 µM for quantification of the effects on I_{Na}; 30 µM for qualitative effects on I_{NaL}) or anemonia toxin-II (1 nM), depolarizing pulses between -60 mV and 0 mV, 10 mV in increments, 5 sec interpulse interval, from V_h -70 mV or -90 mV (see legend to figure for

details) were tested every 1-2 min to evaluate the effects of drugs and experimental conditions.

Measurements of L-type Ca^{2+} current. The L-type Ca^{2+} current (I_{CaL}) was measured in voltage-clamp mode (Torella *et al.*, 2004; Rota *et al.*, 2005; Rota *et al.*, 2007). Myocytes were bathed with a modified Na^+-K^+-free Tyrode solution of the following composition (in mM): N-methyl-D-glucamine (NMDG) 140, CsCl 4, $MgCl_2$ 1, HEPES 5, glucose 5.5, $CaCl_2$ 1, and 4-aminopyridine 2 (pH 7.4 with CsOH). The composition of the pipette solution was (in mM): NMDG 10, CsCl 113, $MgCl_2$ 0.5, Tris-ATP 5, glucose 5.5, HEPES 10, EGTA 5 and TEA-Cl 20 (pH 7.2 with CsOH). I_{CaL} current-voltage (I-V) relation, conductance and activation properties were determined applying depolarizing steps 300 ms in duration from V_h -70 mV in 10 mV increments. I_{CaL} amplitude was measured as the current difference between the peak inward current at the beginning of the step and the current at the end of the 300 ms pulse. I_{CaL} was normalized by C_m.

Equilibrium potential for Ca^{2+} was defined by the intercept of the I-V relation to the zero-current axis. A linear fitting of the positive potential portion of the I-V relation was employed for this determination. At each potential tested (V_m), Ca^{2+} conductance (g) was calculated as:

$g = I_{CaL} / (V_m - E_{Ca})$,

where I_{CaL} is the amplitude of the L-type Ca^{2+} current at V_m.

Conductance-voltage relations were plotted and fitted with Boltzmann function. Values of normalized Ca^{2+} conductance ($G = g / g_{max}$) were plotted to obtain activation curves; half maximal activation potential ($V_{1/2G}$) and slope of the activation curve (k_G) were derived by fitting the data with Boltzmann equation.

A two-pulse protocol was utilized to assess the voltage dependence of steady state inactivation of I_{CaL}. Prepulses were introduced to depolarize the cell to different membrane voltages starting from −80 mV for 300 ms, in 10 mV increments. Each pre-pulse was followed by a single 300 ms test pulse, which depolarized the cell to 0 mV. Values of normalized Ca^{2+} conductance ($G = g / g_{max}$) were plotted with V_m relative to the preconditioning steps to determine steady state inactivation curves, fitted with a Boltzmann equation, as indicated above.

Inactivation time course of I_{CaL} was studied with a 300 ms depolarizing pulse at 0 mV (Rota *et al.*, 2007). Traces were fitted between the inward peak and the end of the 300 ms pulse to 0 mV with a bi-exponential function (Rota & Vassalle, 2003):

$I_{(t)} = A_f \cdot \exp(-t/\tau_f) + A_s \cdot \exp(-t/\tau_s) + C$,

where A_f and A_s are, respectively, the fraction of the fast and slow inactivating components, and C is the offset constant.

AP-clamp and Ca^{2+} transients. For AP-clamp experiments, Ca^{2+} levels in patch-clamped myocytes was assessed as fluorescence signal intensity of Fluo-loaded cells using a photomultiplier, and a photon to voltage converter (IonOptix) connected to the patch-clamp A/D converter (Rota *et al.*, 2007; Signore *et al.*, 2013). Cells were bathed in Tyrode solution and pipette solution was comparable to the one employed for AP measurements with the omission of EGTA and $CaCl_2$.

Fluo signals were expressed as normalized fluorescence (F/F_0), where F_0 is the diastolic fluorescent level subtracted by the background signal measured in the region adjacent to the cell (Signore *et al.*, 2013). Duration of Ca^{2+} transient decay was evaluated at 10%-90% and obtained results from different cells were averaged and fitted with a mono-exponential function:

$F_{(t)}/F_0 = (F_P/F_0 - F_0/F_0) \cdot \exp(-t/\tau) + F_0/F_0$,

where F_P and F_0 are, respectively, the fluorescence relative to the peak and diastolic phase of the Ca^{2+} transient.

Isometric force in papillary muscles. Papillary muscles were dissected from the mouse LV and mounted in a horizontal tissue bath (Steiert, Hugo Sachs Elektronik-Harvard Apparatus) connected to a force transducer (F10, Harvard Apparatus)(Signore *et al.*, 2013). Muscles were superfused with KHB solution at 37°C. The myocardium was stimulated by two platinum electrodes employing field stimulation (isolated stimulator output: frequency 6 Hz; pulse duration 2 ms; intensity 1.5-fold threshold; UISO, Hugo Sachs Elektronik-Harvard Apparatus). Each muscle was stretched to the length at which force of contraction was maximal. Muscle preparations were allowed to equilibrate for at least 30 min. Developed tension was measured isometrically with the force transducer attached to a Bridge Amp (ADInstruments) and a 4 kHz A/D converter (Power Lab 4/30, ADInstruments). Tension

signal was recorded using LabChart 7 Pro software (ADInstruments) and analyzed with LabChart 8. Time to 50% and 90% relaxation are expressed with respect to the beginning of the twitch. Based on the premise that each muscle had a cylindrical shape, force measurements were normalized by the cross sectional area of the muscle (mN/mm^2). Digital images of sections were acquired using micro-zoom system microscopes (MVX10 and SZX16, Olympus) and a sCMOS camera (pco.edge) or a CCD camera (DP73, Olympus), and analyzed by ImageJ software (Signore *et al.*, 2013).

Passive diastolic tension was examined by progressively stretching muscles stimulated at 6 Hz, beginning from near slack length (L_0) to the length at which the muscle developed maximal twitch tension (L_{max}). Diastolic length-tension relations were plotted and fitted with a second-order polynomial equation:

$$dT_{(L/Lmax)}=a\cdot(L/L_{max})+b\cdot(L/L_{max})^2,$$

where dT is diastolic tension and L is the length of the muscle.

The late Na^+ current was blocked with ranolazine (10 μM, Sigma) or mexiletine (10 μM, Sigma), or enhanced with anemonia toxin II (10 nM, Sigma)(Sicouri *et al.*, 1997; Sossalla *et al.*, 2011; Wagner *et al.*, 2011; Fischer *et al.*, 2015). 4-aminopyridine (1 mM, Sigma) was employed to inhibit Kv currents and induce prolongation of myocyte AP)(Brouillette *et al.*, 2004; Rota *et al.*, 2007; Liu *et al.*, 2011). Twitch properties were evaluated in young and old muscles at baseline and following superfusion with agonists or inhibitors. Muscles exposed to excessive stretching and displaying unstable twitches were excluded from the analysis. For evaluation of diastolic tension-length relations, muscles were superfused with KHB, mexiletine or anemonia toxin II and then progressively stretched under continuous electrical stimulation.

Quantitative RT-PCR. Total RNA was extracted from isolated mouse LV myocytes utilizing TRIZOL reagent (Invitrogen). cDNA was obtained from 1 μg total RNA using MultiScribe reverse transcriptase kit (Applied Biosystems). Real-time RT-PCR was performed with primers designed using the Vector NTI Advance 11 (Invitrogen) software (Ferreira-Martins *et al.*, 2009; Goichberg *et al.*, 2011; Signore *et al.*, 2013). The sequences of primers are indicated in Table 1. The StepOnePlus Real-Time PCR system (Applied Biosystems) was employed for quantitative RT-PCR. In each case, cDNA was combined with Power SYBR Green Master Mix (Applied Biosystems) in a 10 μl reaction. Cycling conditions were as

follow: 95°C for 10 min followed by 40 cycles of amplification (95°C denaturation for 15 sec, 60°C annealing and extension for 1 min). The melting curve was then obtained. C_t values were normalized with respect to β-2-microglobulin (β2m). To avoid the influence of genomic contamination, forward and reverse primers for each gene were located in different exons. PCR products were run on 3% agarose/1x TBE gel to confirm the specificity of the reaction. Total RNA extracted from mouse brain and skeletal muscle was employed as controls. For fibrotic markers (Hao *et al.*, 2011), RNA was extracted from LV tissue. C_t values were normalized with respect to hypoxanthine guanine phosphoribosyl transferase (Hprt) (Hao *et al.*, 2011).

Western blotting. Whole protein extracts from pellets of isolated LV myocytes or LV myocardium were prepared using RIPA buffer (Sigma), supplemented with a cocktail of protease inhibitors (Roche) and phosphatase inhibitors (Sigma). Equivalent of 15 μg of proteins were separated on SDS-PAGE, transferred onto PVDF membrane, blocked with 5% BSA and exposed to the antibodies listed in Table 2. Horseradish peroxidase-conjugated secondary antibodies (Cell Signaling Technology) and Pierce ECL 2 Western Blotting chemiluminescent substrate (Thermo Scientific) were utilized for signal detection (Signore *et al.*, 2013). Western blotting protocols with various antibodies were optimized before quantitative analysis. Optical density of bands was measured using ImageJ and normalized by the expression of GAPDH.

Data Analysis. Data are presented as median and interquartile ranges (IQR) or mean ± s.e.m. Linear and nonlinear regressions were calculated with Prism 6.0c software, and parameters are reported in Table 3. Statistical analysis was performed using SigmaPlot 11.0 software. Data were initially tested for normality (Shapiro-Wilk) and equal variance for assignment to parametric or non-parametric analysis. Parametric test included Student's *t*-test or ANOVA followed by Bonferroni test for non-paired comparison between two or among multiple groups, respectively. For paired statistical analysis, paired *t*-test or One Way Repeated Measures Analysis of Variance followed by Bonferroni test were employed for two groups or multiple comparisons, respectively. When normality or equal variance were not met, non-parametric analysis was performed using Mann-Whitney Rank Sum Test or Kruskal-Wallis One Way Analysis of Variance on Ranks followed by Dunn's Method, for non-

paired comparison between two or among multiple groups, respectively. Wilcoxon Signed Rank test or Friedman Repeated Measures Analysis of Variance on ranks, were employed for paired comparison between two or among multiple groups, respectively. For categorical data analysis Fisher's exact or Chi Square tests were used. $P<0.05$ was considered significant.

Results

Aging impairs ventricular performance

To determine the effects of aging on left ventricular (LV) function, echocardiographic measurements, including speckle-tracking and Doppler protocols, were combined with MRI and invasive hemodynamics. Mice from 3 to 35 months of age were studied. Systolic blood pressure, evaluated by tail-cuff plethysmography, was comparable in un-anesthetized mice at 3, 25 and 30 months of age, indicating that systemic blood pressure did not increase with aging in this model (**Figure 3**). EF was preserved at 24 months, when an increase in LV mass was observed. Then, EF slightly decreased at 30 months together with an increase in cavitary volume, whereas stroke volume and cardiac output were maintained (**Figure 4**). These properties were confirmed by cardiac MRI (Nahrendorf *et al.*, 2006) (**Figure 5**). Additionally, speckle-tracking strain echocardiographic imaging demonstrated that radial and longitudinal strain and strain rates were altered in old mice (**Figure 6**). Importantly, following blockade of the autonomous nervous system (D'Souza *et al.*, 2014), differences in EF observed between mice at 3-4 and 30-31 months of age were attenuated (**Figure 7**), indicating that alterations in cardiac performance with age are partly dictated by an imbalance in autonomic nerve activity, as reported previously (White *et al.*, 1994; Xiao *et al.*, 1994).

To define the diastolic properties of the LV, transmitral flow Doppler echocardiography was employed (Ram *et al.*, 2011). Mice at 25 months of age and older presented reduced passive filling velocity (E wave), increased active filling (A wave), lower E/A ratio and prolonged timing parameters (**Figure 8**). Hemodynamically, an increase in end-diastolic pressure occurred at 24-25 months and preceded the deterioration in systolic performance; in fact, LV systolic pressure, developed pressure, and +dP/dt decreased significantly in mice at 30-35 months of age, although stroke volume and cardiac output were preserved (**Figure 9**). In contrast, reduced -dP/dt, prolonged time constant of pressure decay (tau), and increased end-diastolic pressure were already present at 24-25 months documenting a decline in diastolic function in the absence of systolic defects. Additionally, occlusion of the inferior vena cava or aortic arch, which alters LV loading, showed that the slope of the LV end-diastolic PV relation was 2.5-fold steeper in old than in young animals, pointing to alterations in ventricular compliance with age (**Figure 9**). The deterioration of diastolic and

systolic hemodynamic indices in mice at 30 months and older was also observed following complete autonomic blockade (**Figure 10**). Thus, these in vivo data emphasize the defective kinetics of contraction and relaxation, and the impaired diastolic filling of the old heart, which anticipate, chronologically, the compromise of systolic function.

LV weight was similar in mice at 3 and 11 months of age, and increased modestly at 23-25 months. Myocardial hypertrophy became apparent in the senescent heart at 28-34 months (**Figure 11a**), when cardiac performance was depressed. Structurally, cell size was enlarged by 34% in myocytes from senescent mice, together with changes in the expression of fibrotic markers (Hao *et al.*, 2011) and a relatively modest increase in myocardial interstitial fibrosis, from 0.2% at 2-3 months of age to 0.3% at 29-30 months (**Figure 11b-11e**). Collectively, these results support the notion that the aging myopathy is characterized by an initial decline of diastolic function, dictated by protracted kinetics of contraction and relaxation. These alterations are then accompanied by intervening defects in systolic performance together with development of myocyte and myocardial hypertrophy.

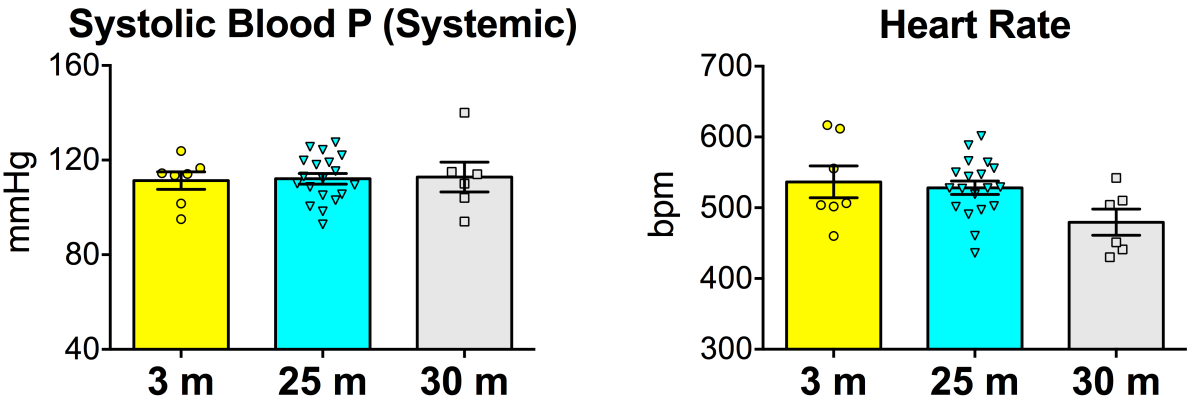

Figure 3. Systemic pressure is preserved in aging mice. Quantitative data for non-invasive systolic blood pressure (left) and heart rate (right) evaluated in conscious male mice at 3 months (3 m, *n* = 7), 25 months (25 m, *n* = 19), and 30 months (30 m, *n* = 6) are shown as mean ± s.e.m. and scatter plots. Data was not significantly different (one-way ANOVA).

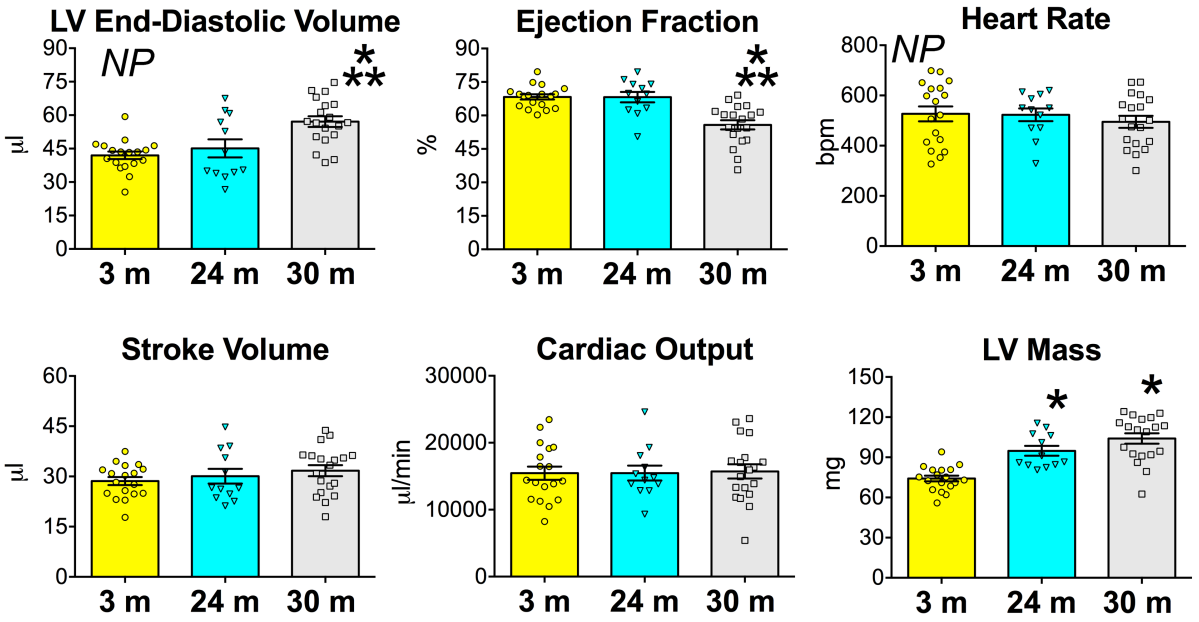

Figure 4. Cardiac function is depressed in senescent mice. Anatomical and functional parameters evaluated by echocardiography in aging mice. Data for male mice at 3 months (3 m, *n* = 18), 24 months (24 m, *n* = 12), and 30 months (30 m, *n* = 19) are shown as mean ± s.e.m. and scatter plots. **P*<0.05 versus 3 m; ***P*<0.05 versus 24 m (one-way ANOVA with Bonferroni's *post hoc* test and Kruskal-Wallis one-way ANOVA on ranks with Dunn's *post hoc* test); *NP*: non-parametric analysis.

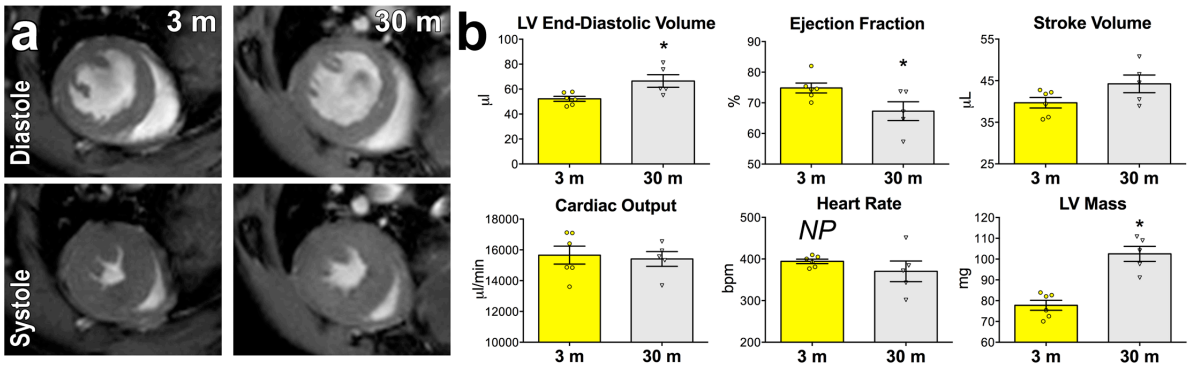

Figure 5. Aging is associated with a progressive deterioration of diastolic function. (**a**) Short axis views by MRI of young (3 months, 3 m) and old (30 months, 30 m) male mouse hearts. (**b**) Quantitative data obtained by MRI imaging for 3 months (3 m, *n* = 6) and 30 months (30 m, *n* = 5) male mice are shown as mean ± s.e.m. and scatter plots. **P*<0.05 versus 3 m (Student's *t*-test and Mann-Whitney rank sum test); *NP*: non-parametric analysis.

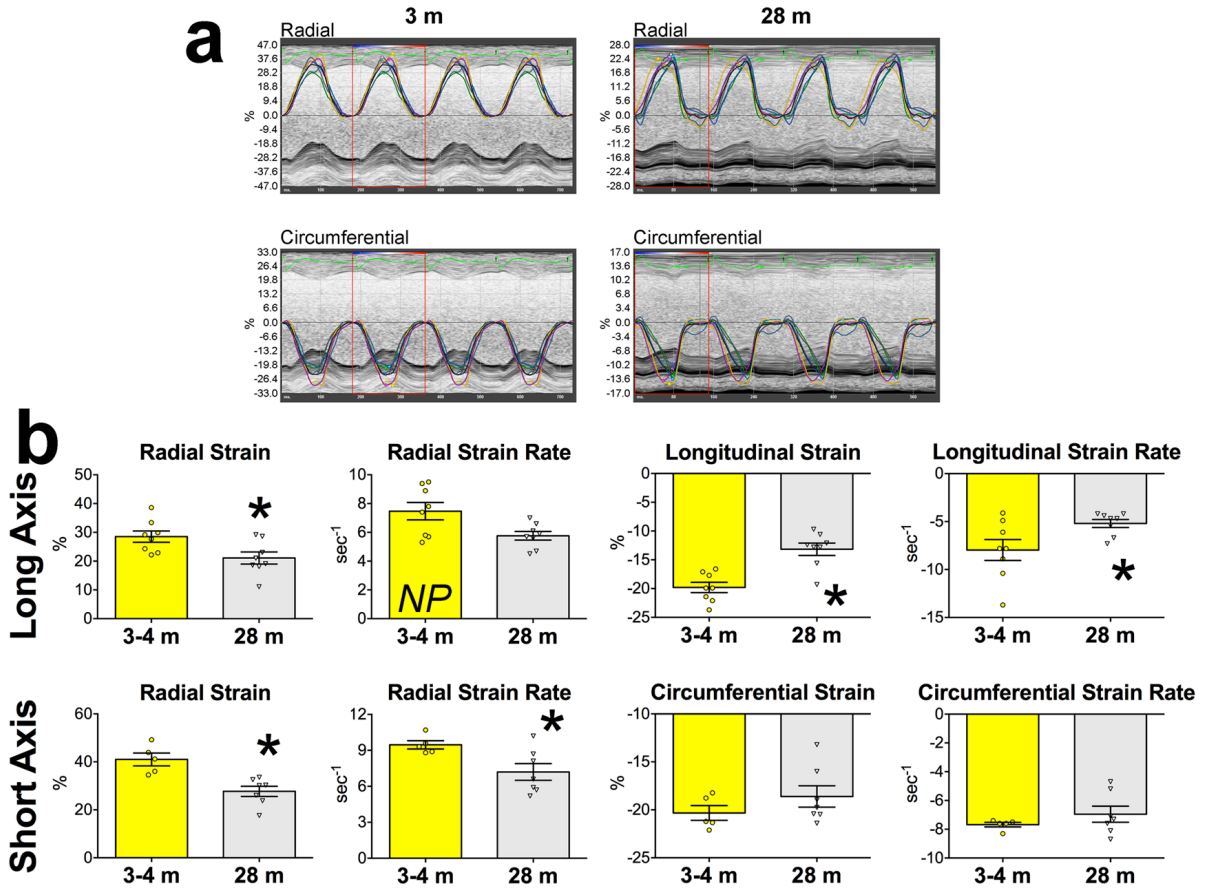

Figure 6. Speckle tracking-based strain analysis for the evaluation of cardiac function in the aging heart. (**a**) Radial and circumferential strain curves for parasternal short axis images in male mice at 3 months (3 m) and 28 months (28 m) of age. (**b**) Quantitative data of speckle tracking-based analysis for male mice at 3-4 months (3-4 m, *n* = 5-8) and 28 months (28 m, *n* = 7-8) are shown as mean ± s.e.m. and scatter plots. **P*<0.05 versus 3-4 m (Student's *t*-test and Mann-Whitney rank sum test); *NP*: non-parametric analysis.

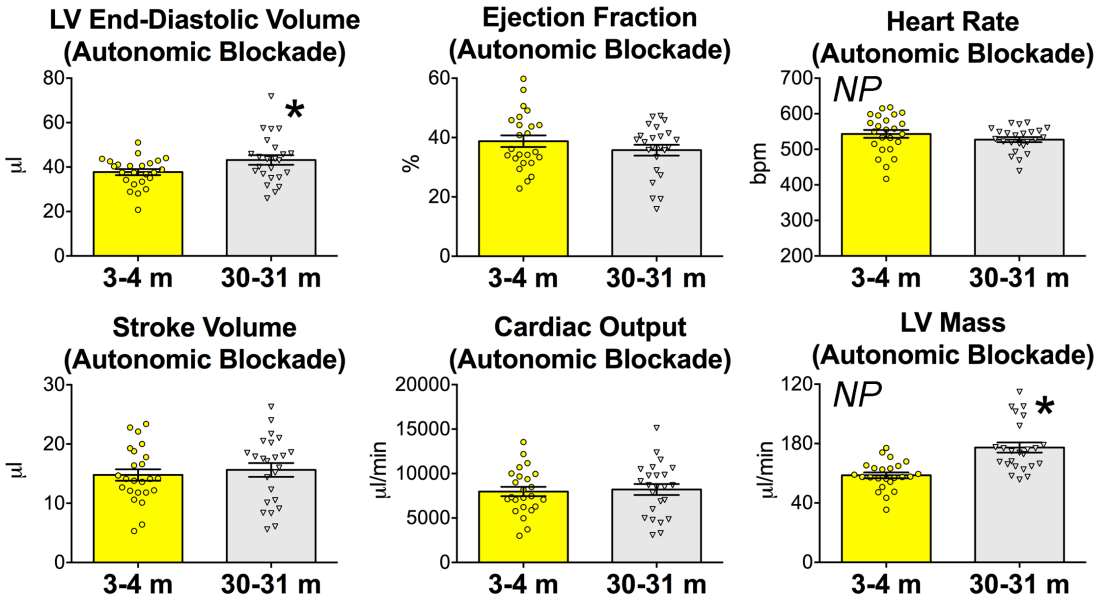

Figure 7. Blockade of the autonomous nervous system attenuates defects in cardiac function in aged mice. Anatomical and functional parameters evaluated by echocardiography in aging mice following complete block of the autonomic nervous system with atropine (0.5 mg kg^{-1} body weight, i.p.) plus propranolol (1 mg kg^{-1} body weight, i.p.). Data for male mice at 3-4 months (3-4 m, *n* = 24) and 30-31 months (30-31 m, *n* = 24) are shown as mean ± s.e.m. and scatter plots. **P*<0.05 versus 3-4 m (Student's *t*-test and Mann-Whitney rank sum test); *NP*: non-parametric analysis.

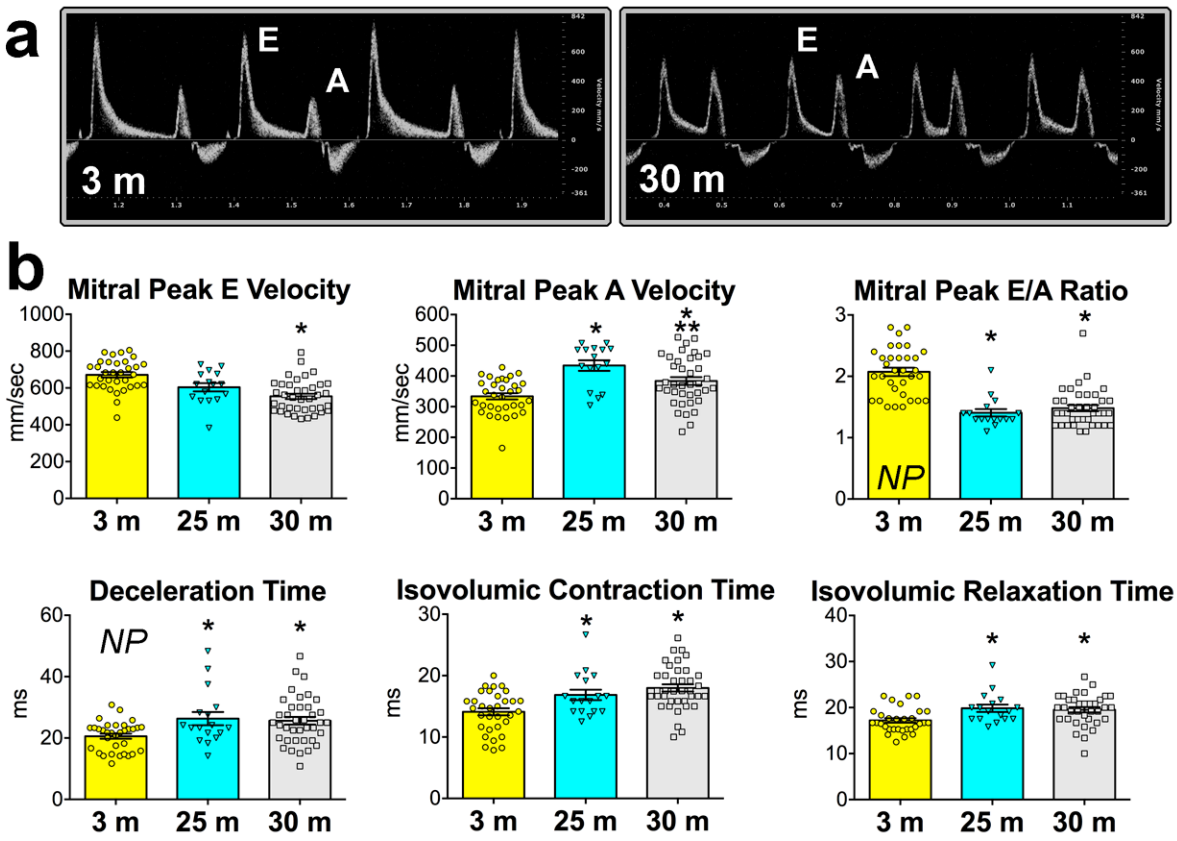

Figure 8. Aging is associated with a progressive deterioration of diastolic function. (**a**) Transmitral flow Doppler echocardiograms obtained from young (3 months, 3 m) and old (30 months, 30 m) male mice show early passive filling (E) and active filling (A) waves. (**b**) Quantitative data for male mice at 3 months (3 m, *n* = 33), 25 months (25 m, *n* = 19), and 30 months (30 m, *n* = 38) are shown as mean ± s.e.m. and scatter plots. m: months. **P*<0.05 versus 3 m, ***P*<0.05 versus 25 m (one-way ANOVA with Bonferroni's *post hoc* test and Kruskal-Wallis one-way ANOVA on ranks with Dunn's *post hoc* test); *NP*: non-parametric analysis.

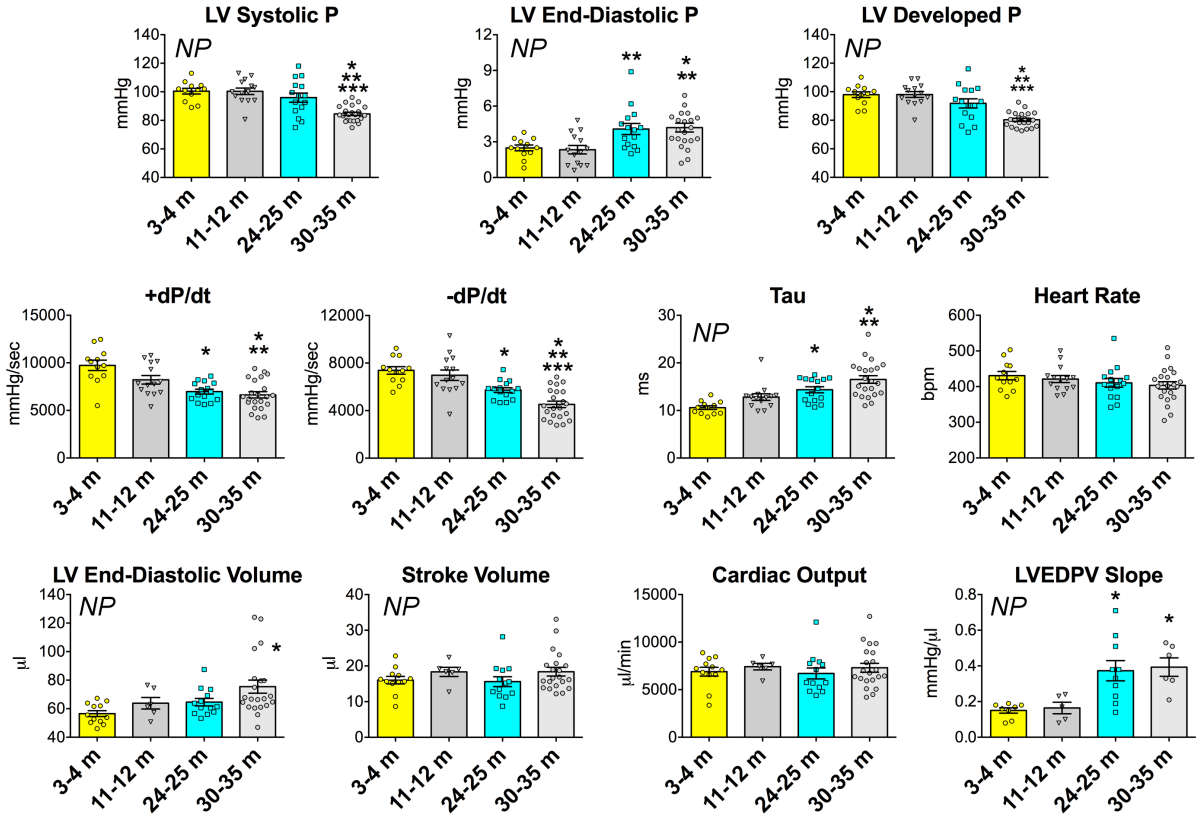

Figure 9. Aging is associated with a progressive deterioration of cardiac function. Hemodynamic and volumetric parameters obtained by pressure-volume (PV) catheterization in male mice. Data for animals at 3-4 months (3-4 m, *n* = 12), 11-12 months (11-12 m, *n* = 14), 24-25 months (24-25 m, *n* = 15), and 30-35 months (30-35 m, *n* = 19) are shown as mean ± s.e.m. and scatter plots. P: pressure; LVEDPV: LV end-diastolic PV relation; LVESPV: LV end-systolic PV relation. **P*<0.05 versus ~3 m, ***P*<0.05 versus ~12 m, ****P*<0.05 versus ~25 m (one-way ANOVA with Bonferroni's *post hoc* test and Kruskal-Wallis one-way ANOVA on ranks with Dunn's *post hoc* test); *NP*: non-parametric analysis.

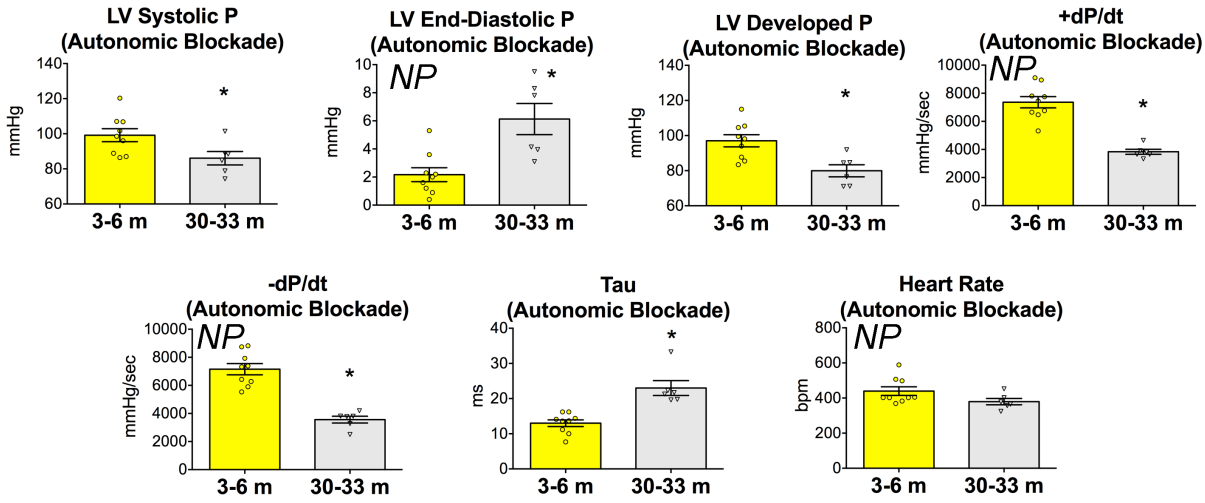

Figure 10. Blockade of the autonomous nervous system does not abrogate diastolic and systolic defects in aged mice. Functional parameters evaluated by LV hemodynamics in aging mice following complete block of the autonomic nervous system with atropine (0.5 mg kg^{-1} body weight, i.p.) plus propranolol (1 mg kg^{-1} body weight, i.p.). Data for male mice at 3-4 months (3-6 m, *n* = 9) and 30-33 months (30-33 m, *n* = 6) are shown as mean ± s.e.m. and scatter plots. **P*<0.05 versus 3-6 m (Student's *t*-test and Mann-Whitney rank sum test); *NP*: non-parametric analysis.

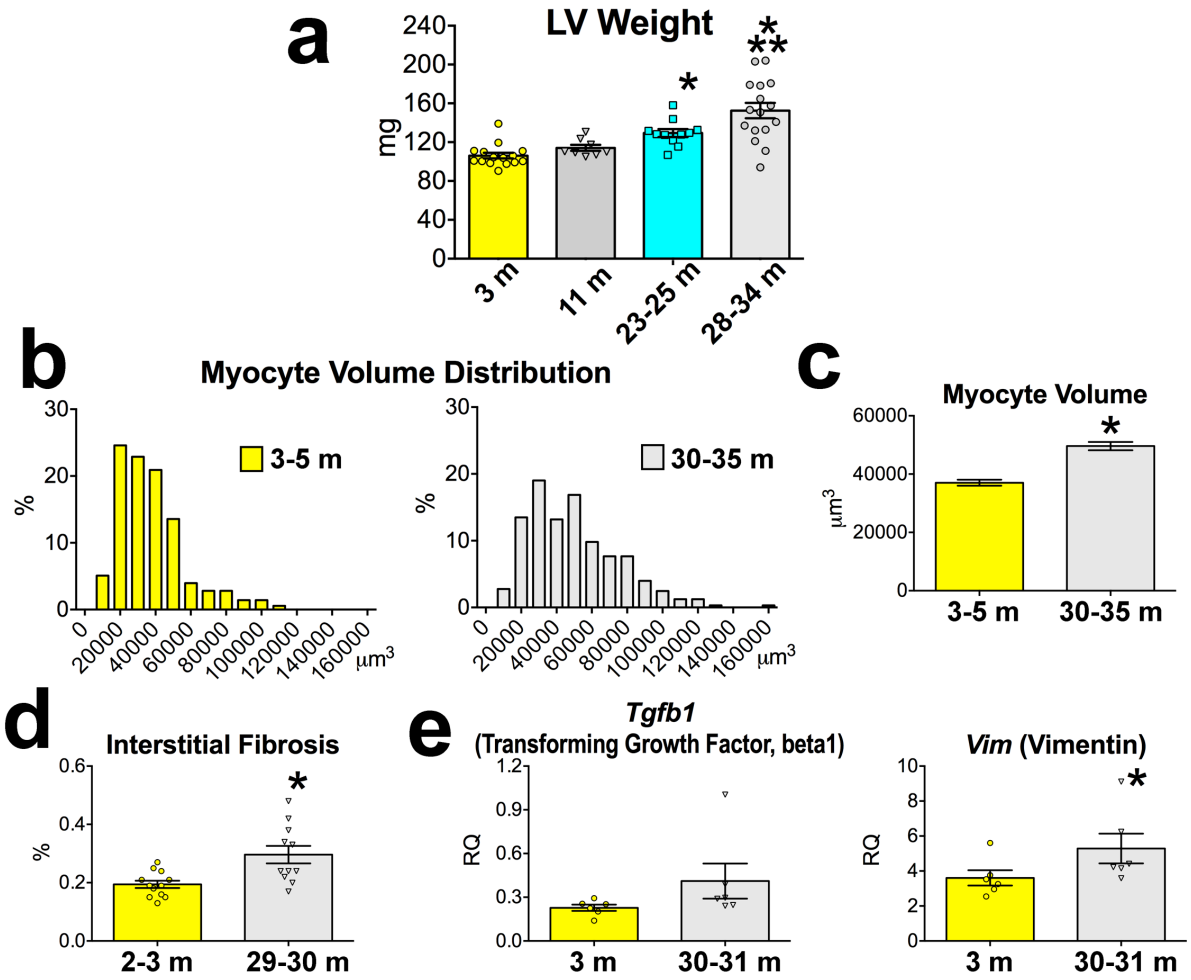

Figure 11. Aging and cardiac structure. (**a**) LV weights for male mice at 3 months (3 m, *n* = 15), 11 months (11 m, *n* = 8), 23-25 months (23-25 m, *n* = 11), and 28-34 months (28-34 m, *n* = 16) are shown as mean ± s.e.m. and scatter plots. **P*<0.05 versus 3 m; ***P*<0.05 versus 11 m; ***P*<0.05 versus 23-25 m (Kruskal-Wallis one-way ANOVA on ranks with Dunn's *post hoc* test). (**b**) Volume distribution of cardiomyocytes from male mice at 3-5 months (3-5 m, *n* = 354 cells from 5 hearts) and 30-35 months (30-35 m, *n* = 326 cells from 5 hearts). (**c**) Data presented in **b** are shown as mean ± s.e.m. and scatter plots. **P*<0.001 versus 3-5 m (Mann-Whitney rank sum test). (**d**) Quantitative measurements of interstitial fibrosis in male mice at 2-3 months (2-3 m, *n* = 12), 29-30 months (29-30 m, *n* = 11) are shown as mean ± s.e.m. and scatter plots. **P*<0.01 versus 2-3 m (Mann-Whitney rank sum test). (**e**) Quantitative data for the transcript levels of transforming growth factor, beta1 (Tgfb1) and vimentin (Vim) in the LV of male mice at 3 months (3 m, *n* = 6) and 30-31 months (30-31 m, *n* = 6) are shown as mean ± s.e.m. and scatter plots. **P*<0.05 versus 3 m (Mann-Whitney rank sum test).

Aging delays myocardial and myocyte electrical recovery

Surface ECG was employed to assess the electrical properties of the heart in mice at 3, 11-13, 25, and 30-34 months of age. PR and QT intervals were prolonged in mice at 25 months and older (**Figure 12a and 12b**), indicating that delays in atrioventricular conduction, ventricular activation and repolarization occurred with age. These changes were also observed by telemetry in conscious animals and persisted following autonomic blockade (**Figure 12c and 12d**). To exclude the confounding effects of circulating neurohumoral factors, an isolated organ preparation was employed (Signore *et al.*, 2013). Again, old hearts showed delayed PR and QT intervals (**Figure 12e**). Additionally, epicardial monophasic action potentials, which reflect local cellular depolarization and repolarization, were recorded on the LV free wall (Signore *et al.*, 2013). AP duration (APD) was prolonged in old hearts (**Figure 13**), suggesting that defects in the electrical properties of the aging myocardium were mediated by alterations at the cellular level. Since repolarization delays are associated with electrical disturbances (Roden & Viswanathan, 2005; Signore *et al.*, 2013), the propensity of the aging heart to develop arrhythmias was assessed by a protocol of programmed electrical stimulation (PES) (Goichberg *et al.*, 2011; Signore *et al.*, 2013). Arrhythmic events were 2.6-fold more frequent in hearts 24 months of age and older (**Figure 14**).

The electrical properties of isolated LV myocytes were established by the patch-clamp technique (Rota *et al.*, 2007; Signore *et al.*, 2013). The duration of the AP (APD), measured at 90% (APD_{90}) of repolarization, was 1.8-fold longer in 26-30 month-old myocytes (**Figure 15**). The changes in APD detected in old myocytes were consistent with the 24% reduction in the maximal negative slope during repolarization (dV/dt_{min}). However, resting membrane potential, AP amplitude, and dV/dt_{max} were comparable in myocytes at all ages. These electrical parameters, obtained at 1 Hz pacing rate, were maintained at higher stimulation frequency (**Figure 16**). Collectively, myocardial aging is characterized by electrical disturbances and the prolongation of the AP in myocytes contributes to the delayed electrical recovery of the old heart.

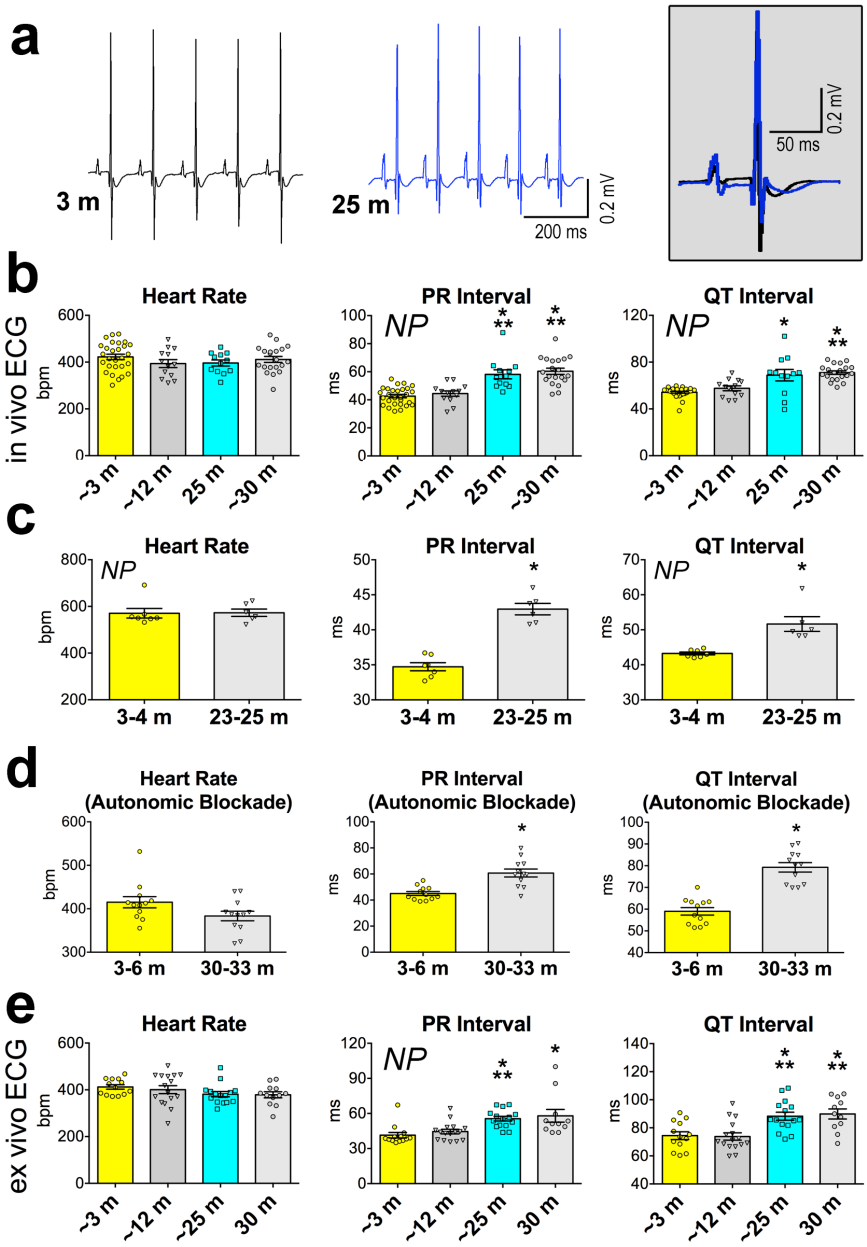

Figure 12. Aging leads to cardiac electrical abnormalities. (**a**) ECGs obtained from a young (3 months, 3 m; black traces) and old (25 months, 25 m; blue traces) mouse. Superimposed traces are shown in the inset. (**b, e**) Electrocardiographic parameters in anesthetized male mice (**b**) and explanted hearts (**e**) from animals at 3-4 months (~3 m, *n* = 28, 13), 11-13 months (~12 m, *n* = 13, 16), 25 and 24-27 months (25 and ~25 m, *n* = 12, 15), and 30-34 months (~30 m, *n* = 20, 12) are shown as mean ± s.e.m. and scatter plots. **P*<0.05 versus ~3 m, ***P*<0.05 versus ~12 m (one-way ANOVA with Bonferroni's *post hoc* test and Kruskal-Wallis one-way ANOVA on ranks with Dunn's *post hoc* test); *NP*: non-parametric analysis.
(**c**) Quantitative data for electrocardiographic parameters evaluated by telemetry in conscious male mice 3-4 months (3-4 m, *n* = 7) and 28-34 months (28-34 m, *n* = 6) are shown as mean ± s.e.m. and scatter plots. **P*<0.01 versus 3-4 m (Student's *t*-test and Mann-Whitney rank sum test); *NP*: non-parametric analysis**.** (**d**) Quantitative data for electrocardiographic parameters in anesthetized male mice 3-6 months (3-6 m, *n* = 12) and 30-33 months (30-33 m, *n* = 12) following complete block of the autonomic nervous system with atropine (0.5 mg kg^{-1} body weight, i.p.) plus propranolol (1 mg kg^{-1} body weight, i.p.). Data are as mean ± s.e.m. and scatter plots. **P*<0.05 versus 3-6 m (Student's *t*-test).

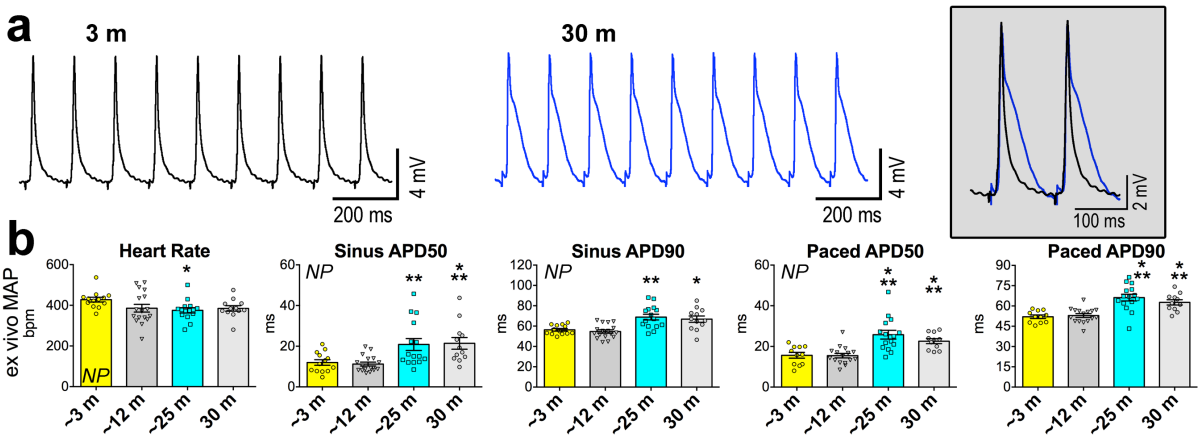

Figure 13. Aging prolongs the repolarization of the LV. (**a**) Epicardial monophasic action potentials (MAPs) obtained from perfused hearts of male mice at 3 months (3 m; black traces) and 30 months (30 m; blue traces). Superimposed traces are shown in the inset. (**b**) Data obtained during sinus rhythm (Sinus) or following stimulation at 8 Hz (Paced) in hearts from male mice at 3-4 months (~3 m, *n* = 11), 11-13 months (~12 m, *n* = 16), 24-27 months (~25 m, *n* = 15), and 30 months (30 m, *n* = 11) are shown as mean ± s.e.m. and scatter plots. APD50: MAP duration at 50% repolarization; APD90: MAP duration at 90% repolarization. **P*<0.05 versus ~3 m, ***P*<0.05 versus ~12 m (one-way ANOVA with Bonferroni's *post hoc* test and Kruskal-Wallis one-way ANOVA on ranks with Dunn's *post hoc* test); *NP*: non-parametric analysis.

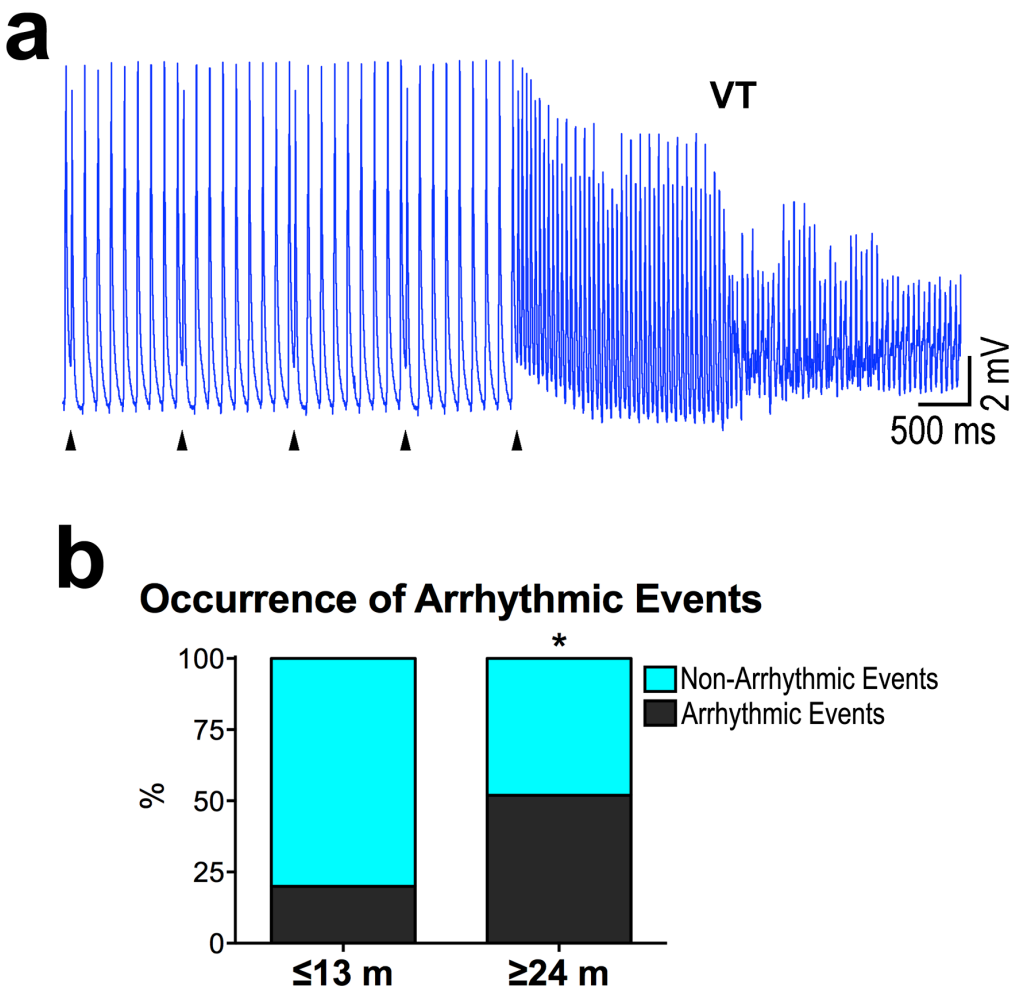

Figure 14. Aging is associated with electrical disturbances. (**a**) Monophasic action potentials (MAPs) during a protocol of programmed electrical stimulation (PES) in an old mouse. Reduced time interval for the stimulated premature beats (arrowheads) induces arrhythmia in an old heart. VT: ventricular tachycardia. (**b**) Quantitative data for hearts obtained from male mice at ≤13 months (≤13 m, *n* = 25) and ≥24 months (≥24 m, *n* = 27) are expressed as percentage of organs displaying arrhythmic events following PES. **P*<0.05 versus ≤13 m (Fisher exact test).

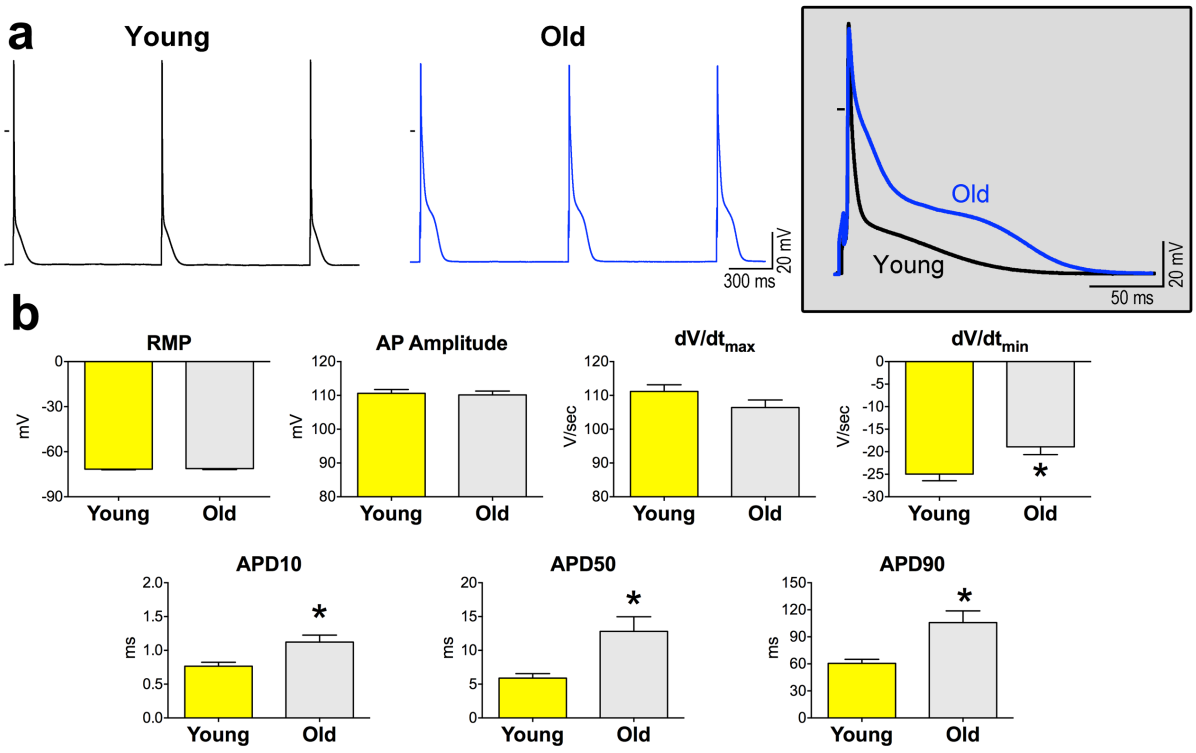

Figure 15. Aging prolongs the duration of the action potential in myocytes. (**a**) Action potentials (APs) recorded in isolated LV myocytes obtained from young (black traces) and old (blue traces) mice. Superimposed traces are shown in the inset. (**b**) Quantitative data for AP parameters obtained from myocytes isolated from male mice at 3 months (Young, *n* = 50 cells from 18 hearts) and 26-30 months (Old, *n* = 42 cells from 23 hearts) are shown as mean ± s.e.m. RMP: resting membrane potential. **P*<0.05 versus young (Mann-Whitney rank sum test).

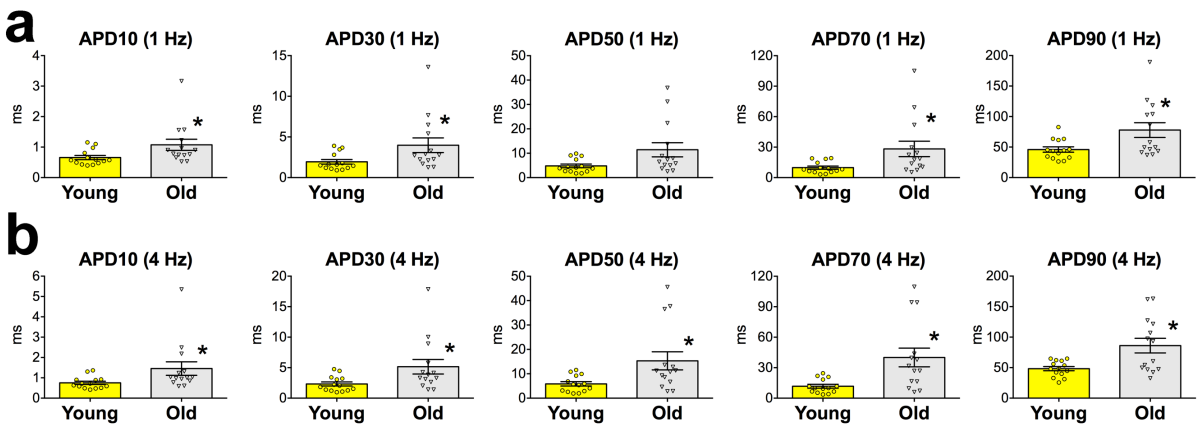

Figure 16. Old myocytes present protracted repolarization of the action potential. (**a**,**b**) Action potential repolarization time of myocytes isolated from male mice at 3 months (Young, *n* = 14 cells from 7 hearts) and 30-35 months (Old, *n* = 14 cells from 8 hearts) obtained at 1 Hz (**a**) and 4 Hz (**b**) pacing rate. Data are shown as mean ± s.e.m and scattered plots. **P*<0.05 versus Young (Mann-Whitney rank sum test).

Aging alters transmembrane ionic currents

Voltage-gated outward K^+ Kv currents are primary determinants of the AP repolarization and major factors in the electrophysiological remodeling occurring in myocytes during maturation, in pathological conditions and with age (Walker *et al.*, 1993; Wang & Duff, 1997; Wickenden *et al.*, 1997; Kaprielian *et al.*, 1999; Oudit *et al.*, 2001; Sah *et al.*, 2001; Brouillette *et al.*, 2004; Nerbonne & Kass, 2005). Kv currents comprise components with rapid activation and fast (I_{to}), intermediate ($I_{K,slow1}$) and slow ($I_{K,slow2}$) kinetics of inactivation, together with a sustained (non-inactivating) component (I_{ss}) (Nerbonne & Kass, 2005; Liu *et al.*, 2011). By voltage-clamp protocols (Liu *et al.*, 2011), Kv currents were reduced in LV myocytes from old mice (31-32 months), with respect to cells obtained from animals at 3-4 months of age (**Figure 17**). Thus, reduction of Kv currents in old myocytes contributes, at least in part, to the prolonged repolarization of the AP.

Next, we tested whether changes in the slowly inactivating late Na^+ (I_{NaL}) and L-type Ca^{2+} (I_{CaL}) inward currents were implicated in the protracted AP. I_{NaL} current density was 1.6-fold higher in 30 month-old cardiomyocytes than in 3 month-old cells (**Figure 18**). Additionally, I_{NaL} maximal conductance was increased, whereas voltage-activation and steady state inactivation were comparable in young and old cells (**Figure 19**). Moreover, we dissected pharmacologically I_{NaL} in young and old myocyte using tetrodotoxin (TTX) and found that the TTX-sensitive slowly inactivating current was increased in cells from old mice, with respect to young (**Figure 20**). The fast inactivating Na^+ current (I_{Na}), that controls the upstroke of the AP, was not altered with aging (**Figure 21**), a result which is consistent with the preservation of the amplitude and upstroke velocity of the AP. Similarly, the density and properties of I_{CaL} were comparable in the two groups of cells (**Figure 22**).

The role of I_{NaL} in myocyte repolarization was determined by measuring the AP before and after inhibition of this current. We employed ranolazine, a selective inhibitor of I_{NaL} (Sossalla *et al.*, 2008; Wagner *et al.*, 2011; Moreno & Clancy, 2012), and mexiletine, a blocker of the late Na^+ current that, as previously reported (Sicouri *et al.*, 1997; Gao *et al.*, 2013), minimally affects peak I_{Na} (**Figure 23**). Reduction of I_{NaL} shortened the intermediate and late repolarization phases of the AP in old myocytes, but had attenuated impact on young cells (**Figure 24**). Moreover, the duration of LV MAP measured at 90% repolarization was reduced following mexiletine perfusion by 14% and 22% in 5-month and of 24-30 month-old

hearts, respectively (**Figure 25**), indicating that inhibition of I_{NaL} abbreviates the repolarization phase of the AP with aging.

To establish whether I_{NaL} was implicated in the prolongation of the QT interval in the senescent heart (see **Figure 12b**), young and old mice were treated systemically with an inhibitor of I_{NaL} or saline and electrocardiograms were obtained before and one hour after administration of the inocula. In young animals, inhibition of I_{NaL} had no major consequences on the electrical activation and recovery of the myocardium. Conversely, blockade of I_{NaL} in old mice with ranolazine or mexiletine shortened the QT interval by 7% and 8%, respectively (**Figure 26**). These results were confirmed in conscious mice by telemetry (**Figure 27**). Thus, alterations in I_{NaL} prolong myocyte AP and electrical recovery of the senescent myocardium, and inhibition of I_{NaL} partially corrects this defect, restoring in vivo a younger cardiac phenotype.

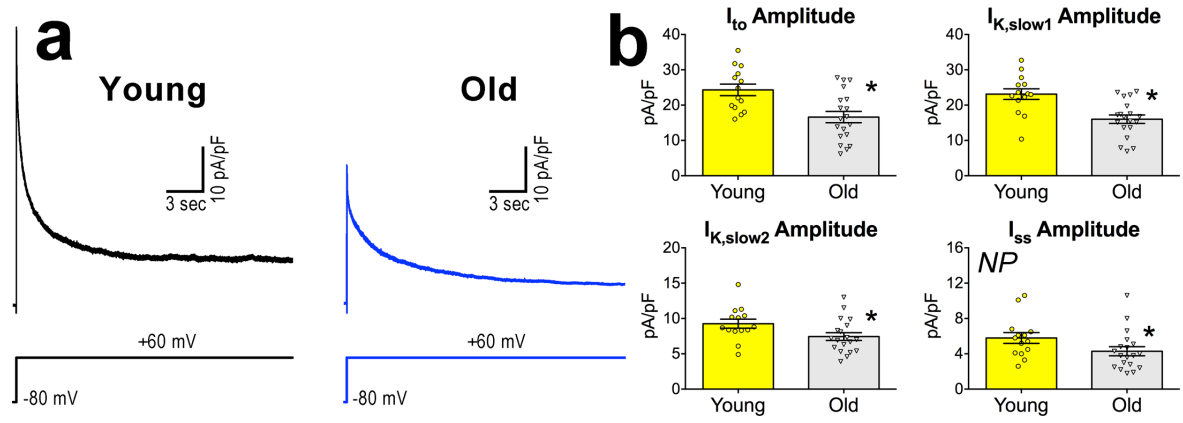

Figure 17. Aging alters Kv currents in LV cardiomyocytes. (**a**) Whole-cell voltage-gated K^+ currents recorded in voltage-clamp in a young (black traces) and an old (blue traces) LV myocyte. Voltage-clamp protocol is reported in the lower traces. (**b**) Quantitative data for the amplitude Kv current components in myocytes from mice at 3-4 months (Young, *n* = 14 cells from 5 hearts) and 31-32 months (Old, *n* = 19 cells from 4 hearts) are shown as mean ± s.e.m. **P*<0.05 versus old (Student's *t*-test and Mann-Whitney rank sum test); *NP*: non-parametric analysis.

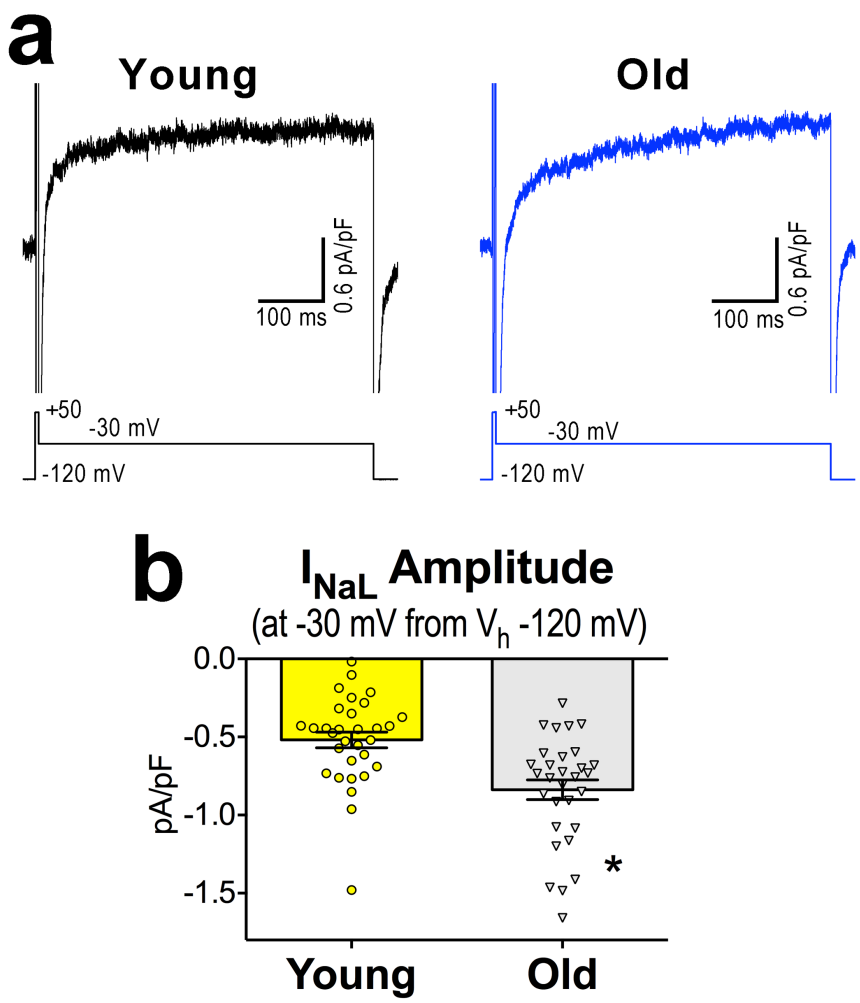

Figure 18. Aging alters I_{NaL} in LV cardiomyocytes. (**a**) Whole-cell voltage-gated Na^+ currents recorded in voltage-clamp in a young (black traces) and an old (blue traces) LV myocyte. The voltage-command protocol, which is shown in the lower traces, comprised a preconditioning pulse to +50 mV to prevent Na^+ influx and minimize loss of voltage control. Alternative voltage-clamp protocols were also employed (see Figs 19 and 20). (**b**) Quantitative data in myocytes from male mice at 3 months (Young, *n* = 31 cells from 4 hearts) and 30 months (Old, *n* = 30 cells from 4 hearts) are shown as mean ± s.e.m. and scatter plots. **P*<0.001 versus Young (Mann-Whitney rank sum test).

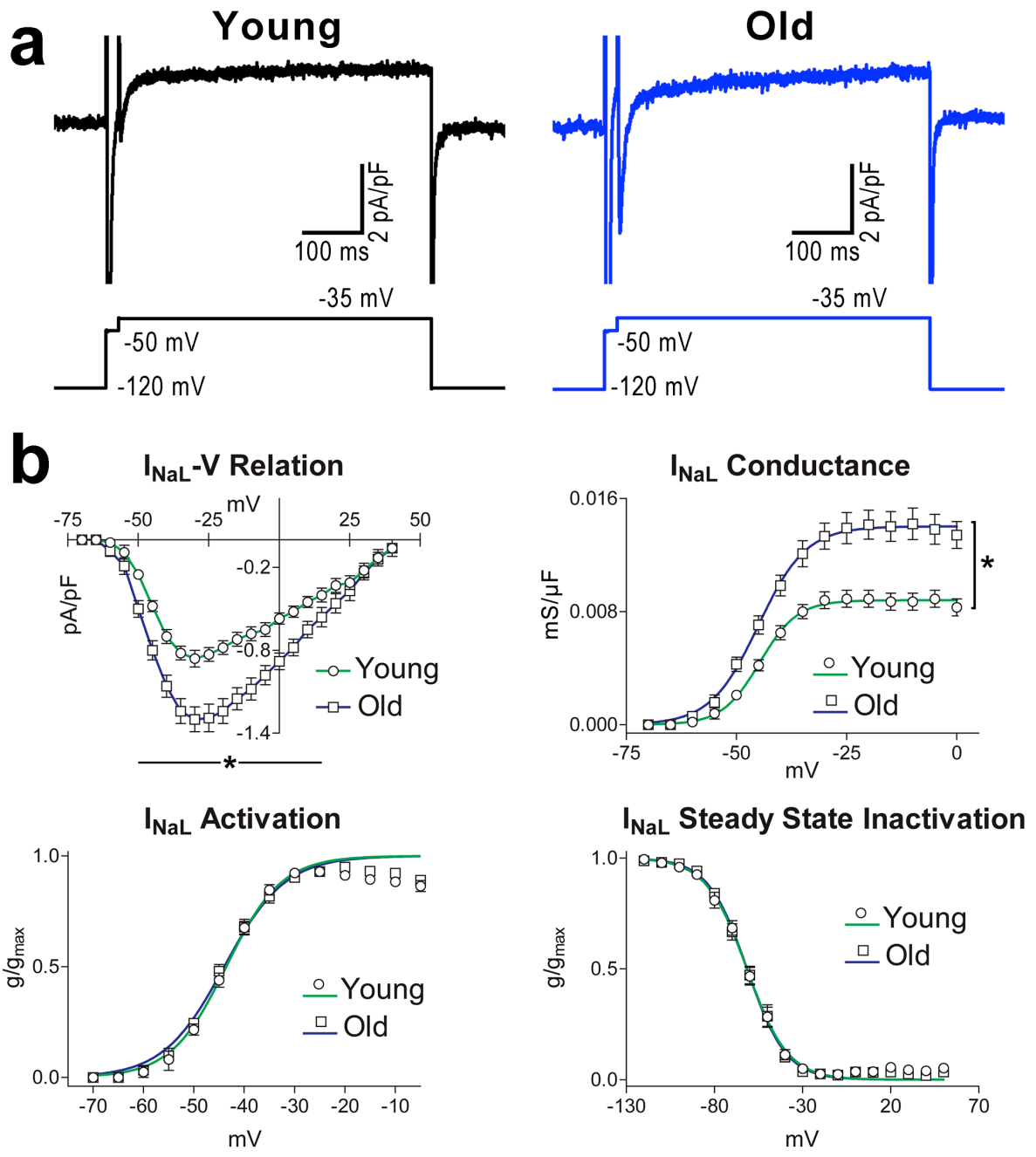

Figure 19. The late Na^+ current I_{NaL} is enhanced in old myocytes. (**a**) Whole-cell voltage-gated Na^+ currents in a young (black traces) and an old (blue traces) LV myocyte. The voltage-command protocol is shown in the lower traces. (**b**) Quantitative data for I_{NaL} properties obtained in myocytes from male mice at 3 months (Young, *n* = 16-27 cells from 5 hearts) and 30-31 months (Old, *n* = 9-18 cells from 5 hearts) shown as mean ± s.e.m. **P*<0.05 versus Young in I_{NaL}-V Relation (Student's *t*-test and Mann-Whitney rank sum test). Conductance, activation, and inactivation plots were fitted with Boltzmann functions (Young, solid green line; Old, solid blue line). **P*<0.0001 between fittings (Student's *t*-test). Parameters are reported in Table 3.

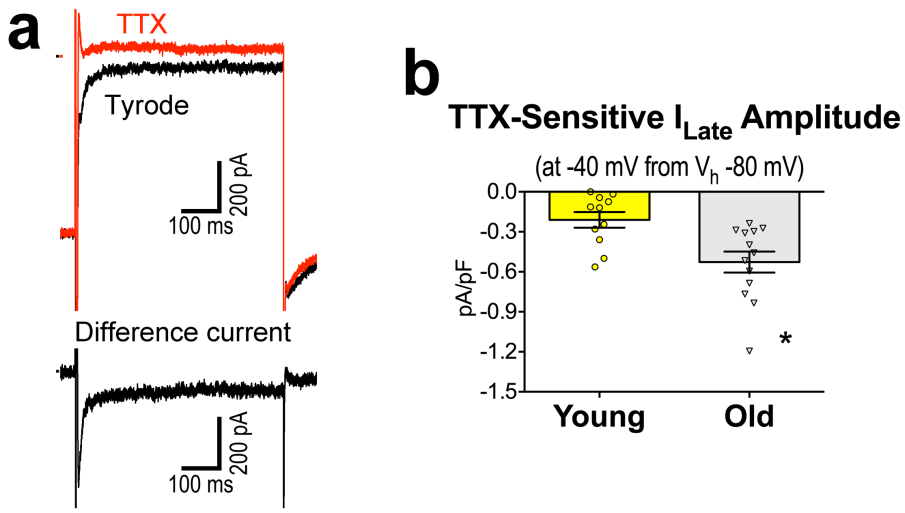

Figure 20. A slowly inactivating TTX-sensitive current is enhanced in old myocytes. (**a**) Whole-cell voltage-gated currents recorded in voltage-clamp in an old myocyte with a depolarizing step from -80 mV to -40 mV before (Tyrode, black traces) and after exposure to 10 µM tetrodotoxin (TTX, red traces). Difference current is reported in the lower panel. (**b**) Quantitative data of the time dependent component of the TTX-sensitive difference current obtained in myocytes from male mice at 3-6 months (Young, *n* = 11 cells from 9 hearts) and 31-35 months (Old, *n* = 13 cells from 7 hearts) are shown as mean ± s.e.m. and scatter plots. **P*<0.01 versus Young (Mann-Whitney rank sum test). With the protocol employed, peak I_{Na} was reduced following TTX exposure. Due to specific amplifier gain settings, I_{Na} was saturated in Tyorde solution, but its amplitude was not saturated and comparable between the two cell populations in TTX (74 ± 9 pA/pF in young and 64 ± 9 pA/pF in old myocytes).

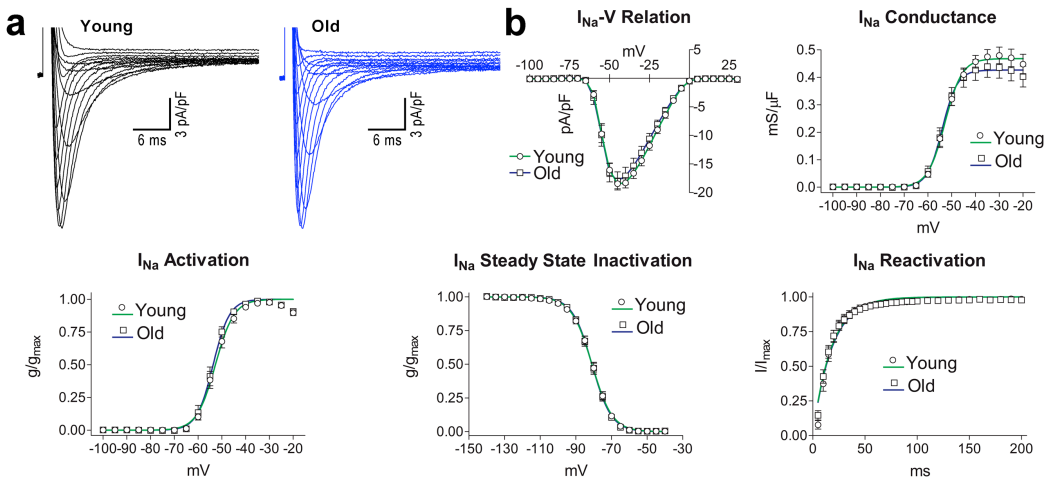

Figure 21. The fast Na^+ current I_{Na} is not affected by aging. (**a**) Whole-cell voltage-gated Na^+ currents recorded in voltage-clamp in a young (black traces) and an old (blue traces) LV myocyte. (**b**) I-V relations, voltage-dependency of conductance, steady state activation, and steady state inactivation, time dependency of reactivation for I_{Na} in myocytes from male mice at 3 months (Young, *n* = 17-26 cells from 4 hearts) and 29-31 months (Old, *n* = 16-19 cells from 4 hearts) are shown as mean ± s.e.m. Conductance, activation, and inactivation plots were fitted with Boltzmann functions, and reactivation plots with an exponential function (Young, solid green line; Old, solid blue line). Parameters are reported in Table 3.

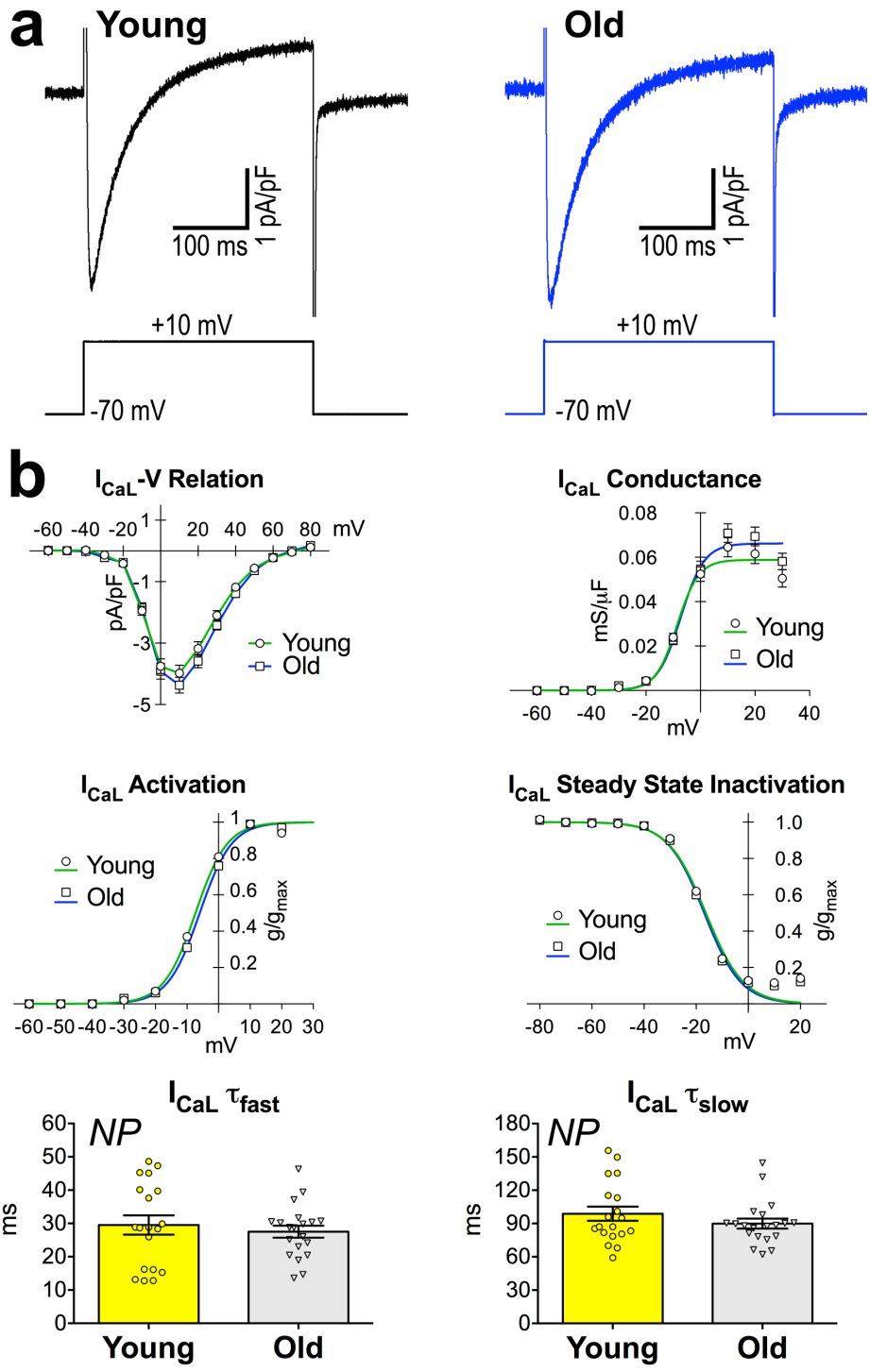

Figure 22. The L-type Ca^{2+} current I_{CaL} is not affected by aging. (**a**) Whole-cell voltage-gated Ca^{2+} currents recorded in voltage-clamp in a young (black traces) and an old (blue traces) LV myocyte. (**b**) L-type Ca^{2+} current properties obtained in myocytes from male mice at 3 months (Young, *n* = 19 cells from 5 hearts) and 27 months (Old, *n* = 17-20 cells from 5 hearts). I-V relations, voltage-dependency of conductance, steady state activation, and steady state inactivation for I_{CaL} are shown as mean ± s.e.m. Fast and slow time constants (τ) for I_{CaL} were measured at 0 mV and are shown as mean ± s.e.m. and scatter plots. Conductance, activation, and inactivation plots were fitted with Boltzmann functions (Young, solid green line; Old, solid blue line). Parameters are reported in Table 3. *NP*: non-parametric analysis.

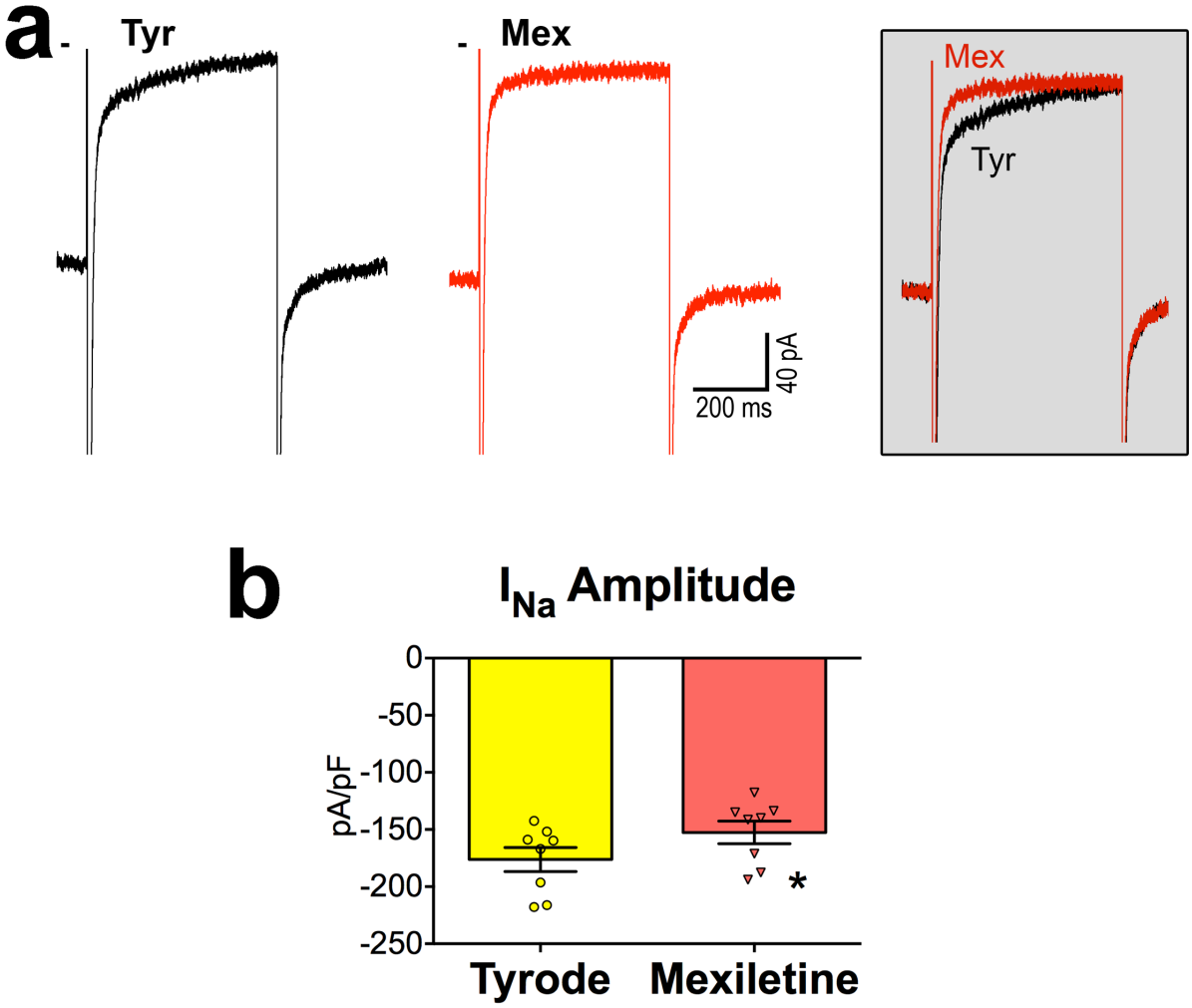

Figure 23. Mexiletine inhibits I_{NaL}. (**a**) Current traces in voltage-clamp mode showing the effects of mexiletine on I_{NaL} in a myocytes obtained from a male mouse at 27 month of age. I_{NaL} was elicited by a depolarizing step from V_h -90 mV to -30 mV. Traces recorded before (black trace) and in the presence of 30 µM mexiletine (Mex, red trace) are superimposed in the inset. (**b**) Quantitative data for peak I_{Na} density elicited by depolarizing pulses to -40 mV from V_h -70 in myocytes from male mice at 5-6 months (*n* = 6 cells from 3 hearts) before (Tyrode) and after exposure to the 10 µM mexiletine are shown as mean ± s.e.m. and scatter plots. **P*<0.01 versus Tyrode (Wilcoxon signed rank test);

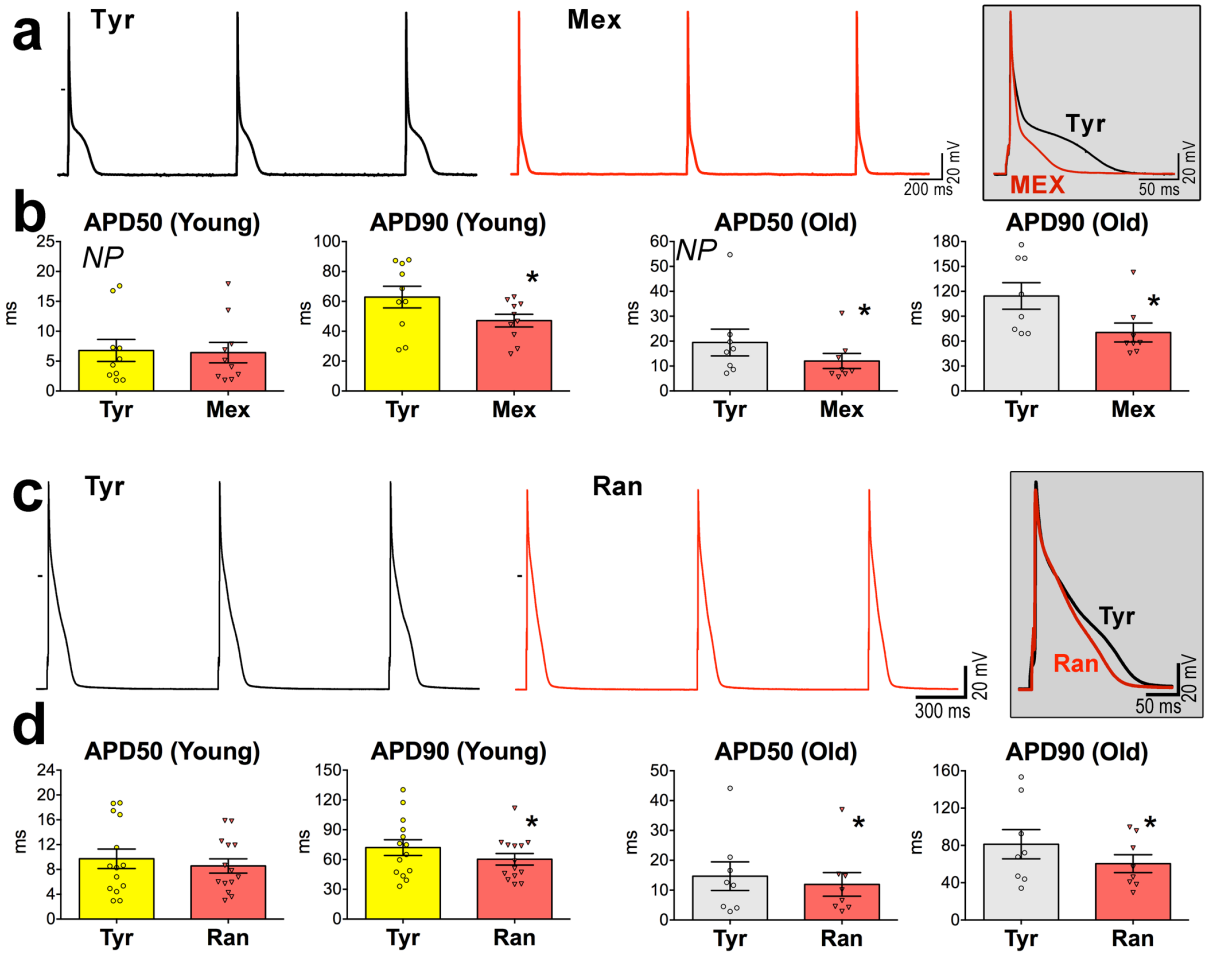

Figure 24. Inhibition of I_{NaL} shortens the AP. (**a**) APs recorded in an old myocyte before (Tyrode, black traces) and after exposure to the Na^+ channel inhibitor mexiletine (Mex, red traces). Superimposed traces are reported in the inset. (**b**) Quantitative data in myocytes from male mice at 3 months (Young, *n* = 10 cells from 5 hearts) and 27-30 months (Old, *n* = 8 cells from 5 hearts) before (Tyr) and after exposure to 10 μM mexiletine (Mex) are shown as mean ± s.e.m. and scatter plots. Tyr: Tyrode solution. **P*<0.05 versus Tyr (paired *t*-test and Wilcoxon signed rank test); *NP*: non-parametric analysis. (**c**) APs recorded in an old myocyte before (Tyrode, black traces) and after exposure to I_{NaL} inhibitor ranolazine (Ran, red traces). Superimposed traces are reported in the inset. (**d**) Quantitative data in myocytes from mice at 3-6 months (Young, *n* = 14 cells from 4 hearts) and 27-33 months (Old, *n* = 8 cells from 5 hearts) before (Tyr) and after exposure to 10 μM ranolazine (Ran) are shown as mean ± s.e.m. and scatter plots. **P*<0.05 versus Tyr (paired *t*-test).

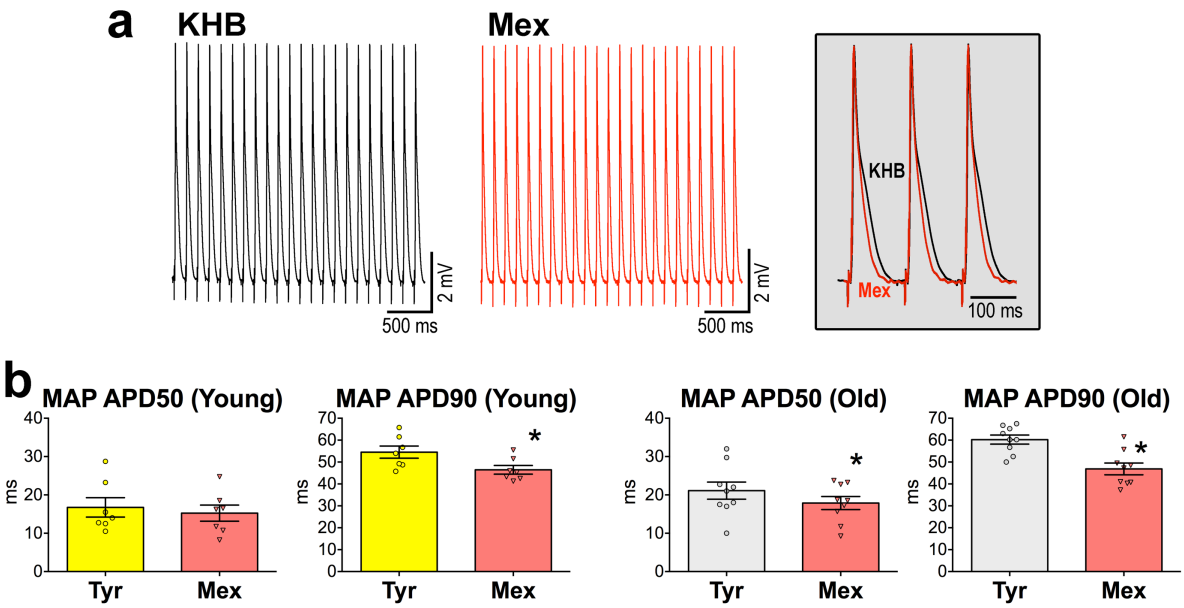

Figure 25. Inhibition of I_{NaL} shortens local epicardial monophasic APs. (**a**) Monophasic AP recorded before (KHB, black traces) and after perfusion of 10 µM mexiletine (Mex, red traces) in an old mouse heart. (**b**) Quantitative data of repolarization times for hearts from female mice at 5 months (Young, *n* = 7) and male mice at 24-30 months (*n* = 9) before (KHB, Krebs–Henseleit buffer) and after exposure to the I_{NaL} inhibitor mexiletine (Mex) are shown as mean ± s.e.m. and scatter plots. **P*<0.05 versus KHB (paired *t*-test).

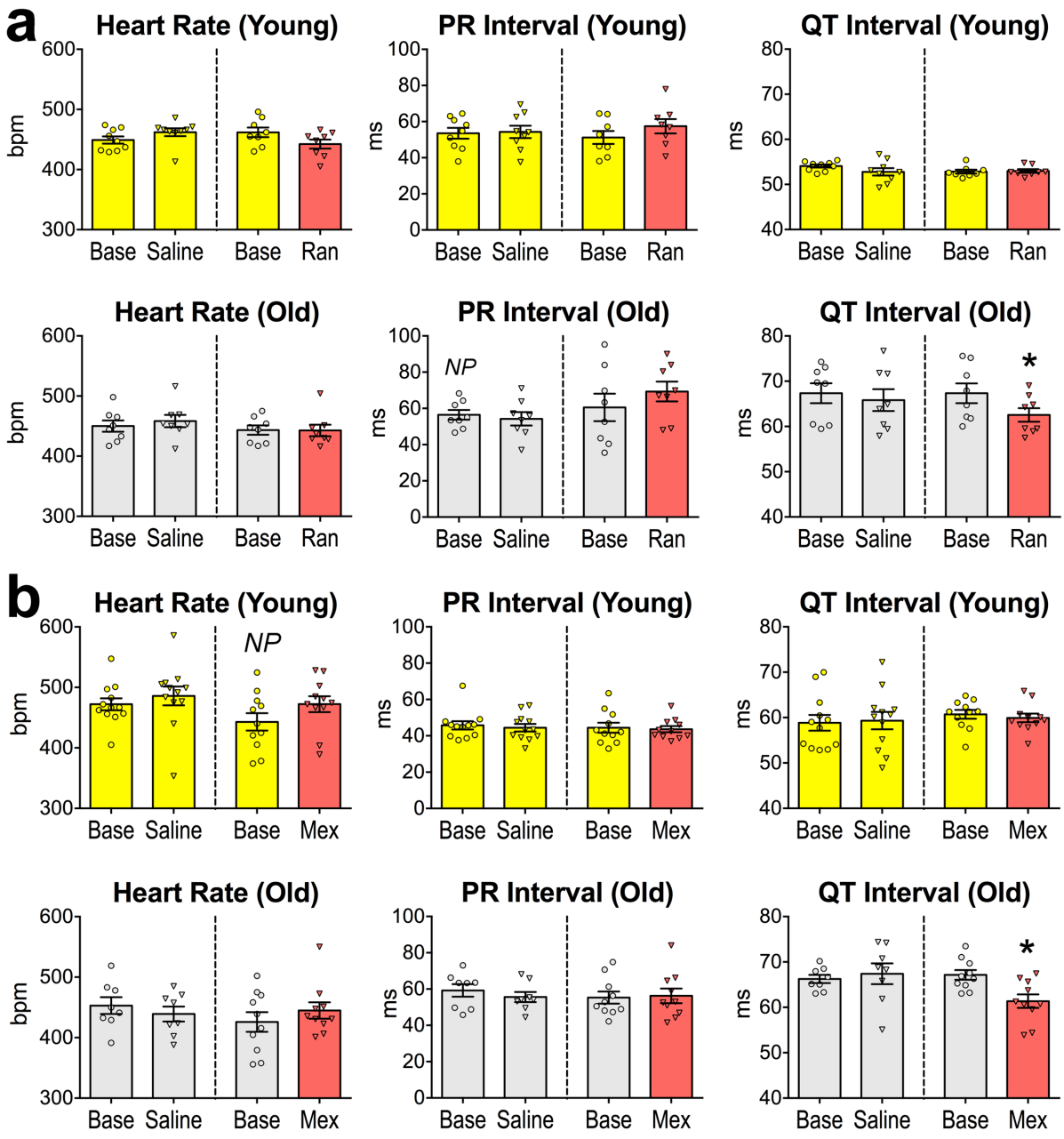

Figure 26. Inhibition of I_{NaL} shortens the repolarization of the old heart. (**a**) Quantitative data for electrocardiographic parameters obtained in male mice at 3-4 months (Young) and at 30-31 months (Old) at baseline (Base) and 1 hour after treatment with saline (Young, *n* = 9; Old *n* = 8) or ranolazine (30 mg kg^{-1} body weight, i.p.) (Young, *n* = 8; Old *n* = 8). Data are shown as mean ± s.e.m and scatter plots. **P*<0.05 versus Base (paired *t*-test and Wilcoxon signed rank test); *NP*: non-parametric analysis. (**b**) Quantitative data for electrocardiographic parameters obtained in male mice at 3 months (Young) and at 30 months (Old) at baseline (Base) and 1 hour after treatment with saline (Young, *n* = 12; Old *n* = 8) or mexiletine (5 mg kg^{-1} body weight, i.p.) (Young, *n* = 11; Old *n* = 10). Data are shown as mean ± s.e.m and scatter plots. **P*<0.05 versus Base (paired *t*-test and Wilcoxon signed rank test); *NP*: non-parametric analysis.

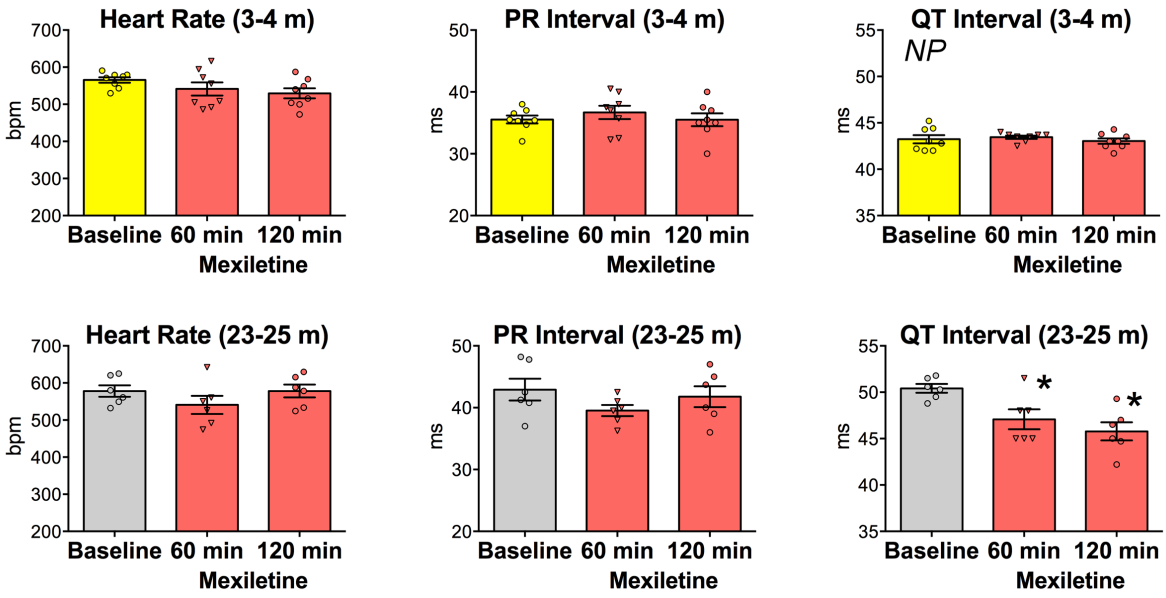

Figure 27. Inhibition of I_{NaL} shortens the electrical recovery of the old heart. Quantitative data for electrocardiographic parameters obtained in conscious male mice at 3-4 months (3-4 m, *n* = 8) and 23-25 months (23-25 m, *n* = 6) treated with mexiletine (5 mg kg^{-1} body weight) and followed for a two-hour period. Data are shown as mean ± s.e.m and scatter plots. **P*<0.05 versus baseline (before administration of the inhibitor, one-way ANOVA with Bonferroni's *post hoc* test); *NP*: non-parametric analysis.

Electrical activity and modulation of myocyte mechanics and Ca^{2+} transients

The repolarization of the AP controls the transmembrane Ca^{2+} influx via L-type channels and the NCX, which, in turn, activates the release of Ca^{2+} from the sarcoplasmic reticulum (SR)(Sah *et al.*, 2001; Bers, 2002; Janczewski *et al.*, 2002; Sah *et al.*, 2003; Rota *et al.*, 2007; Signore *et al.*, 2013). Thus, we tested whether the protracted electrical repolarization of the AP of senescent myocytes was associated with alterations in Ca^{2+} cycling and cell contractility. Ca^{2+} transients and unloaded cell shortening were evaluated in young, 3 months, and old, 29-30 months, myocytes. At 1 Hz, Ca^{2+} transient amplitude and cell shortening were similar in both groups of myocytes, but time to peak Ca^{2+} transient was delayed by 26%, and time to peak shortening was prolonged by 21% in senescent cells. Moreover, Ca^{2+} decay and myocyte relengthening at 90% were, respectively, 54% and 32% longer in old myocytes (**Figure 28**). The delay in the timing parameters was maintained at higher stimulation frequencies, although a reduction in developed Ca^{2+} was observed (**Figure 29**).

To establish the presence of a causative link between prolonged AP in old cardiomyocytes and delayed kinetics and preserved amplitude of Ca^{2+} transients, AP-clamp experiments

were performed. Two short APs (APD_{50}: 5 and 7 ms) collected from 2 young myocytes and 3 longer APs (APD_{50}: 17, 26, and 80 ms) obtained from 3 old cells were employed as voltage-clamp command while monitoring intracellular Ca^{2+} levels. As previously reported (Bouchard *et al.*, 1995; Rota *et al.*, 2007; Signore *et al.*, 2013), longer APD led to a progressive increase in Ca^{2+} transient amplitude, but the slope of the positive APD-inotropic relationship was attenuated in myocytes obtained from old mice, with respect to young (**Figure 30**). In both group of cells, increases in APD resulted in delayed time to peak and Ca^{2+} decay at 30%, whereas the late decay, measured at 90%, negatively correlated with APD. Moreover, when the same AP shape was imposed to young and old myocytes, the elicited Ca^{2+} transients presented comparable timing parameters, but amplitude tended to be reduced in old (**Figure 31**). These results suggest that i) prolongation of the AP increases the amplitude of Ca^{2+} transients in cardiomyocytes, but the efficiency of the process is attenuated in old cells; ii) longer APD delays time to peak and early decay of Ca^{2+} transients; and iii) experimental conditions employed here, including cell dialysis, abolish the slower Ca^{2+} transient kinetics observed in old cells with field stimulation.

The lack of potentiated Ca^{2+} transient amplitude in old myocytes in the presence of protracted APD, with respect to young cells, raised the possibility that SR Ca^{2+} load was affected with age, a factor that may limit Ca^{2+} release following electrical excitation in old cells (Trafford *et al.*, 2000). Thus, field stimulated myocytes were rapidly exposed to caffeine to assess SR Ca^{2+} content (Rota *et al.*, 2005; Rota *et al.*, 2007; Signore *et al.*, 2013). The amplitude of the AP-induced Ca^{2+} transient was comparable in young and old cells whereas the caffeine-induced Ca^{2+} release was reduced in old myocytes (**Figure 32a and 32b**), suggesting a defective SR Ca^{2+} load. Moreover, the decay of the caffeine-induced Ca^{2+} transient, which reflects NCX activity (Voigt *et al.*, 2012), was faster in old myocytes (**Figure 32c**). Thus, reduced SR Ca^{2+} load may represent the basis for the attenuated amplitude of Ca^{2+} transients in old myocytes in the presence of protracted APs.

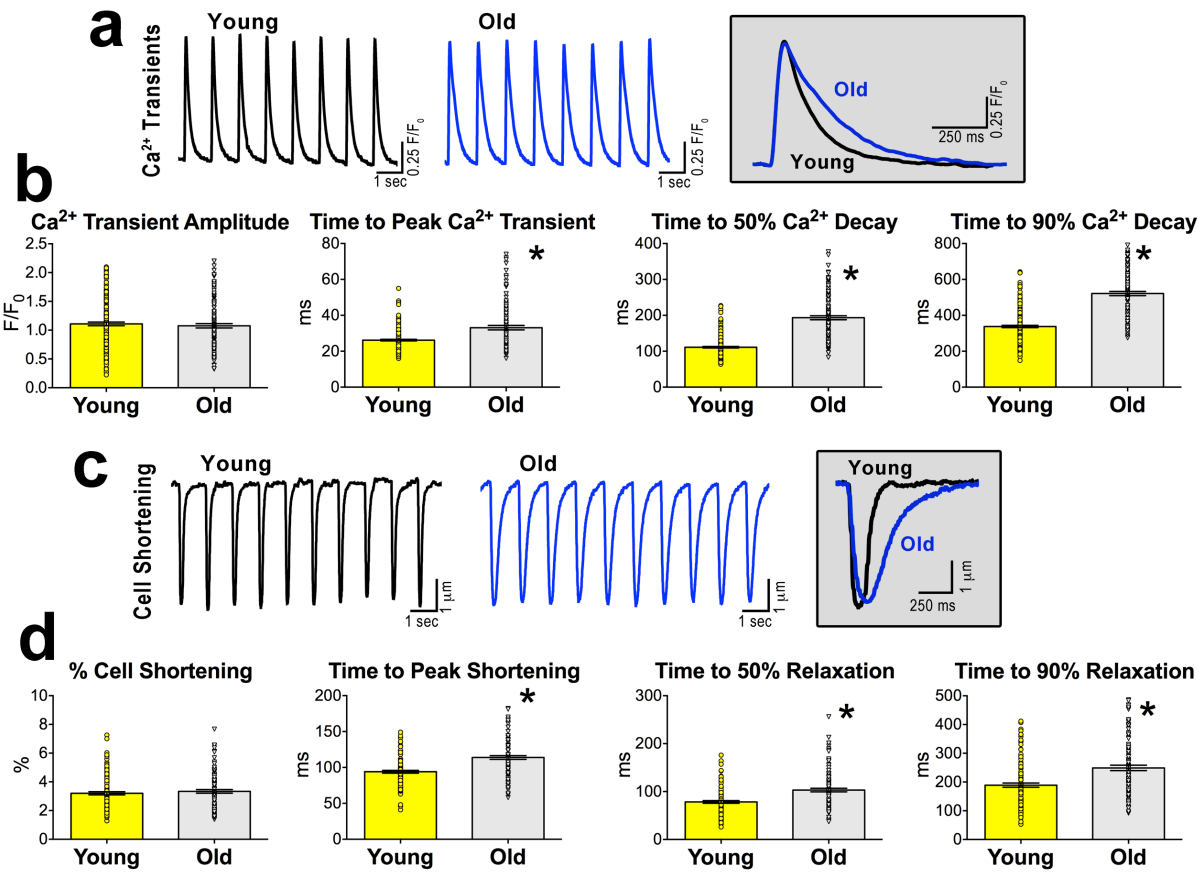

Figure 28. Electromechanical properties of aging LV myocytes. (**a**) Ca^{2+} transients of young (black traces) and old (blue traces) myocytes. Superimposed traces are reported in the inset. (**b**) Quantitative data for Ca^{2+} transient properties obtained in myocytes from mice at 3 months (Young) and 29-30 months (Old) (Young, *n* = 195 cells from 16 hearts; Old, *n* = 131 cells from 11 hearts); data are shown as mean ± s.e.m. and scatter plots. **P*<0.05 versus Young (Mann-Whitney rank sum test). (**c**) Unloaded cell shortening of young (black traces) and old (blue traces) myocytes. Superimposed traces are reported in the inset. (**d**) Quantitative data for cell shortening properties obtained in myocytes from mice at 3 months (Young) and 29-30 months (Old) (Young, *n* = 129 cells from 8 hearts; Old, *n* = 117 cells from 7 hearts); data are shown as mean ± s.e.m. and scatter plots. **P*<0.05 versus Young (Mann-Whitney rank sum test).

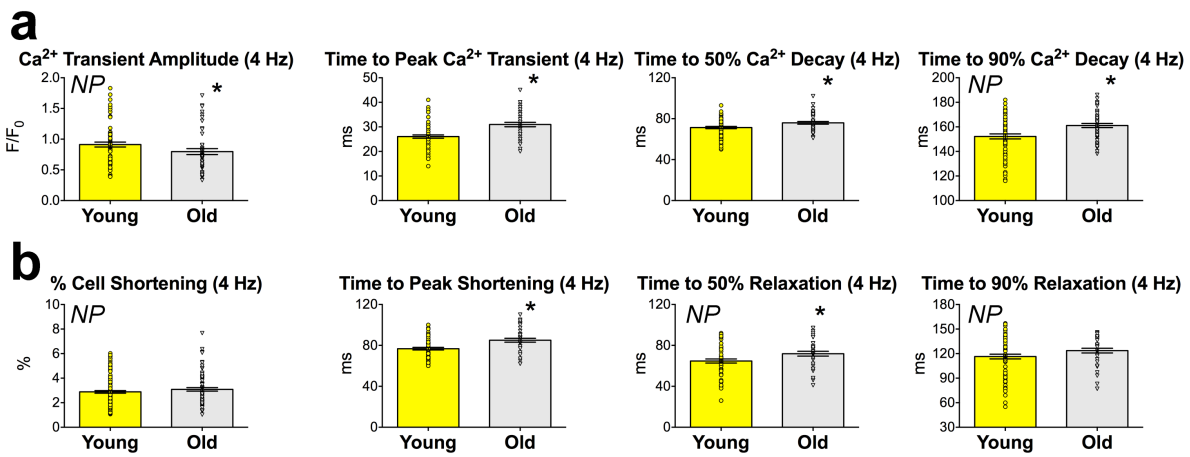

Figure 29. Aging delays the kinetics of Ca^{2+} transients and cell shortening in LV myocytes. (**a**) Ca^{2+} transient properties assessed at 4 Hz pacing rate in myocytes from male mice at 3-6 months (Young, *n* = 69 cells from 4 hearts) and 30-35 months (Old, *n* = 49 cells from 4 hearts) are shown as mean ± s.e.m and scatter plots. **P*<0.05 versus Young (Student's *t*-test and Mann-Whitney rank sum test); *NP*: non-parametric analysis. (**b**) Quantitative data for cell shortening properties obtained in myocytes from mice at 3 months (Young, *n* = 69 cells from 7 hearts) and 29-30 months (Old, *n* = 41 cells from 6 hearts) stimulated at 4 Hz pacing rate; data are shown as mean ± s.e.m and scatter plots. **P*<0.05 versus Young (Student's *t*-test and Mann-Whitney rank sum test); *NP*: non-parametric analysis.

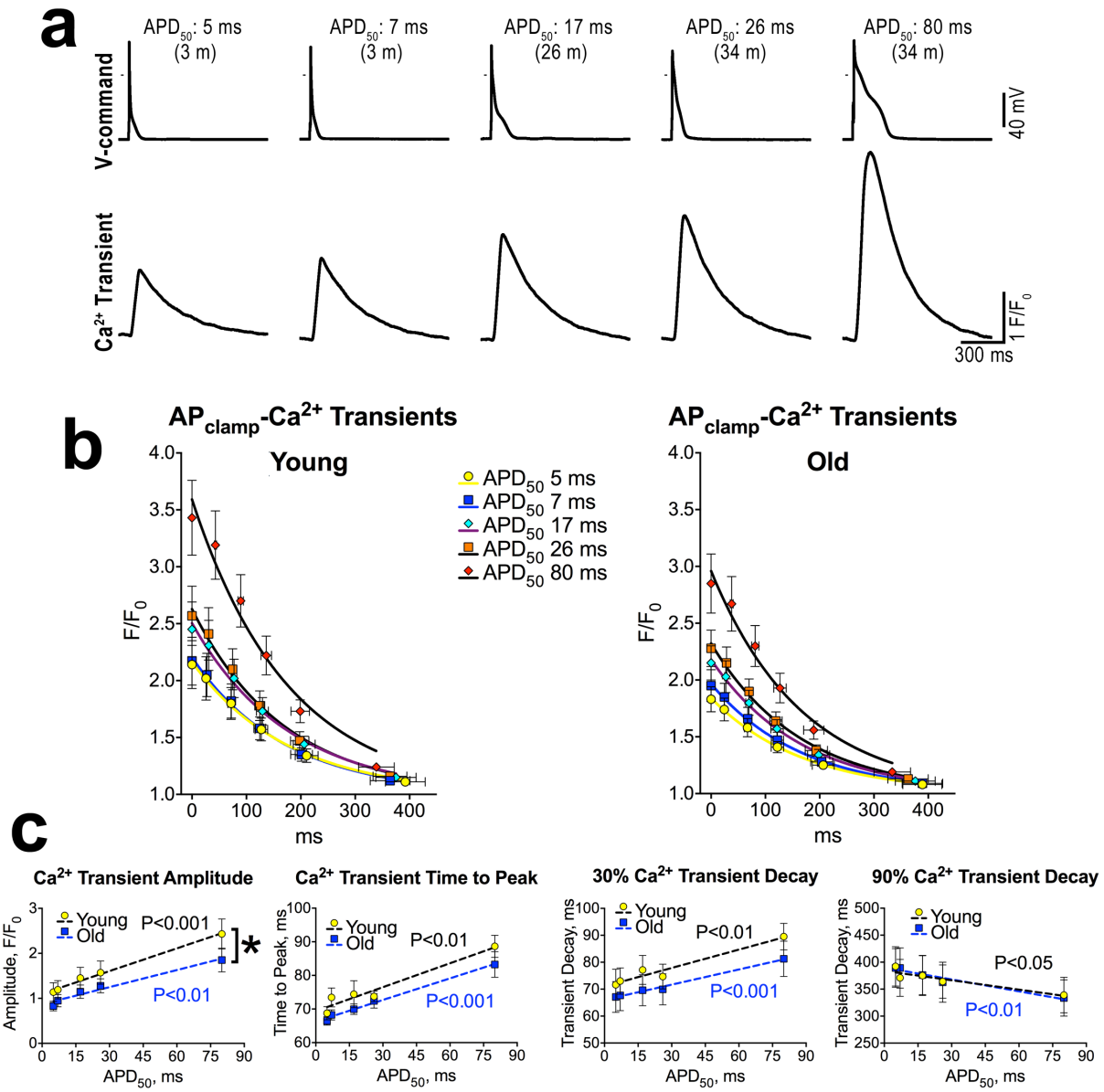

Figure 30. AP and Ca^{2+} transients in aging LV myocytes. (**a**) AP profiles (upper traces) obtained from myocytes at different age (m, months) were applied as voltage-clamp command (AP-clamp) in an old myocyte to elicit Ca^{2+} transients (lower traces). Ionic currents recorded are omitted. (**b**) Decay of Ca^{2+} transients elicited by 5 different AP-clamp protocols obtained in myocytes from male mice at 3-5 months (Young) and 28-33 months (Old) are shown as mean ± s.e.m. (Young, *n* = 12 cells from 5 hearts; Old, *n* = 9 cells from 2 hearts). Levels of the Ca^{2+} fluorescence signal from the peak of the Ca^{2+} transient to 90% of the decay are reported. Data were fitted with monoexponential functions (solid lines). Fitting parameters are reported in Table 3. (**c**) Bivariate plot for APD50 of the AP used as V_{clamp} command and Ca^{2+} transient properties obtained from young and old myocytes reported in **b**.

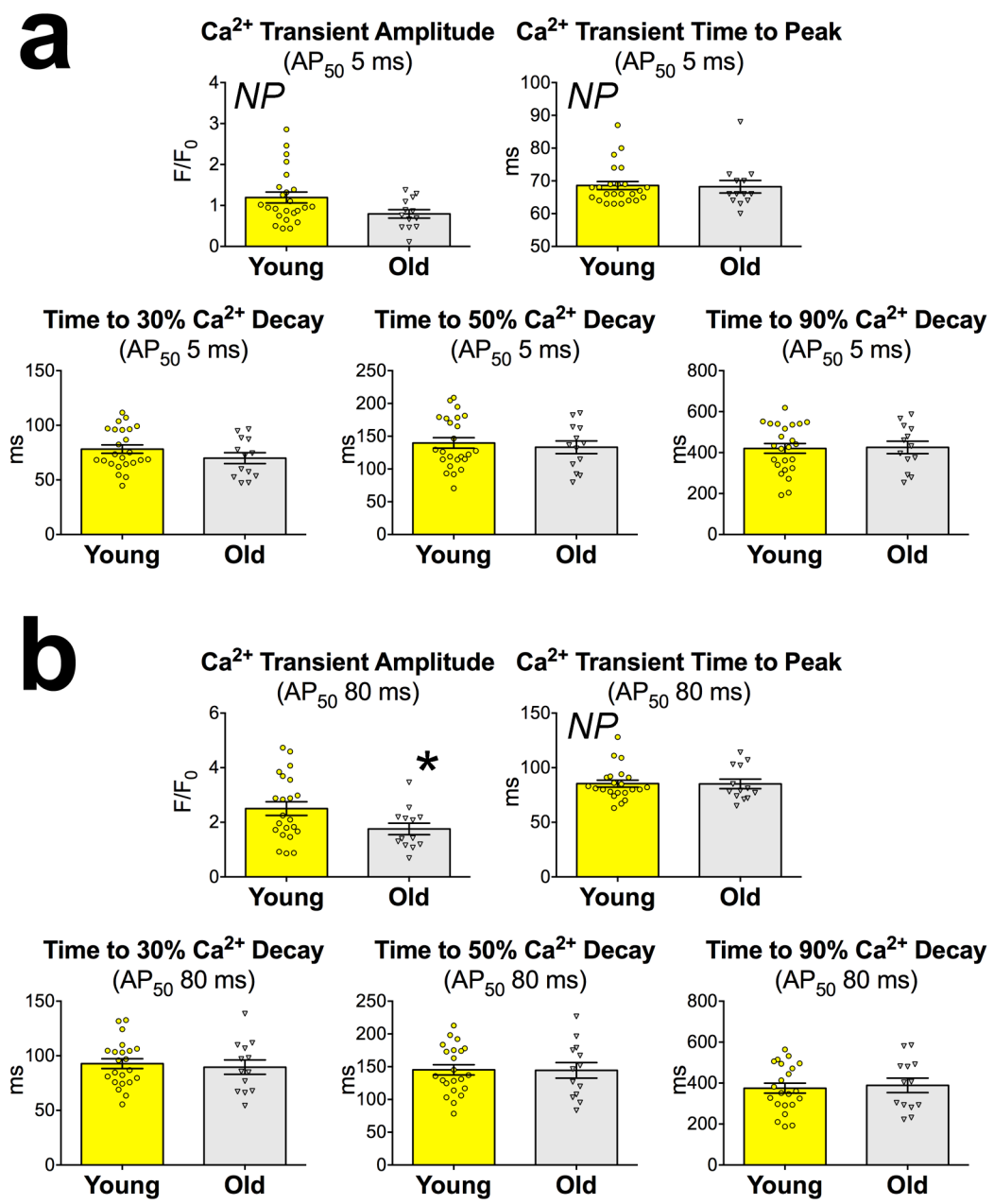

Figure 31. AP duration and Ca^{2+} transients in aging myocytes. (**a**,**b**) Quantitative properties of Ca^{2+} transients elicited in young and old myocytes by AP-clamp protocols with short (**a**) and long (**b**) AP shape. Data for myocytes from male mice at 3-5 months (Young) and 28-33 months (Old) are shown as mean ± s.e.m. (**a**) Young, *n* = 24 cells from 5 hearts; Old, *n* = 13 cells from 2 hearts; (**b**) Young, *n* = 22 cells from 5 hearts; Old, *n* = 13 cells from 2 hearts. **P*<0.05 versus Young (Student's t-test and Mann-Whitney rank sum test); *NP*: non-parametric analysis. For Ca^{2+} Transient Amplitude in **b**, **P* = 0.049.

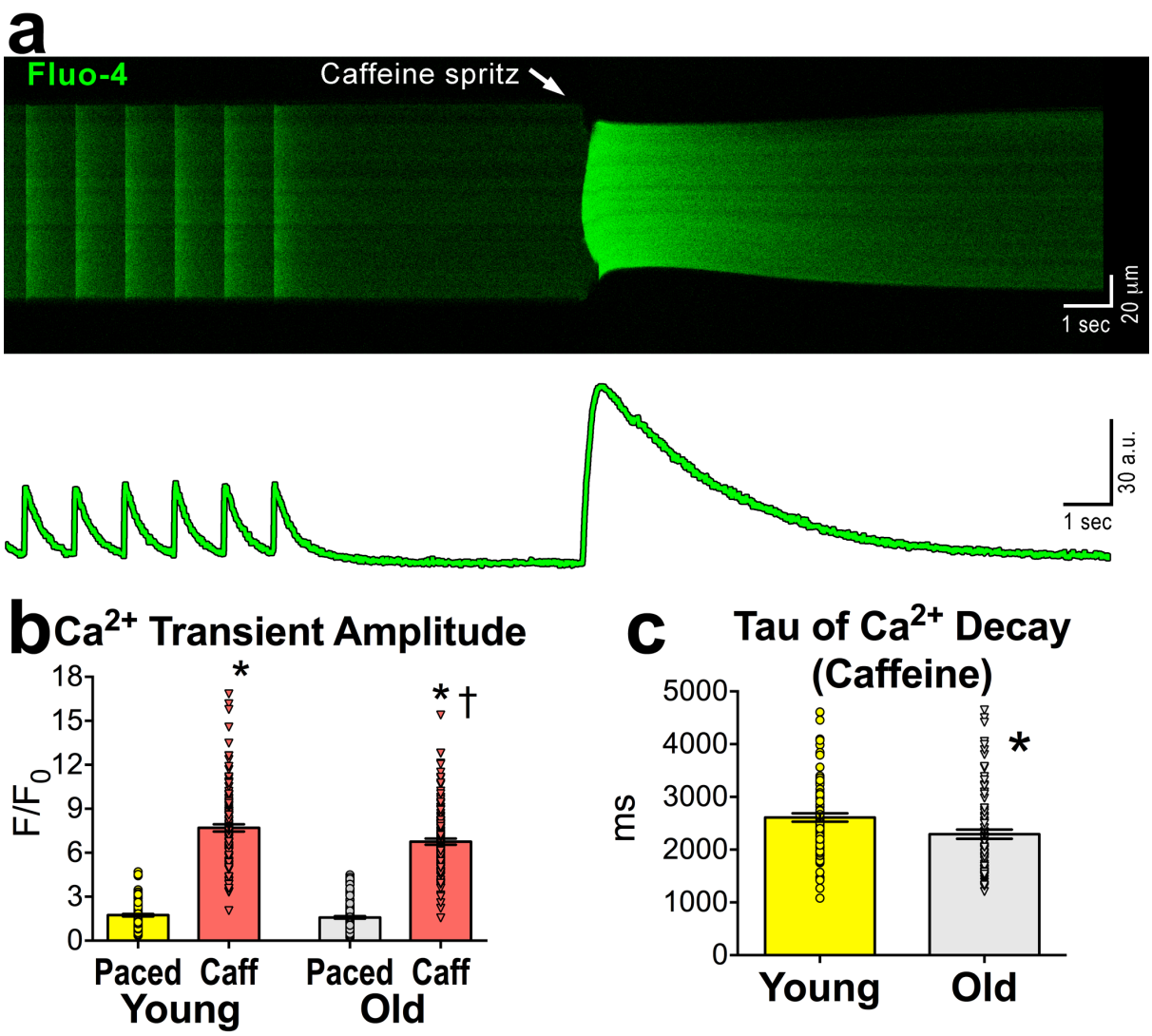

Figure 32. SR Ca^{2+} load of aging LV myocytes. (**a**) Line scan image of a young myocyte loaded with the Ca^{2+} indicator Fluo-4 (green). Ca^{2+} transients were elicited by electrical pacing or by 20 mM caffeine spritz (arrow). Scale bars, 1 s, 20 µm. Traces are reported in the lower panel. Scale bars, 1 s, 30 a.u. (**b**) Quantitative data for myocytes from male mice at 3-6 months (Young, *n* = 120 cells from 4 hearts) and 27 months (Old, *n* = 131 cells from 5 hearts) are shown as mean ± s.e.m. and scatter plots. Caff: caffeine. **P*<0.001 versus Paced (Wilcoxon Signed Rank Test); †*P*<0.01 versus Young (Mann-Whitney rank sum Test). (**c**) Quantitative data for the caffeine-induced Ca^{2+} transient decay obtained from a subset of cells represented in **b** (Young, *n* = 90 cells from 4 hearts; Old, *n* = 86 cells from 5 hearts) are shown as mean ± s.e.m. and scatter plots. **P*<0.05 versus Tyr (Mann-Whitney rank sum test).

I_{NaL} and modulation of myocyte mechanics and Ca^{2+} transients

The prolonged APD has only explained in part the defective properties of Ca^{2+} transients in old myocytes. Thus, additional factors potentially contributing to the altered Ca^{2+} transient decay were considered. Beside the contribution to the prolongation of the AP, enhanced Na^+ influx via I_{NaL} may increase intracellular Na^+ load in old cardiomyocytes (Maltsev *et al.*, 2007; Undrovinas *et al.*, 2010; Coppini *et al.*, 2013; Zaza & Rocchetti, 2013), a condition that inhibits diastolic Ca^{2+} extrusion via NCX and may affect Ca^{2+} transient decay (Vassalle & Lin, 2004; Sossalla *et al.*, 2008; Zaza *et al.*, 2008; Zaza & Rocchetti, 2013). To test this possibility, I_{NaL} was inhibited in field-stimulated myocytes obtained from young and old mice while monitoring Ca^{2+} transients and cell shortening. As expected, this intervention decreased amplitude and time to peak of Ca^{2+} transients and contractility, effects consistent with shortening of the APD. However, kinetics of Ca^{2+} decay and cell relengthening were reduced in old myocytes, opposing the behavior observed with AP-clamp tests (**Figure 33 and Figure 34**). To clarify these findings, 4-aminopyridine (4-AP) or anemonia toxin-II (ATX-II) were employed to prolong the APD (**Figure 35**) by selectively inhibiting Kv currents (Brouillette *et al.*, 2004; Rota *et al.*, 2007; Liu *et al.*, 2011) or enhancing I_{NaL} (Sicouri *et al.*, 1997; Fischer *et al.*, 2015), respectively. Prolongation of the AP with these two compounds increased the amplitude and delayed time to peak of Ca^{2+} transients. However, 4-AP led to a faster Ca^{2+} transient decay, whereas enhanced I_{NaL} with ATX-II failed to shorten the kinetics of Ca^{2+} decline (**Figure 36**). Thus, these findings suggest that enhanced Na^+ influx opposes the appearance of faster Ca^{2+} decay typically associated with increases in APD.

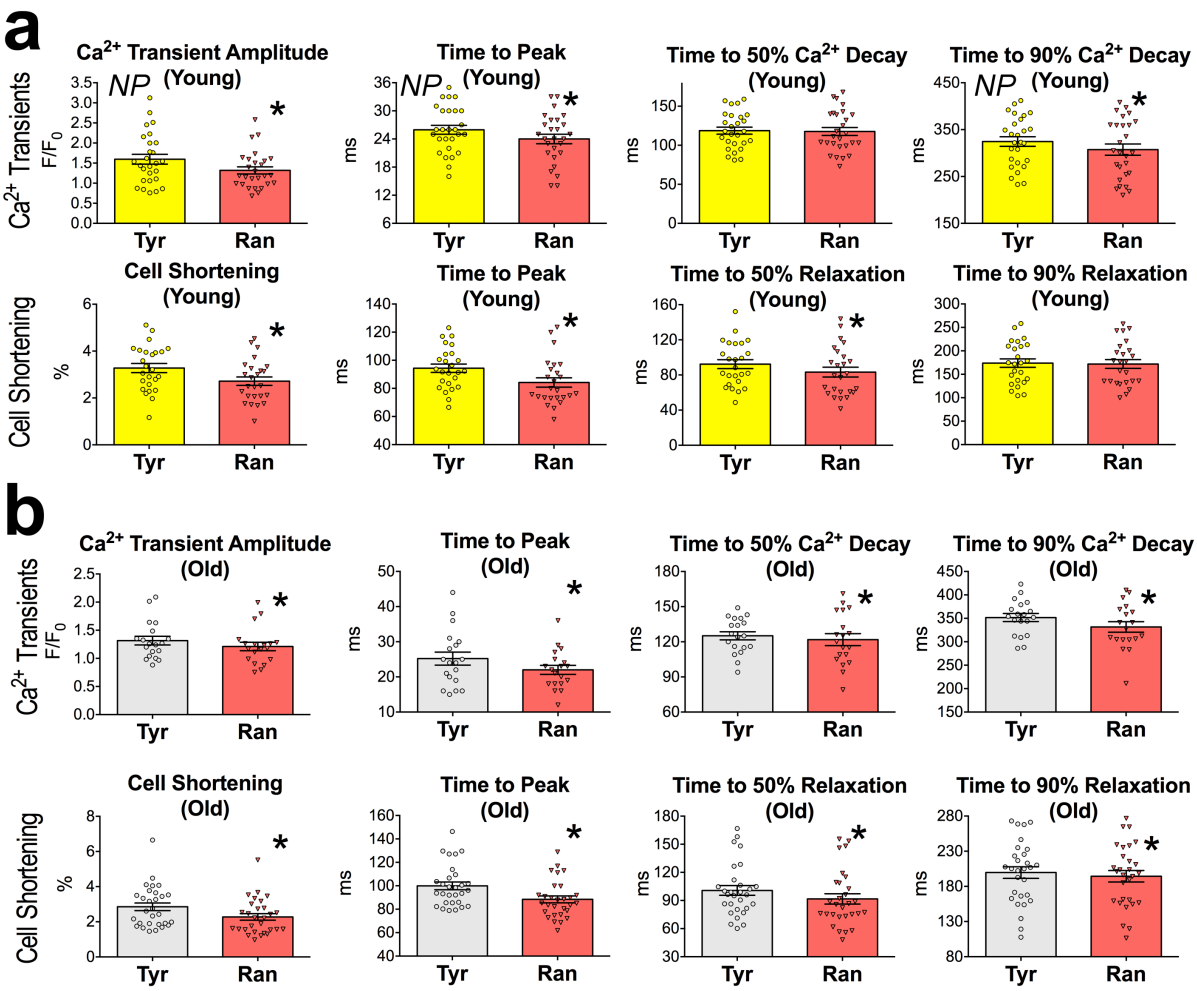

Figure 33. I_{NaL} alters the amplitude and kinetics of Ca^{2+} transients and contraction of LV myocytes. (**a**) Quantitative data for Ca^{2+} transient and cell shortening properties in myocytes from male mice at 3 months, before (Tyr) and after exposure to 10 μM ranolazine (Ran) (Ca^{2+} transients: *n* = 27 cells from 10 hearts; cell shortening *n* = 26 cells from 5 hearts); data are shown as mean ± s.e.m. and scatter plots. **P*<0.05 versus Tyr (paired *t*-test and Wilcoxon signed rank test); *NP*: non-parametric analysis. (**b**) Quantitative data for Ca^{2+} transient and cell shortening properties in myocytes from male mice at 30-33 months, before (Tyr) and after exposure to 10 μM ranolazine (Ran) (Ca^{2+} transients *n* = 19 cells from 5 hearts; cell shortening *n* = 29 cells from 4 hearts) data are shown as mean ± s.e.m. and scatter plots. **P*<0.05 versus Tyr (paired *t*-test).

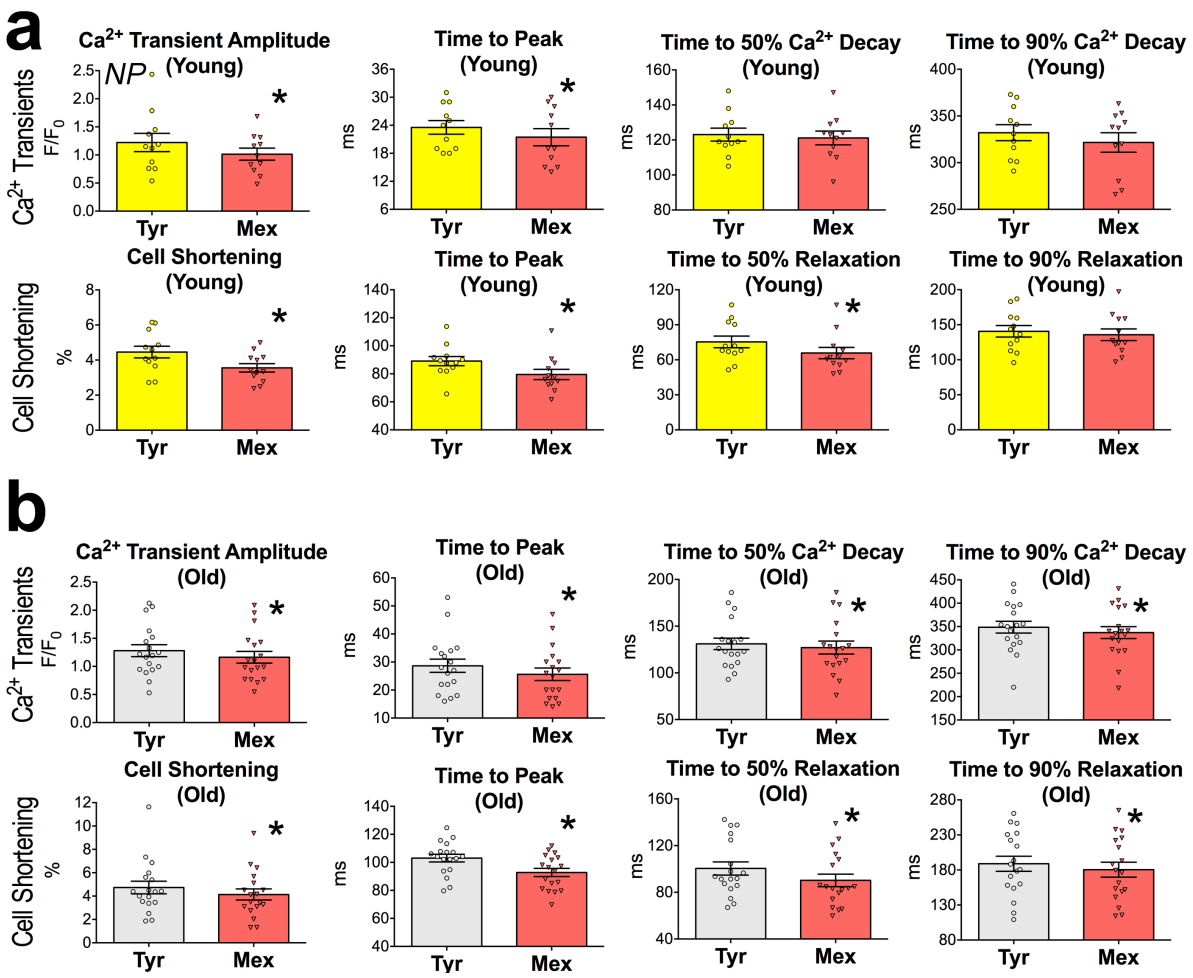

Figure 34. I_{NaL} alters the amplitude and kinetics of Ca^{2+} transients and contraction of LV myocytes. (**a**) Quantitative data for Ca^{2+} transient and cell shortening properties in myocytes from male mice at 3 months, before (Tyr) and after exposure to 10 µM mexiletine (Mex) (Ca^{2+} transients: *n* = 11 cells from 2 hearts; cell shortening *n* = 12 cells from 2 hearts); data are shown as mean ± s.e.m. and scatter plots. **P*<0.05 versus Tyr (paired *t*-test and Wilcoxon signed rank test); *NP*: non-parametric analysis. (**b**) Quantitative data for Ca^{2+} transient and cell shortening properties in myocytes from male mice at 30-31 months, before (Tyr) and after exposure to 10 µM mexiletine (Mex) (Ca^{2+} transients: *n* = 18 cells from 4 hearts; cell shortening *n* = 18 cells from 3 hearts); data are shown as mean ± s.e.m. and scatter plots. **P*<0.05 versus Tyr (paired *t*-test).

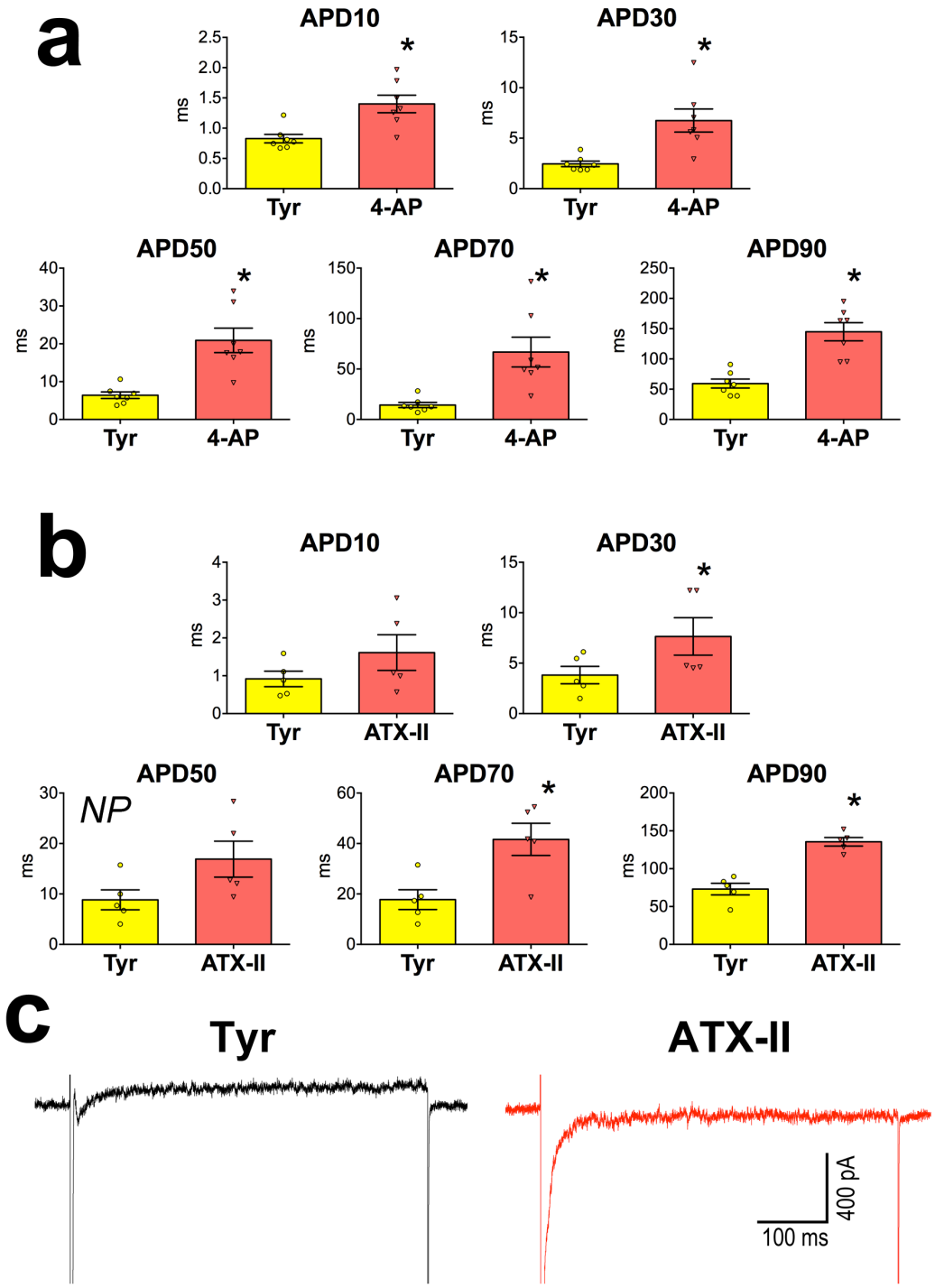

Figure 35. Prolongation of the AP with pharmacological interventions. (**a**) Quantitative AP repolarization properties in myocytes from female mice at 3 months, before (Tyr) and after exposure to 0.5 mM 4-aminopyridine (4-AP) (*n* = 7 cells from 3 hearts); data are shown as mean ± s.e.m. and scatter plots. **P*<0.05 versus Tyr (paired *t*-test). (**b**) Quantitative AP repolarization properties in myocytes from mice at 3 months, before (Tyr) and after exposure to 1 nM anemonia toxin-II (ATX-II) (*n* = 5 cells from 4 hearts); data are shown as mean ± s.e.m. and scatter plots. **P*<0.05 versus Tyr (paired *t*-test and Wilcoxon signed rank test); *NP*: non-parametric analysis. (**c**) Current traces in voltage-clamp mode showing the effects of 1 nM ATX-II on I_{NaL} in a young myocytes. I_{NaL} was elicited by a depolarizing step from V_h -70 mV to -40 mV. Scale bars: 100 ms, 400 pA.

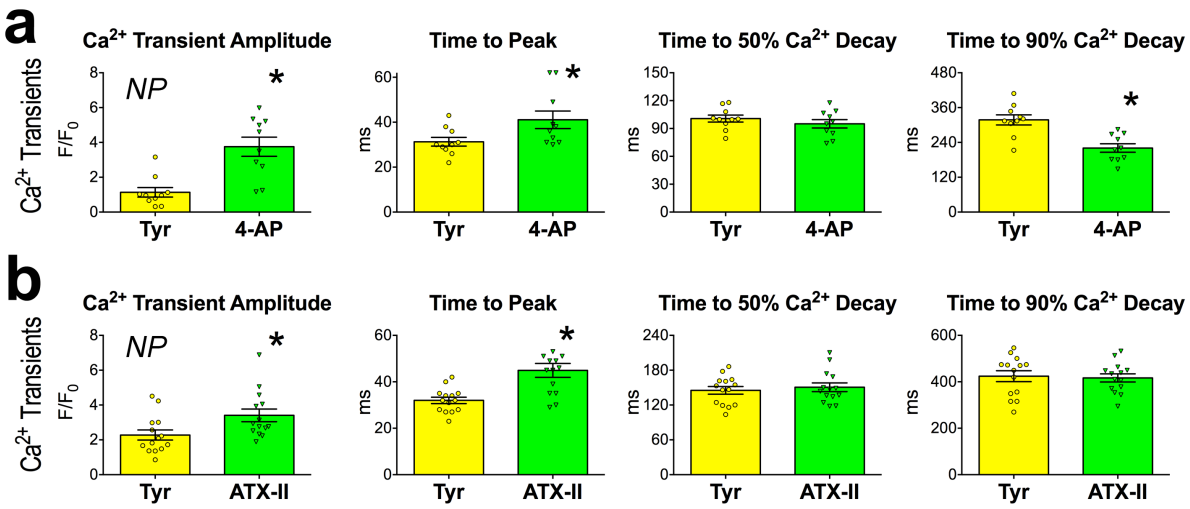

Figure 36. I_{NaL} influences mechanical properties of LV myocytes. (**a**) Quantitative data for Ca^{2+} transient properties in myocytes from male mice at 3-6 months, before (Tyr) and after exposure to 4-aminopyridine (4-AP) (*n* = 10 cells from 2 hearts); data are shown as mean ± s.e.m. and scatter plots. **P*<0.01 versus Tyr (paired *t*-test and Wilcoxon Signed Rank Test); *NP*: non-parametric analysis. (**b**) Quantitative data for Ca^{2+} transient properties in myocytes from mice at 3-9 months, before (Tyr) and after exposure to anemonia toxin-II (ATX-II) (*n* = 14 cells from 4 hearts); data are shown as mean ± s.e.m. and scatter plots. **P*<0.001 versus Tyr (paired *t*-test and Wilcoxon Signed Rank Test); *NP*: non-parametric analysis.

I_{NaL}, myocardial and cardiac function

To determine whether alterations in I_{NaL} and its effects on senescent cardiomyocytes were equally operative at the level of the myocardium, LV papillary muscles from young, 3-6 months, and old, 30-33 months, hearts were studied in an isometric system. Developed tension was similar in both muscles, but twitch kinetics, measured as time of relaxation from the beginning of the contraction, were prolonged with aging (**Figure 37a and 37b**). Inhibition of I_{NaL} with ranolazine or mexiletine reduced developed force and accelerated relaxation times, effects more accentuated in aged muscles with respect to young (**Figure 37c and 37d; Figure 38**). Additionally, to better define the adaptation of papillary muscles to the protracted electrical recovery and enhanced Na^+ entry, 4-AP or ATX-II were employed. 4-AP had a positive inotropic effect which was coupled with faster twitches (**Figure 39a**), whereas enhanced I_{NaL} with ATX-II increased developed force but failed to accelerate contractile dynamics (**Figure 39**).

The influence of Na^+ influx and altered twitch kinetics on diastolic tension of the myocardium was then assessed. The passive length-tension relationship was measured by progressively stretching muscles stimulated at 6 Hz, beginning from near slack length (L_0) to the length at which the muscle developed maximal force (L_{max}). Diastolic tension was higher in the senescent myocardium and inhibition of Na^+ influx shifted the relation to lower passive tension (**Figure 40a**). In contrast, enhancement of Na^+ entry with ATX-II altered the diastolic length-tension curve of young muscles to higher levels (**Figure 40b**).

To determine whether the ameliorated muscle kinetics following inhibition of I_{NaL} had functional consequences on cardiac performance in vivo, LV hemodynamics were assessed in anesthetized young and old mice prior and after inhibition of I_{NaL}, using an intravenous infusion protocol. Infusion of saline had no consequences on cardiac function (**Figure 41a**). In contrast, in old mice blockade of I_{NaL} with ranolazine accelerated kinetic parameters including systolic duration and time constant of pressure decay, together with an increase in –dP/dt (**Figure 41b**). These effects were attenuated in young animals. Importantly, in vivo infusion of ranolazine reduced the slope of the LVEDPV in aged mice (**Figure 41c and 41d**). Thus, I_{NaL} modulates the contractile and diastolic properties of myocytes, myocardium and whole heart.

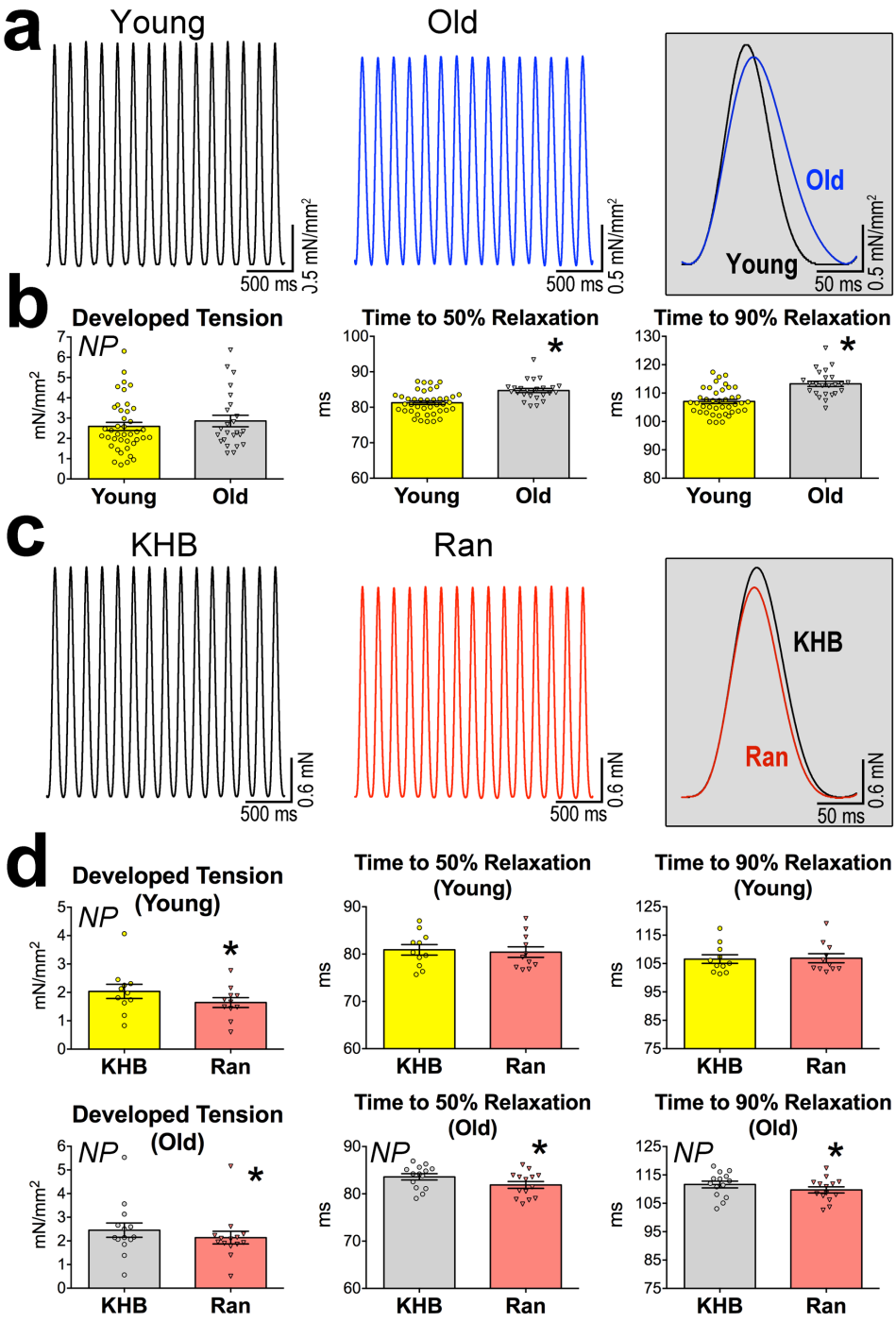

Figure 37. Aging and contractile function of the myocardium. (**a**) Isometric contraction for a young and an old muscle. Superimposed traces are reported in the inset. (**b**) Contractile properties of papillary muscles obtained from male mice at 3-6 months (Young, *n* = 41) and 30-33 months (Old, *n* = 24) are shown as mean ± s.e.m. and scatter plots. **P*<0.001 versus Young (Student's *t*-test); *NP*: non-parametric analysis. (**c**) Isometric contraction for an old muscle prior (black traces) and following exposure to ranolazine (Ran, red traces). Superimposed traces are reported in the inset. (**d**) Data obtained from muscles of male mice at 3-5 months (Young, *n* = 11) and 30-33 months (Old, *n* = 14) before and after exposure to 10 μM ranolazine are shown as mean ± s.e.m. and scatter plots. **P*<0.001 versus KHB (Wilcoxon signed rank test); *NP*: non-parametric analysis.

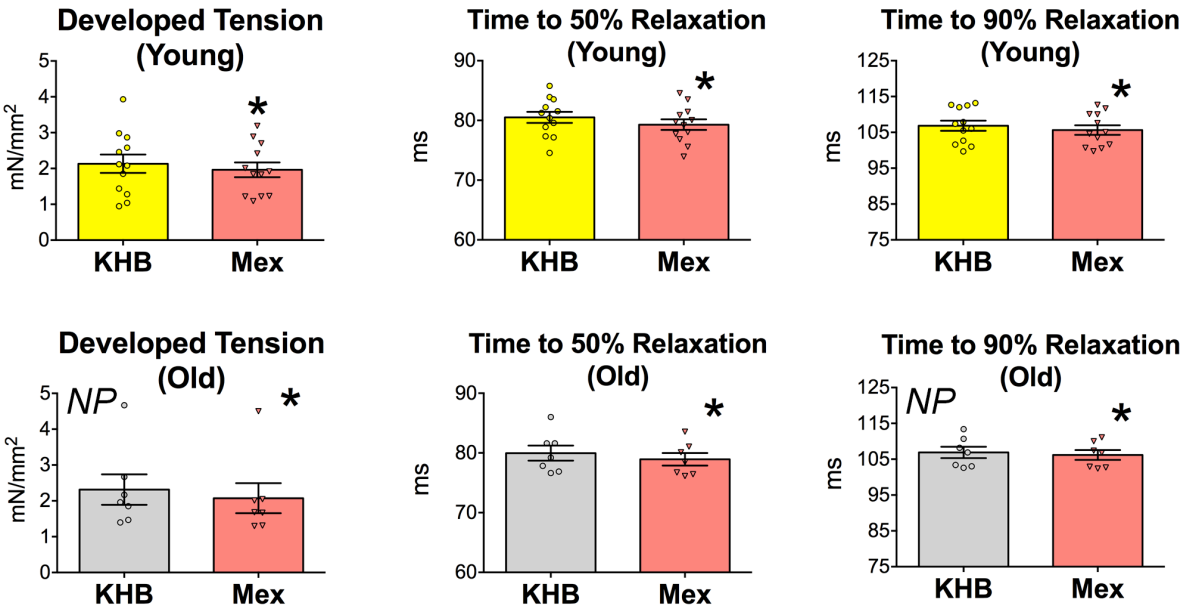

Figure 38. I_{NaL} modulates myocardial contractility. Data obtained from muscles of male mice at 3-6 months (Young, *n* = 12) and 30-33 months (Old, *n* = 7) before and after exposure to 10 µM mexiletine are shown as mean ± s.e.m. and scatter plots. **P*<0.05 versus KHB (paired *t*-test and Wilcoxon signed rank test); *NP*: non-parametric analysis.

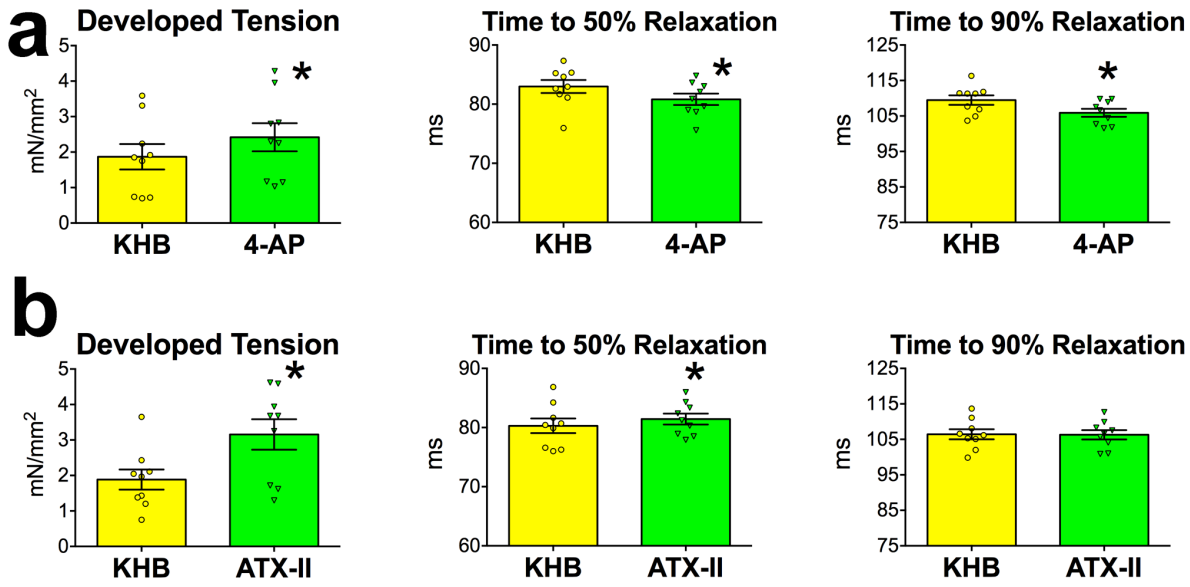

Figure 39. I_{NaL} modulates myocardial function. (**a**) Data obtained from muscles of male mice at 3-6 months (*n* = 9) before and after exposure to 1 mM 4-AP are shown as mean ± s.e.m. and scatter plots. **P*≤0.001 versus KHB (paired *t*-test). (**b**) Data obtained from muscles of mice at 3-9 months (*n* = 9) before and after exposure to 10 nM ATX-II are shown as mean ± s.e.m. and scatter plots. **P*<0.05 versus KHB (paired *t*-test).

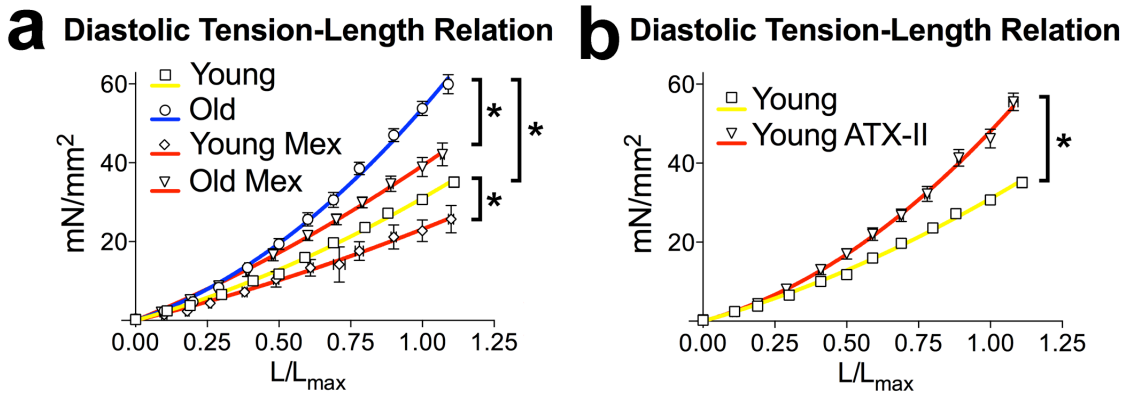

Figure 40. Diastolic tension of the aging myocardium. (**a**) Diastolic length-tension relations for twitching muscle stimulated at 6 Hz in the absence or presence of mexiletine (Mex). Muscles were obtained from male mice at 3 months (Young, *n* = 22; Young-Mex, *n* = 6) and 30-33 months (Old, *n* = 8; Old-Mex, *n* = 8); data are shown as mean ± s.e.m. Data were fitted with a second order polynomial function. Parameters are reported in Table 3. **P*<0.05 between selected fittings (one-way ANOVA with Bonferroni's *post hoc* test). (**b**) Diastolic length-tension relations of muscles from male mice at 3 months in the absence (Young, data as in **a**) and presence of the I_{NaL} enhancer ATX-II (*n* = 10); data are shown as mean ± s.e.m. and fitted with a second order polynomial function. **P*<0.0001 between fittings (Student's *t*-test). Parameters are reported in Table 3.

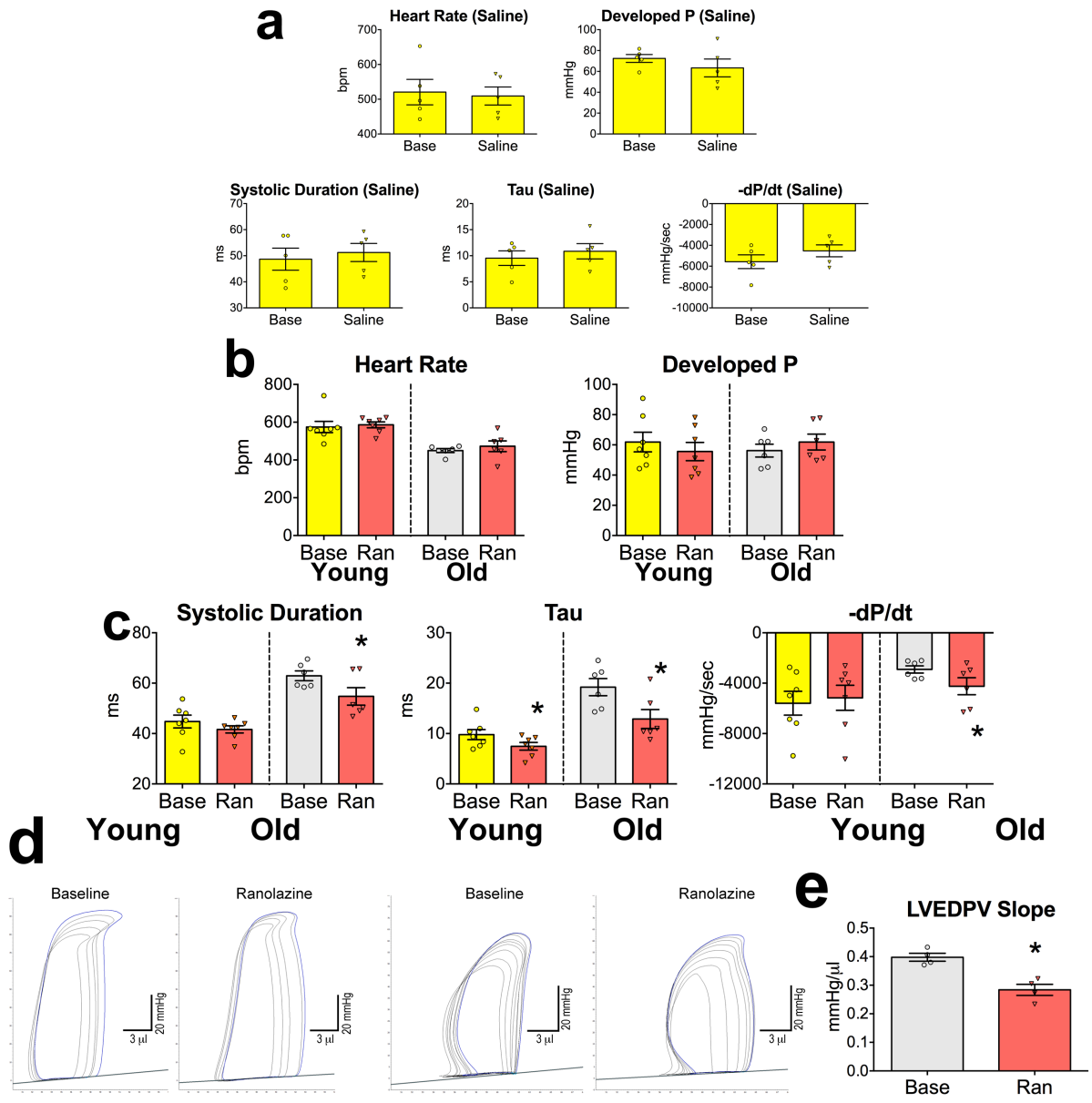

Figure 41. Enhanced I_{NaL} alters the contractile properties of isolated cardiomyocytes. (**a**) Quantitative data for LV hemodynamic parameters obtained in female mice at 7-11 months at baseline (Base) and ~10 min following bolus infusion of saline (*n* = 5). Data are shown as mean ± s.e.m and scatter plots. This intervention did not alter ventricular function. (**b** and **c**) Quantitative data for LV hemodynamic parameters obtained in male mice at 5-6 months (Young) and at 29-33 months (Old) at baseline (Base) and ~10 min following bolus infusion of ranolazine (2.5-5 mg kg^{-1} body weight, i.v.) (Young, *n* = 7; Old *n* = 6). Data are shown as mean ± s.e.m and scatter plots. **P*<0.05 versus Base (paired *t*-test). (**d**) PV loops during inferior vena cava protocol obtained in two male mice at 27 months at baseline and after bolus infusion of ranolazine (2.5 mg kg^{-1} body weight, i.v.). (**e**) Quantitative data for LVEDPV slope obtained in male mice at 27 months at baseline (Base) and following bolus infusion of ranolazine (*n* = 4). Data are shown as mean ± s.e.m and scatter plots. **P*<0.05 versus Base (paired *t*-test).

Molecular determinants of myocyte aging

The gene expression for K^+ and Na^+ channels was evaluated in isolated preparations of young and old myocytes. The transcripts of *Kcnd2*, *Kcnd3* and *Kcnb1* genes, which encode the K^+ channel subunits Kv4.2, Kv4.3 and Kv2.1, respectively, were not affected by aging (**Figure 42a**). In contrast, the mRNAs of the *Kcna4*, *Kcna5*, and *Kcnip2* genes, which encodes the Kv1.4 and Kv1.5 channel subunits, and the Kv channel-interacting protein 2, or KChIP2, were decreased in old myocytes. These changes at the mRNA level are consistent with the attenuated density of Kv currents measured electrophysiologically (see **Figure 17**).

The mRNA levels of the *Scn5a*, *Scn1b*, *Scn2b* and *Scn4b* genes, which encode the Na^+ channel α-subunit Nav1.5, and the Na^+ channel subunits β1, β2 and β4, respectively, did not differ significantly in young and old myocytes (**Figure 42b**). Transcripts of the isoforms of the Na^+ channel α-subunit, typically found in the central nervous system (Nav1.1, Nav1.3, Nav1.6) and skeletal muscle (Nav1.4) were barely detectable or were comparable in young and old cardiomyocytes. Similarly, the expression of Nav1.5 protein was preserved with age, while the levels of the β1 subunit, which modulates Na^+ channel gating (Catterall, 2000; Lopez-Santiago *et al.*, 2007; Maltsev & Undrovinas, 2008; Mishra *et al.*, 2011), were barely detectable, with no measurable differences between young and old samples (**Figure 43**). These findings support the possibility that post-translational modifications or alterations of the Na^+ channel multiprotein complex may have contributed to the alteration of I_{NaL} with age (Abriel & Kass, 2005; Meadows & Isom, 2005; Wagner *et al.*, 2006; Hao *et al.*, 2011; Wagner *et al.*, 2011; Chen-Izu *et al.*, 2015).

qRT-PCR was then employed to define the expression of Ca^{2+} handling molecules in cardiomyocytes. Transcripts of the *Cacna1*, *Slc8a1*, *Ryr2*, and *Pln* genes, which encode, respectively, the Ca^{2+} channel α-subunit Cav1.2, NCX, ryanodine receptor type-2 and phospholamban were comparable in young and old myocytes. However, the mRNA of the *Atpa2a2* gene, encoding SERCA2a, was reduced in old cardiomyocytes, but this change was no longer present at the protein level (**Figure 44**). Thus, the Ca^{2+} handling machinery is largely preserved in aging cardiomyocytes, strengthening the view that the defects in the

electrical properties of these cells contribute in part to the abnormalities in Ca^{2+} cycling identified in the old heart.

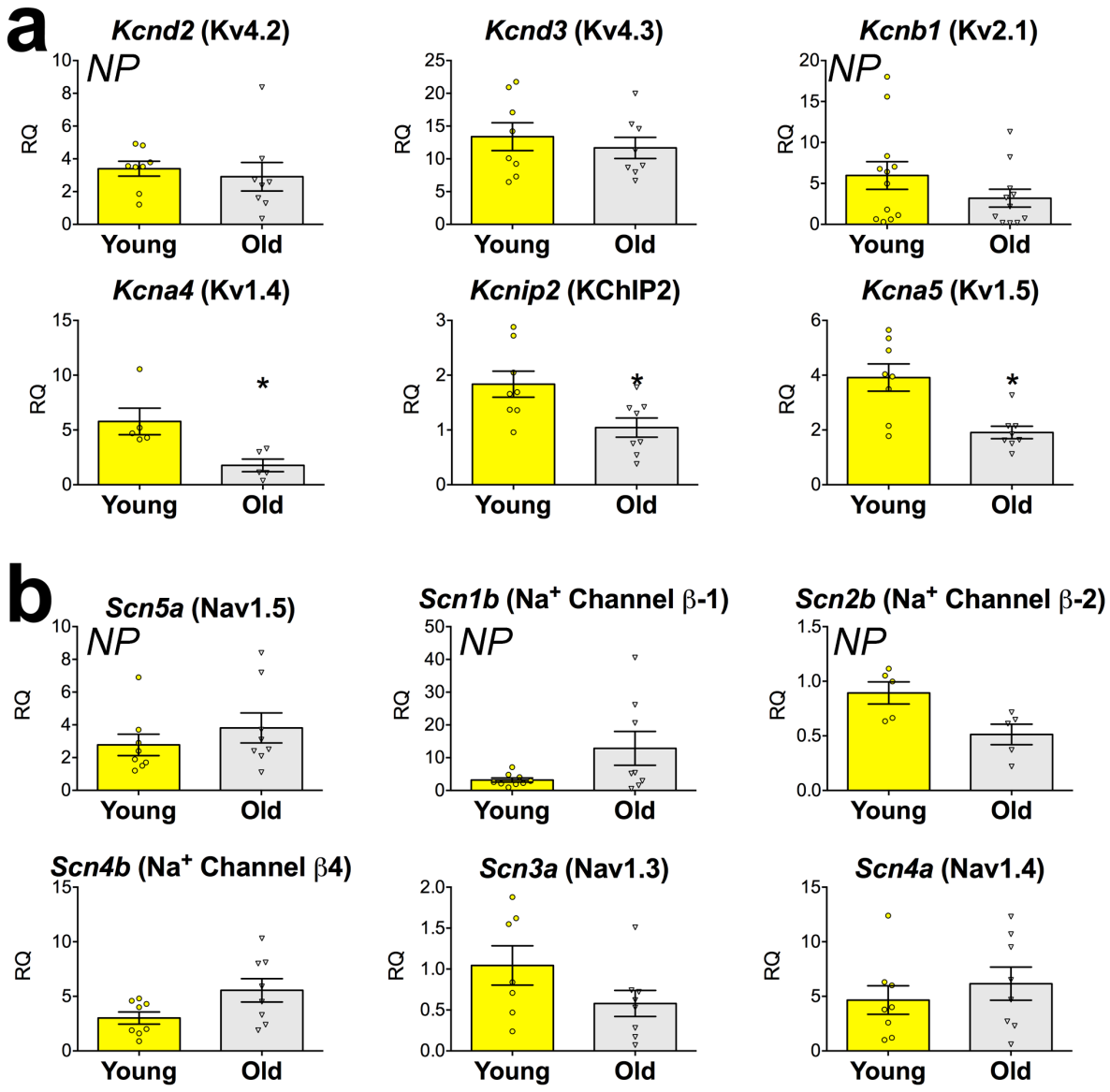

Figure 42. Aging and K^+ and Na^+ channel subunits. (**a**) Quantitative data for expression of genes related to channels mediating I_{to} (*Kcnd2* and *Kcnd3*) and I_{ss} (*Kcnb1*) in myocytes from male mice at 3-4 months (Young, *n* = 8-12) old and 27-33 months (Old, *n* = 8-11) are shown as mean ± s.e.m and scatter plots. RQ: relative quantity with respect to β-2-microglobulin; *NP*: non-parametric analysis. (**b**) Quantitative data for expression of genes related to Na^+ channels in myocytes from male mice at 3-4 months (Young, *n* = 5-8) old and 27-33 months (Old, *n* = 5-8) are shown as mean ± s.e.m and scatter plots. Transcripts for Nav1.1, and Nav1.6 were poorly detectable (data not shown). RQ: relative quantity with respect to β-2-microglobulin; *NP*: non-parametric analysis.

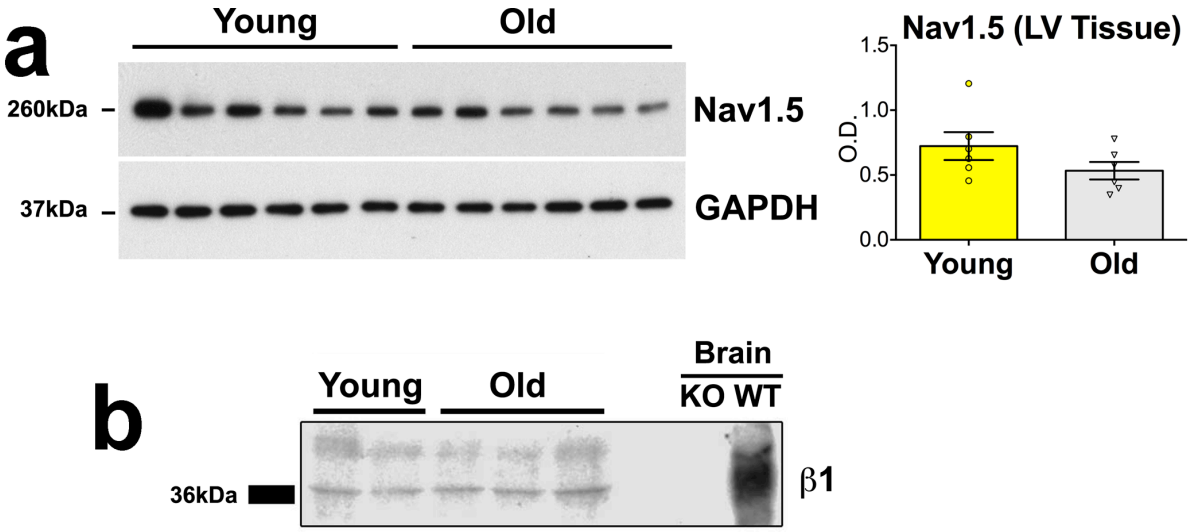

Figure 43. Aging and the expression of transcripts and proteins for K^+ and Na^+ channel subunits. (a) Expression of the Na^+ channel protein subunit Nav1.5 by Western blotting in the LV myocardium of mice at 3-5 months (Young, *n* = 6) and 28 months (Old, *n* = 6). GAPDH is the loading condition. Quantitative data are reported as mean ± s.e.m and scatter plots. (**b**) Expression of Na^+ channel β1 subunit protein by Western blotting in the LV myocardium of mice at 3-4 months (Young) and old 30-31 months (Old). β1 levels in the brains of *Scn1b* null (KO) and wild type (WT) mice were used as negative and positive controls, respectively. A total of 150 µg of LV protein lysate per lane and 25 µg of brain membrane protein per lane were loaded.

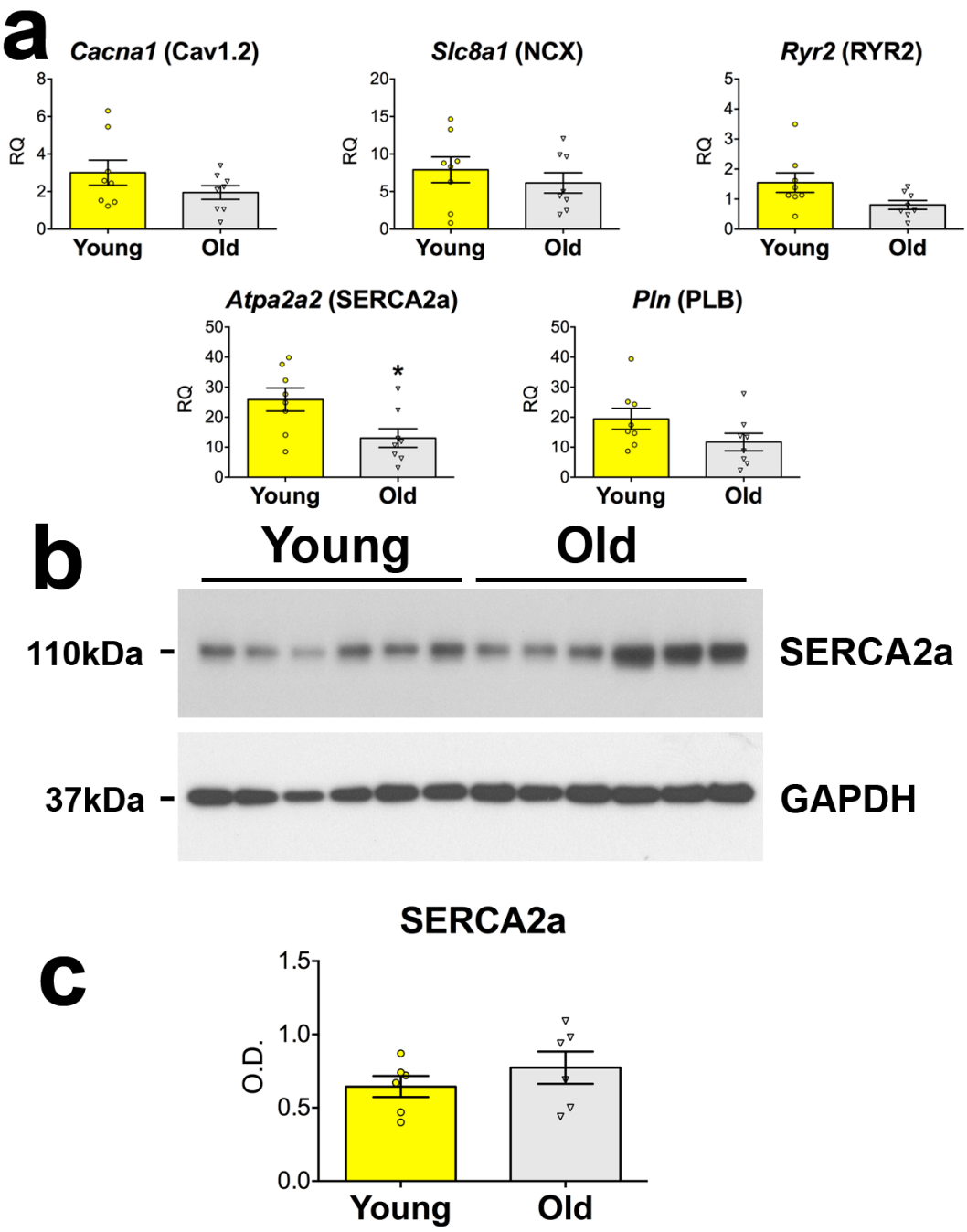

Figure 44. Aging and gene expression profile for Ca^{2+} handling molecules. (**a**) Quantitative data for expression of genes related to L-type Ca^{2+} current (*Cacna1*), NCX (*Slc8a1*), Ryrs, (*Ryr2*), SERCA2a (*Atpa2a2*), and phospholamban (*Pln*) in myocytes from male mice at 3 months (Young, *n* = 6) old and 27-28 months (Old, *n* = 6) are shown as mean ± s.e.m and scatter plots. RQ: relative quantity with respect to β-2-microglobulin; *P<0.05 versus Young (Student's *t*-test). (**b**) Expression of SERCA proteins in LV myocytes from male mice at 3 months (Young, *n* = 6) and old 27-28 months (Old, *n* = 6), by Western blotting. GAPDH is the loading condition. (**c**) Quantitative data for SERCA expression in myocytes shown in **b** are reported as mean ± s.e.m and scatter plots.

Discussion

The results of the present study document that myocardial aging is characterized by a slower electrical repolarization and protracted kinetics of contraction, which contribute to the alterations in the contractile and relaxation function of the old heart. The mechanisms involved in the modifications of ventricular compliance have been predominantly ascribed to collagen accumulation in the myocardial interstitium (Lakatta, 2003; Lakatta & Levy, 2003; Maeder & Kaye, 2009; Borlaug & Paulus, 2011; Schwartz & Zipes, 2011). However, our findings indicate that physiological aging is not associated with diffuse interstitial fibrosis and/or multiple foci of tissue scarring in the myocardium, strengthening the critical role that the remodeled electromechanical characteristics of myocytes have in the diastolic and systolic properties of the aged heart.

The animal model employed here reiterates some of the features of human myocardial aging (Reardon & Malik, 1996; Schwartz & Zipes, 2011). In the absence of systemic hypertension, mice 24-25 month-old show impaired diastolic function; EF and LV end-diastolic volume are preserved, but an increase in LV weight occurs with age. In contrast, in older animals at 30-35 months of age, deterioration of systolic performance, cavitary dilation and myocardial hypertrophy become noticeable, and these changes appear to be independent from the alterations in the diastolic indices observed at earlier time points. The elevated end-diastolic pressure and the perturbations in LV filling found at ~2 years of age are coupled with protracted electrical recovery, corroborating recent observations in patients where the long QT interval has been linked to diastolic dysfunction (Wilcox *et al.*, 2011; Sauer *et al.*, 2012). The prolonged QT interval may be caused by lengthening of the AP and/or by the electrical heterogeneity of the ventricular myocardium, characterized by transmural voltage gradients and dispersion of repolarization (Antzelevitch, 2007). However, our data, in which local epicardial recording was combined with measurements in isolated myocytes, strongly suggest that the shape of the AP is a major determinant of the abnormal electrical recovery of the senescent heart.

Changes in autonomic regulation occur with age (White *et al.*, 1994; Xiao *et al.*, 1994), a factor that may have attenuated the cardiac contractile reserve of the old heart. EF is reduced at 30 months and complete autonomic blockade blunts this difference in conscious animals. However, it has no effects on the protracted electrical repolarization and impaired diastolic indices of ventricular hemodynamics collected in anesthetized mice. Caution has to be exercised when data obtained in conscious and anesthetized animals are compared, although both the in vivo and ex vivo results tend to suggest that defects in neurohumural regulation have modest consequences on the electrical and passive mechanical properties of the senescent myocardium.

Our findings support the notion that the protracted electrical recovery with aging contributes to the alterations in myocyte relengthening and diastolic stiffness of the myocardium. Reduction in the rapidly activating Kv currents and increase of I_{NaL} are the ionic substrates responsible for the prolongation of the AP in aging cells. But whether gene regulatory networks and/or the activity of post-translational modulators are modified in aged cardiomyocytes, impacting on K^+ and Na^+ channel mutiprotein complexes, remains to be determined (Abriel & Kass, 2005; Meadows & Isom, 2005; Wagner *et al.*, 2006; Ozgen *et al.*, 2010; Hao *et al.*, 2011; Wagner *et al.*, 2011; Chen-Izu *et al.*, 2015).

The expression of Kv channel subunits is decreased in the post-infarcted heart in rodents and this condition is associated with reduced outward K^+ current, prolonged AP and increased Ca^{2+} transient amplitude (Kaprielian *et al.*, 1999). Although limited information is available in diseased mouse models with altered Na^+ channel levels, genetic deletion of *Scn1b* in mouse cardiomyocyte results in longer AP duration, increased Ca^{2+} transients and slower Ca^{2+} decay; these defects, however, are reversed by low dose of TTX (Lin *et al.*, 2015). These observations and the current data in aging mice are consistent with the critical role that Kv and Na^+ regulatory channel subunits have in modulating the electrical and mechanical properties of cardiomyocytes.

Reduced outward Kv currents and enhanced I_{NaL} contribute to the electrical recovery of old myocytes by altering, respectively, the early and late repolarization phase of the AP.

Inhibition of I_{NaL} in old myocytes critically shortens APD90 to values found in young cells. However, this pharmacological intervention has minimal effects on the initial repolarization phase of the AP. Similarly, reduction of I_{NaL} in vivo reduces the duration of the QT interval in old mice restoring partly the electrical recovery of the myocardium. The negligible impact of ranolazine and mexiletine on the QT interval in young mice may reflect the attenuated density of I_{NaL} found in isolated cardiomyocytes.

In the failing heart, SERCA activity is attenuated and results in abnormal Ca^{2+} handling, which is centrally involved in the decline of cardiomyocyte performance (Kranias & Hajjar, 2012). However, SERCA protein is preserved in aging myocytes, suggesting that the cellular mechanisms implicated in the aging myopathy may be distinct from those typically found in chronic heart failure (Kranias & Hajjar, 2012). Although a potential role of SERCA with defective Ca^{2+} re-uptake has to be considered in the development of the decompensated aging heart, the increase in I_{NaL}, together with the modifications in the electrical properties of cardiomyocytes, has to be viewed as an important variable of the progressive alterations in contractile kinetics and deterioration in diastolic and systolic properties of the senescent muscle.

Our results indicate that enhanced I_{NaL} mediates protracted repolarization of the AP and Na^{+} influx, potentiating the amplitude of Ca^{2+} transients and exerting a positive inotropic effect. Similarly, the decrease in Kv currents favors the prolongation of the AP promoting Ca^{2+} influx via L-type channels and reduced Ca^{2+} efflux via NCX (Sah *et al.*, 2001; Janczewski *et al.*, 2002; Sah *et al.*, 2003; Rota *et al.*, 2007). Yet, the amplitude of Ca^{2+} transients and cell contractility are maintained with aging, in spite of prolonged AP duration, suggesting that the cellular defects in old myocytes condition the efficiency of the positive APD-inotropic relationship, which may be in part attributed to the reduced SR Ca^{2+} load. Thus, the changes in I_{NaL} and Kv currents may be interpreted as necessary responses aiming at the preservation of systolic function at the expense of a loss in cellular and ventricular compliance.

The prolonged AP in aging myocytes correlates with the delayed peak of Ca^{2+} transients and cell shortening, indicating that the slower repolarization phase sustains the Ca^{2+} induced-Ca^{2+} release mechanism, increasing the translocation of Ca^{2+} from the SR to the cytoplasm. The ionic events underlying the positive inotropic action of enhanced I_{NaL} and the protracted AP may comprise an increased Na^+ influx and enhanced $[Na^+]_i$ (Maltsev & Undrovinas, 2008). The higher intracellular Na^+ load is balanced by an increase in intracellular Ca^{2+} since the elevated Na^+ attenuates the extrusion of Ca^{2+} via the NCX (Sah *et al.*, 2003; Maltsev & Undrovinas, 2008; Zaza & Rocchetti, 2013). This form of inotropic support of myocyte contractility appears to be implicated in the complex adaptation of the myocardium to chronological aging. I_{NaL} may have a dual effect: it prolongs the AP and it influences indirectly Ca^{2+} load. These variables affect, on the one hand, systolic Ca^{2+} release and contraction and, on the other, diastolic Ca^{2+} clearance and relaxation.

The central role of Na^+ influx and enhanced Na^+ load on the protracted Ca^{2+} transient decay in aged myocytes is corroborated by the findings in which the AP was prolonged by inhibition of Kv currents or enhancement of I_{NaL}. Both approaches led to an increase in Ca^{2+} transient amplitude, but differentially modulated the timing of Ca^{2+} decay. Similarly, these interventions had a positive inotropic action on papillary muscles, but differently affected contractile dynamics: twitch kinetics were shortened with 4-AP, but were not altered with ATX-II. Importantly, when $[Na^+]_i$ was stabilized using cells dialysis and patch-clamp, differences in Ca^{2+} transient decay between young and old cells were abrogated. The faster caffeine-induced Ca^{2+} transient decay observed in old myocytes is suggestive of an increased NCX activity, which may reflect an adaptation to the altered Na^+ load.

Inhibition of I_{NaL} in old myocytes shortens the AP and corrects the kinetics of Ca^{2+} transients, cell contraction and relaxation. Similarly, the repolarization and compliance of the senescent myocardium is restored, but muscle developed tension is attenuated. I_{NaL} modulates both the systolic and diastolic properties of the myocardium. However, in old mice, inhibition of I_{NaL} in vivo ameliorated diastolic indices and shortened systolic duration without interfering with developed pressure. Whether the blunted effects on developed pressure are due to

compensatory adaptations inherent in the protocol employed requires further analysis. Thus, chronological age affects the electrical and molecular identity of cardiomyocytes, which are critical determinants of the pathological manifestations of the old heart.

Prolongation of the AP in cardiomyocytes is typically observed in the hypertrophied and failing heart (Tomaselli & Marban, 1999) with major consequences on intracellular Ca^{2+} homeostasis and contractile force developed by the myocardium (Tomaselli & Marban, 1999; Signore *et al.*, 2013). Reduction in repolarizing K^+ Kv currents has been recognized as an important mediator of the AP prolongation in myocytes from human hearts and animal models in a variety of physiological and pathological conditions, including ischemic cardiomyopathy (Rozanski *et al.*, 1998; Kaprielian *et al.*, 1999), hypertrophic cardiomyopathy (Coppini *et al.*, 2013), hypertension (Cerbai *et al.*, 1994), pressure overload (Volk *et al.*, 2001), diabetes (Nishiyama *et al.*, 2001; Pereira *et al.*, 2006; Lu *et al.*, 2007; Panguluri *et al.*, 2013; Lopez-Izquierdo *et al.*, 2014; Sato *et al.*, 2014), aging (Walker *et al.*, 1993) and heart failure (Beuckelmann *et al.*, 1993; Kaab *et al.*, 1996; Tomaselli & Marban, 1999). Also, I_{NaL} has emerged as important player in the lengthening of the AP in myocytes from patients with hypertrophic cardiomyopathy (Coppini *et al.*, 2013) and heart failure (Maltsev *et al.*, 2007). Experimentally, inhibition of I_{NaL} has resulted in an amelioration of diastolic properties of myocytes and myocardium (Sossalla *et al.*, 2008; Undrovinas *et al.*, 2010; Coppini *et al.*, 2013) raising the possibility that inhibition of I_{NaL} may be a therapeutic strategy to correct electrical and functional defects of the aged heart.

Acknowledgements

Data presented in this thesis have been published in *Nature Communication* (Nature Publishing Group, a division of Macmillan Publishers):

Signore S, Sorrentino A, Borghetti G, Cannata A, Meo M, Zhou Y, Kannappan R, Pasqualini F, O'Malley H, Sundman M, Tsigkas N, Zhang E, Arranto C, Mangiaracina C, Isobe K, Sena BF, Kim J, Goichberg P, Nahrendorf M, Isom LL, Leri A, Anversa P, Rota M. Late Na^+ current and protracted electrical recovery are critical determinants of the aging myopathy. Nat Commun. 2015 Nov 6;6:8803.

References

Abriel H & Kass RS. (2005). Regulation of the voltage-gated cardiac sodium channel Nav1.5 by interacting proteins. *Trends in cardiovascular medicine* **15,** 35-40.

Antzelevitch C. (2007). Ionic, molecular, and cellular bases of QT-interval prolongation and torsade de pointes. *Europace : European pacing, arrhythmias, and cardiac electrophysiology : journal of the working groups on cardiac pacing, arrhythmias, and cardiac cellular electrophysiology of the European Society of Cardiology* **9 Suppl 4,** iv4-15.

Bauer M, Cheng S, Jain M, Ngoy S, Theodoropoulos C, Trujillo A, Lin FC & Liao R. (2011). Echocardiographic speckle-tracking based strain imaging for rapid cardiovascular phenotyping in mice. *Circ Res* **108,** 908-916.

Bers DM. (2002). Cardiac excitation-contraction coupling. *Nature* **415,** 198-205.

Beuckelmann DJ, Nabauer M & Erdmann E. (1993). Alterations of K+ currents in isolated human ventricular myocytes from patients with terminal heart failure. *Circ Res* **73,** 379-385.

Borlaug BA & Paulus WJ. (2011). Heart failure with preserved ejection fraction: pathophysiology, diagnosis, and treatment. *Eur Heart J* **32,** 670-679.

Bouchard RA, Clark RB & Giles WR. (1995). Effects of action potential duration on excitation-contraction coupling in rat ventricular myocytes. Action potential voltage-clamp measurements. *Circ Res* **76,** 790-801.

Brouillette J, Clark RB, Giles WR & Fiset C. (2004). Functional properties of K+ currents in adult mouse ventricular myocytes. *J Physiol* **559,** 777-798.

Catterall WA. (2000). From ionic currents to molecular mechanisms: the structure and function of voltage-gated sodium channels. *Neuron* **26,** 13-25.

Cerbai E, Barbieri M, Li Q & Mugelli A. (1994). Ionic basis of action potential prolongation of hypertrophied cardiac myocytes isolated from hypertensive rats of different ages. *Cardiovasc Res* **28,** 1180-1187.

Chen-Izu Y, Shaw RM, Pitt GS, Yarov-Yarovoy V, Sack JT, Abriel H, Aldrich RW, Belardinelli L, Cannell MB, Catterall WA, Chazin WJ, Chiamvimonvat N, Deschenes I, Grandi E, Hund TJ, Izu LT, Maier LS, Maltsev VA, Marionneau C, Mohler PJ, Rajamani S, Rasmusson RL, Sobie EA, Clancy CE & Bers DM. (2015). Na+ channel function, regulation, structure, trafficking and sequestration. *J Physiol* **593,** 1347-1360.

Cingolani OH & Kass DA. (2011). Pressure-volume relation analysis of mouse ventricular function. *Am J Physiol Heart Circ Physiol* **301,** H2198-2206.

Coppini R, Ferrantini C, Yao L, Fan P, Del Lungo M, Stillitano F, Sartiani L, Tosi B, Suffredini S, Tesi C, Yacoub M, Olivotto I, Belardinelli L, Poggesi C, Cerbai E & Mugelli A. (2013). Late sodium current inhibition reverses electromechanical dysfunction in human hypertrophic cardiomyopathy. *Circulation* **127,** 575-584.

Correia LC, Lakatta EG, O'Connor FC, Becker LC, Clulow J, Townsend S, Gerstenblith G & Fleg JL. (2002). Attenuated cardiovascular reserve during prolonged submaximal

cycle exercise in healthy older subjects. *Journal of the American College of Cardiology* **40,** 1290-1297.

D'Souza A, Bucchi A, Johnsen AB, Logantha SJ, Monfredi O, Yanni J, Prehar S, Hart G, Cartwright E, Wisloff U, Dobryznski H, DiFrancesco D, Morris GM & Boyett MR. (2014). Exercise training reduces resting heart rate via downregulation of the funny channel HCN4. *Nat Commun* **5,** 3775.

De Luca A, Pierno S, Liantonio A, Desaphy JF, Natuzzi F, Didonna MP, Ferrannini E, Jockusch H, Franchini C, Lentini G, Corbo F, Tortorella V & Camerino DC. (2004). New potent mexiletine and tocainide analogues evaluated in vivo and in vitro as antimyotonic agents on the myotonic ADR mouse. *Neuromuscular disorders : NMD* **14,** 405-416.

Fabiato A. (1983). Calcium-induced release of calcium from the cardiac sarcoplasmic reticulum. *The American journal of physiology* **245,** C1-14.

Ferreira-Martins J, Rondon-Clavo C, Tugal D, Korn JA, Rizzi R, Padin-Iruegas ME, Ottolenghi S, De Angelis A, Urbanek K, Ide-Iwata N, D'Amario D, Hosoda T, Leri A, Kajstura J, Anversa P & Rota M. (2009). Spontaneous calcium oscillations regulate human cardiac progenitor cell growth. *Circ Res* **105,** 764-774.

Fischer TH, Herting J, Mason FE, Hartmann N, Watanabe S, Nikolaev VO, Sprenger JU, Fan P, Yiao L, Popov AF, Danner BC, Schondube F, Belardinelli L, Hasenfuss G, Maier LS & Sossalla S. (2015). Late INa increases diastolic SR-Ca2+-leak in atrial myocardium by activating PKA and CaMKII. *Cardiovasc Res*.

Gao Y, Xue X, Hu D, Liu W, Yuan Y, Sun H, Li L, Timothy KW, Zhang L, Li C & Yan GX. (2013). Inhibition of late sodium current by mexiletine: a novel pharmotherapeutical approach in timothy syndrome. *Circ Arrhythm Electrophysiol* **6,** 614-622.

Gehrmann J, Hammer PE, Maguire CT, Wakimoto H, Triedman JK & Berul CI. (2000). Phenotypic screening for heart rate variability in the mouse. *Am J Physiol Heart Circ Physiol* **279,** H733-740.

Goichberg P, Bai Y, D'Amario D, Ferreira-Martins J, Fiorini C, Zheng H, Signore S, del Monte F, Ottolenghi S, D'Alessandro DA, Michler RE, Hosoda T, Anversa P, Kajstura J, Rota M & Leri A. (2011). The ephrin A1-EphA2 system promotes cardiac stem cell migration after infarction. *Circ Res* **108,** 1071-1083.

Hagendorff A, Schumacher B, Kirchhoff S, Luderitz B & Willecke K. (1999). Conduction disturbances and increased atrial vulnerability in Connexin40-deficient mice analyzed by transesophageal stimulation. *Circulation* **99,** 1508-1515.

Hao X, Zhang Y, Zhang X, Nirmalan M, Davies L, Konstantinou D, Yin F, Dobrzynski H, Wang X, Grace A, Zhang H, Boyett M, Huang CL & Lei M. (2011). TGF-beta1-mediated fibrosis and ion channel remodeling are key mechanisms in producing the sinus node dysfunction associated with SCN5A deficiency and aging. *Circ Arrhythm Electrophysiol* **4,** 397-406.

Hees PS, Fleg JL, Mirza ZA, Ahmed S, Siu CO & Shapiro EP. (2006). Effects of normal aging on left ventricular lusitropic, inotropic, and chronotropic responses to dobutamine. *Journal of the American College of Cardiology* **47,** 1440-1447.

Janczewski AM, Spurgeon HA & Lakatta EG. (2002). Action potential prolongation in cardiac myocytes of old rats is an adaptation to sustain youthful intracellular Ca2+ regulation. *J Mol Cell Cardiol* **34,** 641-648.

Joyner RW, Picone J, Veenstra R & Rawling D. (1983). Propagation through electrically coupled cells. Effects of regional changes in membrane properties. *Circ Res* **53,** 526-534.

Kaab S, Nuss HB, Chiamvimonvat N, O'Rourke B, Pak PH, Kass DA, Marban E & Tomaselli GF. (1996). Ionic mechanism of action potential prolongation in ventricular myocytes from dogs with pacing-induced heart failure. *Circ Res* **78,** 262-273.

Kaprielian R, Wickenden AD, Kassiri Z, Parker TG, Liu PP & Backx PH. (1999). Relationship between K+ channel down-regulation and [Ca2+]i in rat ventricular myocytes following myocardial infarction. *J Physiol* **517 (Pt 1),** 229-245.

Knollmann BC, Kirchhof P, Sirenko SG, Degen H, Greene AE, Schober T, Mackow JC, Fabritz L, Potter JD & Morad M. (2003). Familial hypertrophic cardiomyopathy-linked mutant troponin T causes stress-induced ventricular tachycardia and Ca2+-dependent action potential remodeling. *Circ Res* **92,** 428-436.

Korte T, Fuchs M, Guener Z, v Bonin J, de Sousa M, Niehaus M, Tebbenjohanns J & Drexler H. (2002). In-vivo electrophysiological study in mice with chronic anterior myocardial infarction. *J Interv Card Electrophysiol* **6,** 121-132.

Kranias EG & Hajjar RJ. (2012). Modulation of cardiac contractility by the phospholamban/SERCA2a regulatome. *Circ Res* **110,** 1646-1660.

Krege JH, Hodgin JB, Hagaman JR & Smithies O. (1995). A noninvasive computerized tail-cuff system for measuring blood pressure in mice. *Hypertension* **25,** 1111-1115.

Lakatta EG. (2003). Arterial and cardiac aging: major shareholders in cardiovascular disease enterprises: Part III: cellular and molecular clues to heart and arterial aging. *Circulation* **107,** 490-497.

Lakatta EG & Levy D. (2003). Arterial and cardiac aging: major shareholders in cardiovascular disease enterprises: Part II: the aging heart in health: links to heart disease. *Circulation* **107,** 346-354.

Lin X, O'Malley H, Chen C, Auerbach D, Foster M, Shekhar A, Zhang M, Coetzee W, Jalife J, Fishman GI, Isom L & Delmar M. (2015). Scn1b deletion leads to increased tetrodotoxin-sensitive sodium current, altered intracellular calcium homeostasis and arrhythmias in murine hearts. *J Physiol* **593,** 1389-1407.

Liu J, Kim KH, London B, Morales MJ & Backx PH. (2011). Dissection of the voltage-activated potassium outward currents in adult mouse ventricular myocytes: I(to,f), I(to,s), I(K,slow1), I(K,slow2), and I(ss). *Basic research in cardiology* **106,** 189-204.

Lopez-Izquierdo A, Pereira RO, Wende AR, Punske BB, Abel ED & Tristani-Firouzi M. (2014). The absence of insulin signaling in the heart induces changes in potassium channel expression and ventricular repolarization. *Am J Physiol Heart Circ Physiol* **306,** H747-754.

Lopez-Santiago LF, Meadows LS, Ernst SJ, Chen C, Malhotra JD, McEwen DP, Speelman A, Noebels JL, Maier SK, Lopatin AN & Isom LL. (2007). Sodium channel Scn1b null mice exhibit prolonged QT and RR intervals. *J Mol Cell Cardiol* **43,** 636-647.

Lovelock JD, Monasky MM, Jeong EM, Lardin HA, Liu H, Patel BG, Taglieri DM, Gu L, Kumar P, Pokhrel N, Zeng D, Belardinelli L, Sorescu D, Solaro RJ & Dudley SC, Jr. (2012). Ranolazine improves cardiac diastolic dysfunction through modulation of myofilament calcium sensitivity. *Circ Res* **110,** 841-850.

Lu Z, Jiang YP, Xu XH, Ballou LM, Cohen IS & Lin RZ. (2007). Decreased L-type Ca2+ current in cardiac myocytes of type 1 diabetic Akita mice due to reduced phosphatidylinositol 3-kinase signaling. *Diabetes* **56,** 2780-2789.

Maeder MT & Kaye DM. (2009). Heart failure with normal left ventricular ejection fraction. *Journal of the American College of Cardiology* **53,** 905-918.

Maltsev VA, Sabbah HN, Higgins RS, Silverman N, Lesch M & Undrovinas AI. (1998). Novel, ultraslow inactivating sodium current in human ventricular cardiomyocytes. *Circulation* **98,** 2545-2552.

Maltsev VA, Silverman N, Sabbah HN & Undrovinas AI. (2007). Chronic heart failure slows late sodium current in human and canine ventricular myocytes: implications for repolarization variability. *Eur J Heart Fail* **9,** 219-227.

Maltsev VA & Undrovinas A. (2008). Late sodium current in failing heart: friend or foe? *Progress in biophysics and molecular biology* **96,** 421-451.

Meadows LS & Isom LL. (2005). Sodium channels as macromolecular complexes: implications for inherited arrhythmia syndromes. *Cardiovasc Res* **67,** 448-458.

Mishra S, Undrovinas NA, Maltsev VA, Reznikov V, Sabbah HN & Undrovinas A. (2011). Post-transcriptional silencing of SCN1B and SCN2B genes modulates late sodium current in cardiac myocytes from normal dogs and dogs with chronic heart failure. *Am J Physiol Heart Circ Physiol* **301,** H1596-1605.

Moreno JD & Clancy CE. (2012). Pathophysiology of the cardiac late Na current and its potential as a drug target. *J Mol Cell Cardiol* **52,** 608-619.

Mozaffarian D, Benjamin EJ, Go AS, Arnett DK, Blaha MJ, Cushman M, de Ferranti S, Despres JP, Fullerton HJ, Howard VJ, Huffman MD, Judd SE, Kissela BM, Lackland DT, Lichtman JH, Lisabeth LD, Liu S, Mackey RH, Matchar DB, McGuire DK, Mohler ER, 3rd, Moy CS, Muntner P, Mussolino ME, Nasir K, Neumar RW, Nichol G, Palaniappan L, Pandey DK, Reeves MJ, Rodriguez CJ, Sorlie PD, Stein J, Towfighi A, Turan TN, Virani SS, Willey JZ, Woo D, Yeh RW, Turner MB, American Heart Association Statistics C & Stroke Statistics S. (2015). Heart disease and stroke statistics--2015 update: a report from the American Heart Association. *Circulation* **131,** e29-322.

Nahrendorf M, Streif JU, Hiller KH, Hu K, Nordbeck P, Ritter O, Sosnovik D, Bauer L, Neubauer S, Jakob PM, Ertl G, Spindler M & Bauer WR. (2006). Multimodal functional cardiac MRI in creatine kinase-deficient mice reveals subtle abnormalities in myocardial perfusion and mechanics. *Am J Physiol Heart Circ Physiol* **290,** H2516-2521.

Nerbonne JM & Kass RS. (2005). Molecular physiology of cardiac repolarization. *Physiol Rev* **85,** 1205-1253.

Nishiyama A, Ishii DN, Backx PH, Pulford BE, Birks BR & Tamkun MM. (2001). Altered K(+) channel gene expression in diabetic rat ventricle: isoform switching between Kv4.2 and Kv1.4. *Am J Physiol Heart Circ Physiol* **281,** H1800-1807.

Oudit GY, Kassiri Z, Sah R, Ramirez RJ, Zobel C & Backx PH. (2001). The molecular physiology of the cardiac transient outward potassium current (I(to)) in normal and diseased myocardium. *J Mol Cell Cardiol* **33,** 851-872.

Ozgen N, Lau DH, Shlapakova IN, Sherman W, Feinmark SJ, Danilo P, Jr. & Rosen MR. (2010). Determinants of CREB degradation and KChIP2 gene transcription in cardiac memory. *Heart Rhythm* **7,** 964-970.

Pacher P, Nagayama T, Mukhopadhyay P, Batkai S & Kass DA. (2008). Measurement of cardiac function using pressure-volume conductance catheter technique in mice and rats. *Nat Protoc* **3,** 1422-1434.

Panguluri SK, Tur J, Chapalamadugu KC, Katnik C, Cuevas J & Tipparaju SM. (2013). MicroRNA-301a mediated regulation of Kv4.2 in diabetes: identification of key modulators. *PLoS One* **8,** e60545.

Pereira L, Matthes J, Schuster I, Valdivia HH, Herzig S, Richard S & Gomez AM. (2006). Mechanisms of [Ca2+]i transient decrease in cardiomyopathy of db/db type 2 diabetic mice. *Diabetes* **55,** 608-615.

Pfeffer MA, Pfeffer JM, Fishbein MC, Fletcher PJ, Spadaro J, Kloner RA & Braunwald E. (1979). Myocardial infarct size and ventricular function in rats. *Circ Res* **44,** 503-512.

Plotnikov SV, Millard AC, Campagnola PJ & Mohler WA. (2006). Characterization of the myosin-based source for second-harmonic generation from muscle sarcomeres. *Biophys J* **90,** 693-703.

Ram R, Mickelsen DM, Theodoropoulos C & Blaxall BC. (2011). New approaches in small animal echocardiography: imaging the sounds of silence. *Am J Physiol Heart Circ Physiol* **301,** H1765-1780.

Reardon M & Malik M. (1996). QT interval change with age in an overtly healthy older population. *Clinical cardiology* **19,** 949-952.

Roden DM & Viswanathan PC. (2005). Genetics of acquired long QT syndrome. *J Clin Invest* **115,** 2025-2032.

Roell W, Lewalter T, Sasse P, Tallini YN, Choi BR, Breitbach M, Doran R, Becher UM, Hwang SM, Bostani T, von Maltzahn J, Hofmann A, Reining S, Eiberger B, Gabris B, Pfeifer A, Welz A, Willecke K, Salama G, Schrickel JW, Kotlikoff MI & Fleischmann BK. (2007). Engraftment of connexin 43-expressing cells prevents post-infarct arrhythmia. *Nature* **450,** 819-824.

Rota M, Boni A, Urbanek K, Padin-Iruegas ME, Kajstura TJ, Fiore G, Kubo H, Sonnenblick EH, Musso E, Houser SR, Leri A, Sussman MA & Anversa P. (2005). Nuclear targeting of Akt enhances ventricular function and myocyte contractility. *Circ Res* **97,** 1332-1341.

Rota M, Hosoda T, De Angelis A, Arcarese ML, Esposito G, Rizzi R, Tillmanns J, Tugal D, Musso E, Rimoldi O, Bearzi C, Urbanek K, Anversa P, Leri A & Kajstura J. (2007). The young mouse heart is composed of myocytes heterogeneous in age and function. *Circ Res* **101,** 387-399.

Rota M & Vassalle M. (2003). Patch-clamp analysis in canine cardiac Purkinje cells of a novel sodium component in the pacemaker range. *J Physiol* **548,** 147-165.

Rozanski GJ, Xu Z, Zhang K & Patel KP. (1998). Altered K+ current of ventricular myocytes in rats with chronic myocardial infarction. *The American journal of physiology* **274,** H259-265.

Saba S, London B & Ganz L. (2003). Autonomic blockade unmasks maturational differences in rate-dependent atrioventricular nodal conduction and facilitation in the mouse. *Journal of cardiovascular electrophysiology* **14,** 191-195.

Sah R, Ramirez RJ, Kaprielian R & Backx PH. (2001). Alterations in action potential profile enhance excitation-contraction coupling in rat cardiac myocytes. *J Physiol* **533,** 201-214.

Sah R, Ramirez RJ, Oudit GY, Gidrewicz D, Trivieri MG, Zobel C & Backx PH. (2003). Regulation of cardiac excitation-contraction coupling by action potential repolarization: role of the transient outward potassium current (I(to)). *J Physiol* **546,** 5-18.

Sato T, Kobayashi T, Kuno A, Miki T, Tanno M, Kouzu H, Itoh T, Ishikawa S, Kojima T, Miura T & Tohse N. (2014). Type 2 diabetes induces subendocardium-predominant reduction in transient outward K+ current with downregulation of Kv4.2 and KChIP2. *Am J Physiol Heart Circ Physiol* **306,** H1054-1065.

Sauer A, Wilcox JE, Andrei AC, Passman R, Goldberger JJ & Shah SJ. (2012). Diastolic electromechanical coupling: association of the ECG T-peak to T-end interval with echocardiographic markers of diastolic dysfunction. *Circ Arrhythm Electrophysiol* **5,** 537-543.

Schwartz J & Zipes D. (2011). Cardiovascular disease in the elderly. In *Braunwald's Heart Disease: A Textbook of Cardiovascular Medicine 9th ed*, ed. Bonow R, Mann D, Zipes D, Libby P & eds., pp. 1727-1753. Saunders, Philadelphia, Pa.

Sicouri S, Antzelevitch D, Heilmann C & Antzelevitch C. (1997). Effects of sodium channel block with mexiletine to reverse action potential prolongation in in vitro models of the long term QT syndrome. *Journal of cardiovascular electrophysiology* **8,** 1280-1290.

Signore S, Sorrentino A, Ferreira-Martins J, Kannappan R, Shafaie M, Del Ben F, Isobe K, Arranto C, Wybieralska E, Webster A, Sanada F, Ogorek B, Zheng H, Liu X, Del Monte F, D'Alessandro DA, Wunimenghe O, Michler RE, Hosoda T, Goichberg P, Leri A, Kajstura J, Anversa P & Rota M. (2013). Inositol 1, 4, 5-trisphosphate receptors and human left ventricular myocytes. *Circulation* **128,** 1286-1297.

Sossalla S, Maurer U, Schotola H, Hartmann N, Didie M, Zimmermann WH, Jacobshagen C, Wagner S & Maier LS. (2011). Diastolic dysfunction and arrhythmias caused by overexpression of CaMKIIdelta(C) can be reversed by inhibition of late Na(+) current. *Basic research in cardiology* **106,** 263-272.

Sossalla S, Wagner S, Rasenack EC, Ruff H, Weber SL, Schondube FA, Tirilomis T, Tenderich G, Hasenfuss G, Belardinelli L & Maier LS. (2008). Ranolazine improves diastolic dysfunction in isolated myocardium from failing human hearts--role of late sodium current and intracellular ion accumulation. *J Mol Cell Cardiol* **45,** 32-43.

Tang M, Zhang X, Li Y, Guan Y, Ai X, Szeto C, Nakayama H, Zhang H, Ge S, Molkentin JD, Houser SR & Chen X. (2010). Enhanced basal contractility but reduced excitation-contraction coupling efficiency and beta-adrenergic reserve of hearts with increased Cav1.2 activity. *American journal of physiology Heart and circulatory physiology* **299,** H519-528.

Tomaselli GF & Marban E. (1999). Electrophysiological remodeling in hypertrophy and heart failure. *Cardiovasc Res* **42,** 270-283.

Torella D, Rota M, Nurzynska D, Musso E, Monsen A, Shiraishi I, Zias E, Walsh K, Rosenzweig A, Sussman MA, Urbanek K, Nadal-Ginard B, Kajstura J, Anversa P & Leri A. (2004). Cardiac stem cell and myocyte aging, heart failure, and insulin-like growth factor-1 overexpression. *Circ Res* **94,** 514-524.

Trafford AW, Diaz ME, Sibbring GC & Eisner DA. (2000). Modulation of CICR has no maintained effect on systolic Ca2+: simultaneous measurements of sarcoplasmic reticulum and sarcolemmal Ca2+ fluxes in rat ventricular myocytes. *J Physiol* **522 Pt 2,** 259-270.

Undrovinas NA, Maltsev VA, Belardinelli L, Sabbah HN & Undrovinas A. (2010). Late sodium current contributes to diastolic cell Ca2+ accumulation in chronic heart failure. *The journal of physiological sciences : JPS* **60,** 245-257.

Vaidyanathan R, O'Connell RP, Deo M, Milstein ML, Furspan P, Herron TJ, Pandit SV, Musa H, Berenfeld O, Jalife J & Anumonwo JM. (2013). The ionic bases of the action potential in isolated mouse cardiac Purkinje cell. *Heart Rhythm* **10,** 80-87.

Vassalle M & Lin CI. (2004). Calcium overload and cardiac function. *Journal of biomedical science* **11,** 542-565.

Voigt N, Li N, Wang Q, Wang W, Trafford AW, Abu-Taha I, Sun Q, Wieland T, Ravens U, Nattel S, Wehrens XH & Dobrev D. (2012). Enhanced sarcoplasmic reticulum Ca2+ leak and increased Na+-Ca2+ exchanger function underlie delayed afterdepolarizations in patients with chronic atrial fibrillation. *Circulation* **125,** 2059-2070.

Volk T, Nguyen TH, Schultz JH, Faulhaber J & Ehmke H. (2001). Regional alterations of repolarizing K+ currents among the left ventricular free wall of rats with ascending aortic stenosis. *J Physiol* **530,** 443-455.

Wagner S, Dybkova N, Rasenack EC, Jacobshagen C, Fabritz L, Kirchhof P, Maier SK, Zhang T, Hasenfuss G, Brown JH, Bers DM & Maier LS. (2006). Ca2+/calmodulin-dependent protein kinase II regulates cardiac Na+ channels. *J Clin Invest* **116,** 3127-3138.

Wagner S, Ruff HM, Weber SL, Bellmann S, Sowa T, Schulte T, Anderson ME, Grandi E, Bers DM, Backs J, Belardinelli L & Maier LS. (2011). Reactive oxygen species-activated Ca/calmodulin kinase IIdelta is required for late I(Na) augmentation leading to cellular Na and Ca overload. *Circ Res* **108,** 555-565.

Walker KE, Lakatta EG & Houser SR. (1993). Age associated changes in membrane currents in rat ventricular myocytes. *Cardiovasc Res* **27,** 1968-1977.

Wang L & Duff HJ. (1997). Developmental changes in transient outward current in mouse ventricle. *Circ Res* **81,** 120-127.

White M, Roden R, Minobe W, Khan MF, Larrabee P, Wollmering M, Port JD, Anderson F, Campbell D, Feldman AM & et al. (1994). Age-related changes in beta-adrenergic neuroeffector systems in the human heart. *Circulation* **90,** 1225-1238.

Wickenden AD, Kaprielian R, Parker TG, Jones OT & Backx PH. (1997). Effects of development and thyroid hormone on K+ currents and K+ channel gene expression in rat ventricle. *J Physiol* **504 (Pt 2),** 271-286.

Wilcox JE, Rosenberg J, Vallakati A, Gheorghiade M & Shah SJ. (2011). Usefulness of electrocardiographic QT interval to predict left ventricular diastolic dysfunction. *The American journal of cardiology* **108,** 1760-1766.

Wu L, Ma J, Li H, Wang C, Grandi E, Zhang P, Luo A, Bers DM, Shryock JC & Belardinelli L. (2011). Late sodium current contributes to the reverse rate-dependent effect of IKr inhibition on ventricular repolarization. *Circulation* **123,** 1713-1720.

Xiao RP, Spurgeon HA, O'Connor F & Lakatta EG. (1994). Age-associated changes in beta-adrenergic modulation on rat cardiac excitation-contraction coupling. *J Clin Invest* **94,** 2051-2059.

Zaza A, Belardinelli L & Shryock JC. (2008). Pathophysiology and pharmacology of the cardiac "late sodium current.". *Pharmacol Ther* **119,** 326-339.

Zaza A & Rocchetti M. (2013). The late Na+ current--origin and pathophysiological relevance. *Cardiovascular drugs and therapy / sponsored by the International Society of Cardiovascular Pharmacotherapy* **27,** 61-68.

Zile MR, Gaasch WH, Carroll JD, Feldman MD, Aurigemma GP, Schaer GL, Ghali JK & Liebson PR. (2001). Heart failure with a normal ejection fraction: is measurement of diastolic function necessary to make the diagnosis of diastolic heart failure? *Circulation* **104,** 779-782.

Appendix

Table 1. Primers for PCR Analysis.

Gene	Primers
Mouse Tgfb1	F: 5'-GAAGGACCTGGGTTGGAAGT-3'
	R: 5'-TGGTTGTAGAGGGCAAGGAC-3'
Mouse Vim	F: 5'-AGAGAGAGGAAGCCGAAAGC-3'
	R: 5'-TCCACTTTCCGTTCAAGGTC-3'
Mouse Hprt	F: 5'-AGCCCCAAAATGGTTAAGGT-3'
	R: 5'-CAAGGGCATATCCAACAACA-3'
Mouse Scn1a	F: 5'-AGTAACCCTCCCGACTGGACAAAG-3'
	R: 5'-CCATGGGTCGCGAAGGAAAG-3'
Mouse Scn3a	F: 5'-GAGAGCGACGCAACAGTAACG-3'
	R: 5'-CCAGCATGGTGGACACTTCT-3'
Mouse Scn4a	F: 5'-CCTGGAACTGGCTGGACTTCAGTG-3'
	R: 5'-GATCAGGGCTCCCACGATCG-3'
Mouse Scn5a	F: 5'-AGTACCCAGAAGACCTTCATCGTG-3'
	R: 5'-GGTGCACATGATGAGCATGC-3'
Mouse Scn8a	F: 5'-GACTTTGACCCGTACTATTTG-3'
	R: 5'-ATCATGCTGAAGACTGAATG-3'
Mouse Scn1b	F: 5'-GCGTCGTCAAGAAGATCCAC-3'
	R: 5'-CATCTCTGCCACAAGCCATA-3'
Mouse Scn2b	F: 5'-CAACTCCTGCTACACCGTGA-3'
	R: 5'-TCATTCGGAACTGGAGGAAC-3'
Mouse Scn4b	F: 5'-GGCAATACTCAGGCGAGATG-3'
	R: 5'-ATAGCGTAGATGGTGGTGGC-3'
Mouse Kcna4	F: 5'-AAAGGGGAAACAAATCACCG-3'
	R: 5'-GCAGGAAATGAAGAGCATCC-3'
Mouse Kcna5	F: 5'-ATGAGGCCCATCACTGTAGG-3'
	R: 5'-AAAATTGGAGACGATGACGG-3'
Mouse Kcnb1	F: 5'-CTGGAGAAGCCCAACTCATC-3'
	R: 5'-TGTTGAGTGACAGGGCAATG-3'

Mouse Kcnd2	F: 5'-TCAGCAAGCAAGTTCACCAG-3'
	R: 5'-TTCCCTGCTATGGTTTTTGG-3'
Mouse Kcnd3	F: 5'-TCTGCCAGCAAGTTCACAAG-3'
	R: 5'-TTCCCTGCGATTGTCTTAGG-3'
Mouse Kcnip2	F: 5'-GGAGAGTTTGTCCGAATCCC-3'
	R: 5'-AGCTTGAGGAAACGCTGCT-3'
Mouse Cacna1c	F: 5'-CACCAACTCCAACCTGGAAC-3'
	R: 5'-TGGAAGAGAAGTCCGTAGGC-3'
Mouse Ryr2	F: 5'-ATCTTGGTCAGCGTGTCCTC-3'
	R: 5'-TGCTTCACTTCCTGAGCTGAT-3'
Mouse Atpa2a	F: 5'-TGCAACTCGGTCATAAAGCA-3'
	R: 5'-TGGCTTGTTTGGGGTACAAT-3'
Mouse Slc8a1	F: 5'-AGGAGACAGACCAGCTTCCA-3'
	R: 5'-CAAAACCAGAGCCCCATCTA-3'
Mouse Pln	F: 5'-CCCAGCTAAGCTCCCATAAG-3'
	R: 5'-AACAGGCAGCCAAATGTG-3'
Mouse β2m	F: 5'-CTCGGTGACCCTGGTCTTTCTG-3'
	R: 5'-ATGTGAGGCGGGTGGAACTG-3'

Table 2. Antibodies for Western Blot Analysis.

Antigen	Antibody	Manufacturer
Anti-SCN5A (Nav1.5)	rabbit polyclonal	Gift of Dr. Hugues Abriel
Anti-SCN1B (Navβ1)	rabbit monoclonal	Cell Signaling Technology
Anti-SERCA2a	Mouse monoclonal	Sigma-Aldrich
GAPDH	rabbit monoclonal	Cell Signaling Technology

Table 3. Fitting Parameters.

I_{NaL}, Steady State Inactivation		**$V_{1/2G}$**	**k_G**	**R^2**	**P**
Young		-61.5±0.7 mV	-11.6±0.7 mV	0.9974	0.9954
Old		-61.5±0.5 mV	-11.1±0.5 mV	0.9985	
I_{NaL}, Recovery from Inactivation			**τ**	**R^2**	**P**
Young			655±17 ms	0.9965	0.6254
Old			756±80 ms	0.9968	
I_{Na}, Conductance	**g_{max}**	**$V_{1/2G}$**	**k_G**	**R^2**	**P**
Young	0.468±0.004 $mS \cdot \mu F^{-1}$	-52.9±0.2 mV	3.1±0.2 mV	0.9992	0.6270
Old	0.427±0.004 $mS \cdot \mu F^{-1}$	-54.0±0.2 mV	3.2±0.2 mV	0.9992	
I_{Na}, Activation		**$V_{1/2G}$**	**k_G**	**R^2**	**P**
Young		-52.7±0.4 mV	3.9±0.3 mV	0.9970	0.8170
Old		-53.7±0.3 mV	3.5±0.3 mV	0.9979	
I_{Na}, Steady State Inactivation		**$V_{1/2G}$**	**k_G**	**R^2**	**P**
Young		-81.0±0.1 mV	-5.7±0.1 mV	0.9999	0.9979
Old		-81.0±0.1 mV	-5.5±0.1 mV	0.9999	

I_{Na}, Recovery from Inactivation			**τ**	**R^2**	**P**
Young			17.7±0.6 ms	0.9988	0.9169
Old			18.1±0.8 ms	0.9981	
I_{CaL}, Conductance	**g_{max}**	**$V_{1/2G}$**	**k_G**	**R^2**	**P**
Young	0.0589±0.002 $mS \cdot \mu F^{-1}$	-8.6±0.8 mV	3.95±0.8 mV	0.8408	0.0864
Old	0.0662±0.002 $mS \cdot \mu F^{-1}$	-7.2±0.8 mV	4.29±0.6 mV	0.8609	
I_{CaL}, Activation		**$V_{1/2G}$**	**k_G**	**R^2**	**P**
Young		-7.3±0.4 mV	5.0±0.3 mV	0.9552	0.4404
Old		-6.0±0.3 mV	5.1±0.3 mV	0.9650	
I_{CaL}, Steady State Inactivation		**$V_{1/2G}$**	**k_G**	**R^2**	**P**
Young		-16.3±0.3 mV	-7.2±0.3 mV	0.9722	0.7419
Old		-16.9±0.3 mV	-7.0±0.3 mV	0.9781	
AP_{clamp}-Ca^{2+} Transient Decay		**F_p/F_0 (peak fluorescence)**	**τ**	**R^2**	
Young – APD_{50} 5ms		2.163±0.1043 F/F_0	177.2 ms	0.3868	
Young – APD_{50} 7ms		2.204±0.1072 F/F_0	170.4 ms	0.3907	
Young – APD_{50} 17ms		2.504±0.1250	178.1 ms	0.4250	

	F/F_0			
Young – APD_{50} 26ms	2.628±0.1346 F/F_0	169.7 ms	0.4310	
Young – APD_{50} 80ms	3.591±0.1841 F/F_0	176.9 ms	0.5136	
Old – APD_{50} 5ms	1.842±0.05437 F/F_0	171.7 ms	0.6195	
Old – APD_{50} 7ms	1.967±0.06877 F/F_0	169.2 ms	0.5766	
Old – APD_{50} 17ms	2.181±0.07849 F/F_0	166.5 ms	0.6123	
Old – APD_{50} 26ms	2.323±0.08127 F/F_0	165.0 ms	0.6481	
Old – APD_{50} 80ms	2.960±0.1418 F/F_0	168.1 ms	0.5754	

AP_{clamp}-Ca^{2+} Transient Decay	**Slope**	**R^2**	**P**
Young - Ca^{2+} Transient Amplitude	0.01683±0.001 $F/F_0 \cdot ms^{-1}$	0.9925	0.044
Old - Ca^{2+} Transient Amplitude	0.01265±0.0014 $F/F_0 \cdot ms^{-1}$	0.9642	
Young - Ca^{2+} Transient Time to Peak	0.2370±0.03442 $ms \cdot ms^{-1}$	0.9405	0.5484
Old – Ca^{2+} Transient Time to Peak	0.2141±0.01071 $ms \cdot ms^{-1}$	0.9925	
Young - 30% Ca^{2+} Transient Decay	0.2270±0.031 $ms \cdot ms^{-1}$	0.9485	0.2712
Old - 30% Ca^{2+} Transient Decay	0.1878±0.011 $ms \cdot ms^{-1}$	0.9903	
Young - 90% Ca^{2+} Transient Decay	-0.5773±0.142 $ms \cdot ms^{-1}$	0.8459	0.3883
Old - 90% Ca^{2+} Transient Decay	-0.7359±0.094	0.9533	

			$ms \cdot ms^{-1}$		
Diastolic Length-Tension Relation		**a**	**b**	**R^2**	**P**
Young		20. 6±1.5 $mN \cdot mm^{-2}$	10.5±1.6 $mN \cdot mm^{-2}$	0.9090	<0.0001 ANOVA
Old		24.5±2.6 $mN \cdot mm^{-2}$	29.3±2.9 $mN \cdot mm^{-2}$	0.9646	
Young Mex		17.6±3.6 $mN \cdot mm^{-2}$	5.5±4.1 $mN \cdot mm^{-2}$	0.7829	
Old Mex		29.5±2.8 $mN \cdot mm^{-2}$	9.7±3.2 $mN \cdot mm^{-2}$	0.9152	
Young ATX-II		19.7±2.7 $mN \cdot mm^{-2}$	28.4±3.1 $mN \cdot mm^{-2}$	0.9435	<0.0001 vs. Young